Magnetic Field Induced Photocurrents in Semiconductor Nanostructures under THz Laser Excitation

DISSERTATION

zur Erlangung des Doktorgrades der Naturwissenschaften
(Dr. rer. nat.)
der Fakultät für Physik
der Universität Regensburg
vorgelegt von

Dipl.-Phys. Sebastian Stachel
aus Neumarkt i.d.Opf.

im Jahr 2013

Das Promotionsgesuch wurde am 13. Juni 2013 eingereicht.

Die Arbeit wurde von Prof. Dr. Sergey D. Ganichev angeleitet.

Das Kolloquium fand am 22. Oktober 2013 statt.

Prüfungsausschuss:

Vorsitzender:	Prof. Dr. Andrea Donarini
1. Gutachter:	Prof. Dr. Sergey D. Ganichev
2. Gutachter:	Prof. Dr. Christian Schüller
weiterer Prüfer:	Prof. Dr. Josef Zweck

Contents

1 Introduction

In the last decades, the research field of spintronics emerged in order to revolutionize the current charge-based electronics [1]. This new field tries to benefit from the usage of the electron's spin instead of its charge as information carrier. The goal of this paradigm change is to enhance the functionality and performance of the traditional semiconductor devices. Almost all spintronic applications, like e.g. the spin field-effect transistor proposed by Datta and Das [2] or the spin Hall effect transistor [3], are based on the same fundamental requirements: the injection of the carrier spin, its manipulation and control in a semiconductor, and finally the detection of the spin. The manipulation and control is usually achieved by external fields and utilizes a fundamental spin-dependent interaction in semiconductors, the spin-orbit coupling (SOC) [4, 5]. For this purpose, narrow-gap semiconductors are of great interest due to their extraordinary large SOC, and consequently the possibility to control the spin by an applied voltage via the Rashba field [6]. In addition to the strong SOC, heterostructures composed of small energy-gap materials are usually characterized by high electron mobilities providing the opportunity for ballistic transport [7–9]. These transport properties are crucial for an effective operation of spintronic devices, as well as for the further development of conventional low-power high-speed electronics [10].

A narrow-gap semiconductor with many advantageous material properties is indium antimonide (InSb). Among all III-V semiconductors, InSb possesses the lightest electron effective mass (0.0138 m_e at the band edge) and one of the narrowest energy band gaps (170 meV at room temperature) along with an extraordinary large effective Landé g^*-factor of -51 in the bulk [11,12]. Furthermore, the heavy constituent atoms give rise to strong internal electric fields, which cause a strong SOC. The resulting large Rashba field in low-dimensional structures together with the huge g^*-factor offers many advantages over their wider gap counterparts like GaAs or Si regarding the control and manipulation of the spin [13–15]. Many of these advantages only become apparent if the carriers are confined to two dimensions in a heterostructure. However, there are various challenges with heavily mismatched epitaxial growth of low-dimensional structures due to the large lattice mismatch between InSb and

commonly used substrates [16–18]. Despite these difficulties, recent improvements in the growth processes led to the availability of high-quality InSb-based heterostructures, which motivated a number of opto-electronic effects like, e.g., terahertz photoconductivity or the circular photogalvanic effect [19, 20].

In this work, magnetic-field-induced photocurrents in InSb quantum wells (QWs) are investigated by excitation with terahertz (THz) radiation [21]. In particular the linear and the circular magnetogyrotropic photogalvanic effect (MPGE), which so far have been observed mainly in wider gap materials [22–24], will be demonstrated. It will be shown that the (Drude-type) absorption of THz radiation causes a dc electric current in the presence of an in-plane magnetic field. The origin of this current is based on the asymmetry of the relaxation of carriers in the momentum space. Two fundamental different mechanisms contribute to the MPGE: a spin-related and a spin-independent one. The spin-based contribution results from a spin-dependent scattering of electrons on phonons or static defects as a consequence of the SOC. The second, orbital mechanism stems from an asymmetric relaxation due to the Lorentz force acting on heated carriers [25, 26]. A detailed investigation of the magnetic-field-induced photocurrents in InSb QWs allows to obtain information about the role of both mechanisms as well as their interplay. In particular the strength of both contributions is of great interest considering the huge spin-related properties in this material.

In the second part of this work, cyclotron resonance (CR) assisted photocurrents in InSb-based QWs are investigated. So far, THz radiation induced currents were mainly studied in the presence of an in-plane magnetic field. For the investigation of photo-induced currents under CR absorption, InSb structures represent a suitable material, since due to the small effective electron mass, the CR condition is fulfilled in the THz range at rather low magnetic field strengths [27, 28]. It will be demonstrated that the application of a normal magnetic field and excitation under oblique incidence of light results in resonantly enhanced signals. The microscopic origin of the resonant currents is discussed in terms of the photon drag effect and the cyclotron motion of the carriers. Moreover, the study of these resonant photocurrents may deliver information on the band structure of InSb and can thereby give further access to

the understanding of InSb heterostructures and their application for electronic devices.

This work is organized as follows: The first part of chapter 2 describes the physical basics regarding magnetic-field-induced photocurrents. These basics include the band structure of InSb with all its peculiarities. In the second part of chapter 2, the phenomenological and microscopic theories of THz radiation-induced photocurrents are introduced. The following chapter describes the studied samples and the experimental setups, including the THz laser systems as well as the sample alignments. In chapter 4, the photoresponses, which are independent of an applied magnetic field, are briefly presented. These currents allow to obtain information about the symmetry properties of the studied structures. Subsequently, chapter 5 deals with the experimental observation of the linear and circular MPGE in InSb-based QWs. Afterwards, both effects are discussed in the context of an interplay between spin-related and orbital contributions. Finally, the investigation of photocurrents under cyclotron resonance condition is presented. This chapter is completed by the development of a microscopic model based on the photon drag effect in the presence of a normal magnetic field.

2 Physical basics

In this chapter, the physical fundamentals being essential for the understanding of magnetic field induced photocurrents in InSb based quantum wells are introduced. First, the band structure of bulk InSb with its peculiarities compared to other semiconductors is presented. This includes the distances between the bands, which defines InSb as a narrow gap material, as well as their splitting due to the spin-orbit interaction. For this material, also the deviation from the parabolic approximation of the conduction band is of fundamental interest and will be described here. Furthermore, the interaction between the bands and the resulting effects on the characteristic parameters like the electron effective mass and the Landé g^*-factor are explained. After demonstrating the effects of a confinement of the carriers in two dimensions, the consequences of the bulk and structure inversion asymmetry are described. The second part of this chapter deals with the basics of THz radiation induced effects responsible for photocurrents in InSb-based structures. First, the effects which do not require the application of a magnetic field are presented: the circular (CPGE) and the linear photogalvanic effect (LPGE), as well as the photon drag effect. As they are not in the focus of this work, these effects are only introduced on a phenomenological level. Finally, the linear (LMPGE) and circular magneto-gyrotropic photogalvanic effect (CMPGE) are presented phenomenologically and microscopically.

2.1 The bandstructure of indium antimonide

In order to understand the many extraordinary properties of InSb, it is necessary to take a closer look at the successive energy bands formed in this solid, which belongs to the group of III-V semiconductors. Within this group, the material possesses an outstanding status due to one of the smallest band gaps [29]. In general, small energy band gaps require an accurate treatment of the band structure, which is greatly affected by a strong band mixing. This makes InSb to an applicable model example for the band structure calculation of narrow gap semiconductors.

2.1.1 Energy bands and parameters of bulk InSb in parabolic approximation

The first who exactly calculated the band structure of bulk InSb by $\boldsymbol{k}\cdot\boldsymbol{p}$ theory was E. O. Kane [30]. By including the $\boldsymbol{k}\cdot\boldsymbol{p}$ interaction between the first conduction band Γ_{6c} and the valence bands Γ_{8v} as well as Γ_{7v}, and treating all other bands by second order perturbation theory, he calculated the energy dispersion relation $E(\boldsymbol{k})$. This approach is known as the *Kane model* [32], representing a milestone for band structure computational methods and thus, stimulated a huge number of theoretical and experimental investigations of InSb as well as many other semiconductor materials. Fig. 1 illustrates the detailed order of the energy bands for bulk InSb at $T = 0$ resulting from the *Kane model*. Here, the minimum of the lowest conduction band Γ_{6c} was defined as $E = 0$ at the Γ-point of the Brillouin zone. The important bands are the conduction band Γ_{6c} and the valence band Γ_{8v}, whose energy distance defines the fundamental gap in direct semiconductors. The energy gap is in InSb $E_0 = E(\Gamma_{6c})$ - $E(\Gamma_{8v}) = 0.237$ eV, being much smaller than in most of the other III-V semiconductors [12]. The basic findings of Kane's calculations were that due to the narrow band gap and hence, a mutual interaction between the conduction and the valence band, an unusual low effective electron mass and an extraordinary large Landé g^*-factor arises.

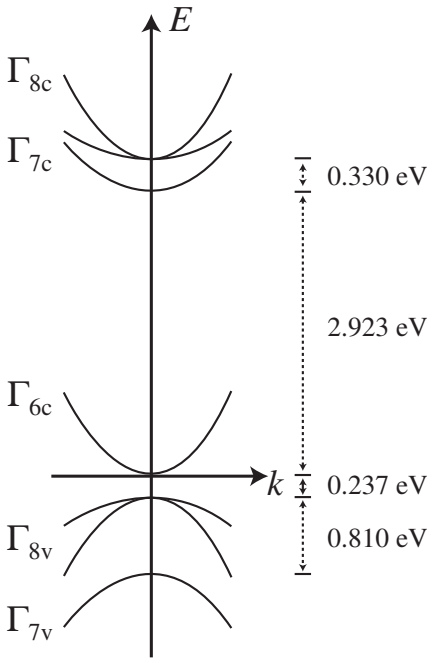

Figure 1: Qualitative sketch of the band structure of InSb. The distances between the single bands reflect the ratio between the single energy separations after [31].

In addition to the band gap, InSb represents a highly interesting material regarding the single atoms with their heavy masses resulting in large relativistic effects, in particular in a strong spin-orbit coupling (SOC). To give an obvious explanation of this coupling, one can imagine an electron moving with velocity

$\boldsymbol{v}$ through the electric field $\boldsymbol{E}$ of the atomic core or lattice [29, 31, 33]. In the inertial system of the moving electron, beside the electric field, a magnetic field $\boldsymbol{B'} = -\frac{1}{c^2}\boldsymbol{v} \times \boldsymbol{E}$ arises to the lowest order in v/c, where c is the light's velocity in vacuum. As a consequence, the magnetic moment of the electron $\boldsymbol{\mu}_s$ couples to the magnetic field $\boldsymbol{B'}$, which leads to the following correction in the Hamiltonian:

$$H_{SO} = -\boldsymbol{B'} \cdot \boldsymbol{\mu}_s = g\mu_B \boldsymbol{B'} \cdot \boldsymbol{s} = \frac{g\hbar}{4c^2 m_e^2} \left(\nabla V(\boldsymbol{r}) \times \boldsymbol{p}\right) \cdot \boldsymbol{s}. \tag{1}$$

Here, μ_B is the Bohr magneton, $\boldsymbol{s}$ the electron's spin giving rise to its magnetic moment $\boldsymbol{\mu}_s$, g the electron spin g-factor, $V(\boldsymbol{r})$ the potential of the atomic core or lattice and $\boldsymbol{p}$ the electron's momentum. From Eq. (1) follows that the heavier the single atoms, e.g. In and Sb, the stronger the SO coupling resulting from the potential $V(\boldsymbol{r})$. This trend is also valid if the two atoms are composed in a lattice crystal [29].

The spin-orbit coupling also affects the band structure and leads to a splitting of the valence band (see Fig. 1). While the electron states in the Γ_{6c} band have no orbital angular momentum $l = 0$ (s-like), the states in the valence band have $l = 1$ (p-like) and can therefore couple with the electron's spin ($s = 1/2$) to the total angular momentum $j = l + s$. Therefore, the valence band is split into heavy- and light-hole band (Γ_{8v}) with $j = 3/2$, and a separated split-off band (Γ_{7v}) with $j = 1/2$. The energy difference $\Delta_0 = E(\Gamma_{8v})$ - $E(\Gamma_{7v})$ describes the Pauli spin-orbit interaction, which stems from the Coulomb potential of the innermost region of the individual atomic cores. As a result of the large effective atomic number of indium and antimony, the Δ_0 splitting in InSb (0.810 eV) is much larger than in many other semiconductors like, e.g., GaAs (0.341 eV) or Si (0.044 eV) [31, 32].

For most of the semiconductors with wider band gap, it is necessary to calculate the band structure exactly by taking into account the interactions between all bands addressed above. This approach is called the *extended Kane model*. However for semiconductors with smaller energy band gap E_0, it is sufficient to take into account only 4 bands (Γ_{6c}, $2\times\Gamma_{8v}$, Γ_{7v}). This results from the fact that the other two highest conduction bands Γ_{7c} and Γ_{8c}, in particular in InSb (see Fig. 1), are much larger distant from the lowest 4 bands than in other

materials [34, 35]. By using this 4-band-model, where all bands are two-fold spin degenerated, the calculated band structure also allows to draw conclusions about basic parameters like the electron's effective mass or the Landé g^*-factor. For the effective mass m_0^* at the bulk conduction band minimum, one obtains [31]:

$$\frac{m_0}{m_0^*} = \frac{2m_0}{\hbar^2}\frac{\hat{P}^2}{3}\left(\frac{2}{E_0} + \frac{1}{E_0 + \Delta_0}\right), \tag{2}$$

where m_0 is the mass of a free electron and $\hat{P}$ the momentum matrix element. From this equation it is readily apparent that the small energy gap E_0 leads to a small effective mass of $m_0^* = 0.014\, m_0$ at the minimum of the conduction band. This value is one of the smallest within the group of III-V semiconductors and is a result of the strong repulsion of the conduction and valence band. For small $\boldsymbol{k}$ and consequently small energies E, the dispersion relation for the Γ_{6c} band can be treated in parabolic approximation as $E(\boldsymbol{k}) = \frac{\hbar^2 \boldsymbol{k}^2}{2m_0^*}$, where the effective mass m_0^* is an energy-independent constant. For larger $\boldsymbol{k}$ and E, contributions of higher than second order have to be taken into account leading to a nonparabolic dependence of $E(\boldsymbol{k})$, and therefore m_0^* becomes energy-dependent [32].

In addition to the effective mass, the Landé g^*-factor is an important parameter in the presence of an external applied magnetic field. Beside the magnitude of the applied field, this factor defines the strength of the Zeeman splitting between the spin-up and -down conduction band. Similar to the effective mass in InSb, the Landé g^*-factor strongly deviates from the Landé factor of a free electron $g_0 \approx 2$. This behavior results again from the strong mutual interaction of the conduction and valence band and is expressed in the formula from L. Roth [36]:

$$\frac{g^*}{2} = -\frac{2m_0}{\hbar^2}\frac{\hat{P}^2}{3}\left(\frac{1}{E_0} - \frac{1}{E_0 + \Delta_0}\right), \tag{3}$$

From Eq. (3) it can be seen that the small E_0 and large Δ_0 cause for InSb a huge negative Landé g_0^*-factor of -51 at the bulk conduction band edge, being the largest in comparison to other semiconductors [11]. Like for the effective mass, Eq. (3) is also restricted to the parabolic approximation [37].

2.1.2 Nonparabolic corrections

If electrons acquire energies comparable to a fraction of the band gap, or in other words occupy higher energy states of the conduction band, the nonparabolicity mentioned above cannot be neglected anymore. The nonparabolicity can be taken into account by including corrections to the energy dispersion of higher orders than $\boldsymbol{k}^2$ [30, 32, 37, 39–41]. Accordingly, the parabolic dispersion for a bulk semiconductor can be modified by:

$$E(\boldsymbol{k}) = \frac{\hbar^2 \boldsymbol{k}^2}{2m_0^*}(1 - \gamma' \boldsymbol{k}^2). \tag{4}$$

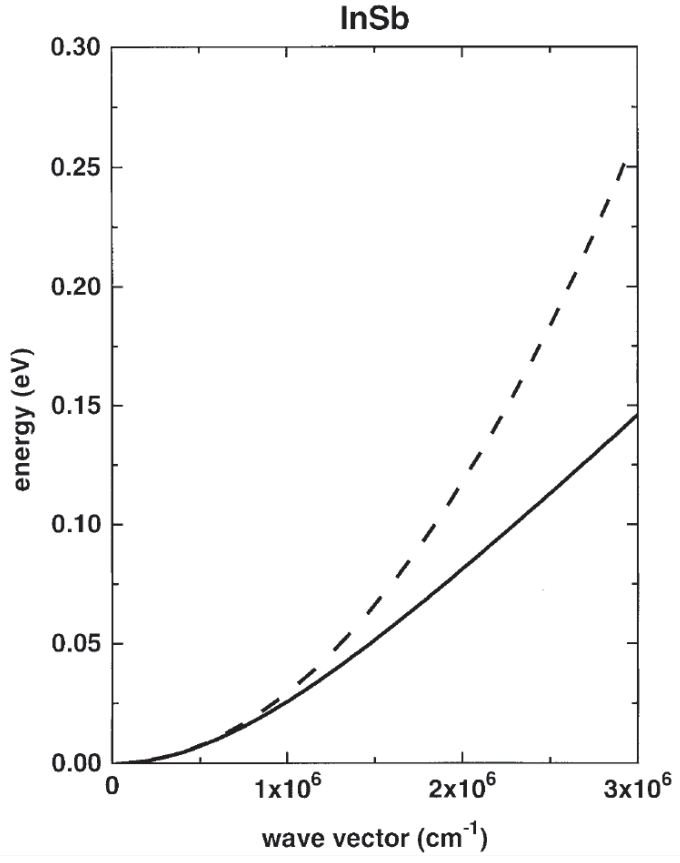

Figure 2: Conduction band of InSb at room temperature for a parabolic dispersion (dashed line) and Kane's nonparabolic relation (solid line) after [38].

Here γ' is the positive nonparabolicity parameter and describes the strength of the deviation from the parabolic approximation. In Fig. 2, the energy of the conduction band is plotted against the wave vector $\boldsymbol{k}$ for the parabolic as well as the nonparabolic dependence of InSb. From this one can clearly see the deviation of the nonparabolic treatment from the parabolic approximation for higher E and $\boldsymbol{k}$. This deviation affects both, the effective mass and the Landé g^*-factor, which can be modified by the following equations [32, 41, 42]:

$$m^*(E) = m_0^* \cdot \left[1 + \frac{2E}{E_0}\right], \qquad g^*(E) = g_0^* + \beta \cdot E. \tag{5}$$

Here β represents a positive, material dependent parameter. As a result, the nonparabolicity in InSb leads to an increase of the effective mass and a decrease of the Landé g^*-factor compared to their values at the band edge. Considering lower dimensions and doped structures instead of the bulk undoped material treated so far, this effect increases [38]. This is caused by the fact that the density of states $\Theta(E)$ decreases for small values of the effective mass m_0^*, as well as for a reduction of the dimension from 3D to 2D $\left(\Theta_{3D}(E) \sim (m_0^*)^{\frac{3}{2}};\ \Theta_{2D}(E) \sim m_0^*\right)$ [43]. Consequently, for a degenerated carrier concentration, higher energies are reached and the effect on $m^*(E)$ and $g^*(E)$ becomes stronger.

2.1.3 Two-dimensional band structure

So far, the band structure of InSb was considered only for the case of a three-dimensional crystal. However, for many physical effects it is essential to reduce the spatial degree of freedom by forming heterostructures or quantum wells. The resulting confinement of electrons in two dimensions allows to separate them from charged impurities by modulation doping. This reduces impurity scattering, which is important for the realization of high electron mobility structures [33]. In a quantum well, the reduction of the dimension is accomplished by placing the semiconductor material between two semiconductors with larger band gap. For InSb, a appropriate barrier material is InAlSb, whose band gap can be adjusted by the amount of Al and ensures a small mismatch between the barrier and the well. Fig. 3 shows the size-quantization

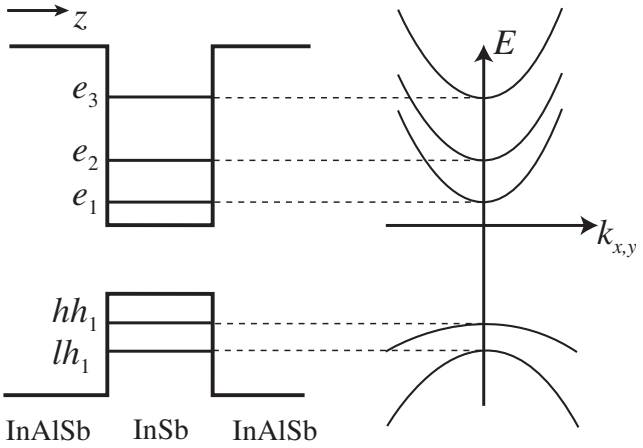

Figure 3: Effect of size-quantization due to the confinement of the carriers in InSb between InAlSb. The confinement splits the conduction and heavy-/light hole band into subbands e_i and hh_i/hl_i.

of the conduction and valence band due to the confinement of electrons and holes. Consequently, the carrier's motion ($k_{x,y}$) is restricted to the plane between the barriers and perpendicular to the growth direction. The quantization leads to energy-separated subbands in the conduction e_i and the valance band hh_i/hl_i. The quantum mechanical zero-point energy increases the energy gap with respect to the bulk material. Furthermore, in materials with spin-orbit interaction, the size quantization lifts the degeneracy between heavy hole and light hole band at $k_{x,y} = 0$.

2.1.4 The effects of bulk and structure inversion asymmetry

In the previous sections, a detailed treatment of the band structure of InSb revealed the essential importance of the interaction between the conduction and the valence band, which yields a strong separated split-off band, as well as a huge Landé g^*-factor and a low effective mass m^*. In addition to these effects, the SO coupling may also result in a *spin* splitting of the individual bands even in the absence of an external magnetic field. In section 2.1.1, the band structure was treated with the assumption of a spatial inversion symmetry of the crystal, as well as time-reversal symmetry. The consequence is that every single band is spin-degenerated. However, in contrast to, e.g.

Si or Ge, the InSb lattice with its zinc blende structure possess a lack of spatial symmetry and consequently, the spin-degeneracy is removed. Due to the asymmetry of the crystal lattice, this contribution to the SO splitting is called the bulk inversion asymmetry (BIA) and appears in the Hamiltonian as the Dresselhaus term [44]. The BIA term also contributes if the dimensions are reduced to 2D by forming a heterojunction or quantum well. For this case, an additional term arises, the Rashba term, which has its origin in the spatial inversion-asymmetry of the structure (SIA) [45]. Figure 4 shows the effect

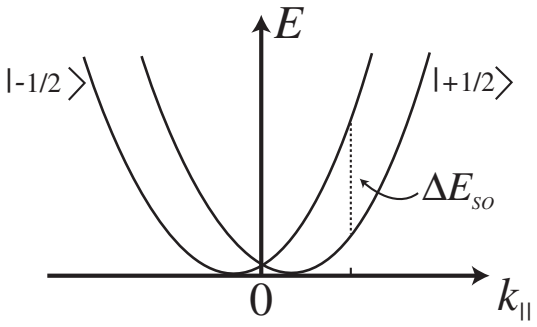

Figure 4: Qualitative illustration of the conduction band at the Γ-point including spin-orbit coupling for a non-centrosymmetric crystal.

of both asymmetries on the spin splitting of the conduction band for a two dimensional structure. The single spin subbands are shifted along the in-plane wave vector $k_{||} = \sqrt{k_x^2 + k_y^2}$, which yields for fixed $k_{||}$ an energy separation of ΔE_{SO} between spin up and spin down subband. Neglecting cubic in k-terms, this energy spin-splitting from both, SIA and BIA, is expressed in the 2D Hamiltonian for a (001)-grown quantum well as follows [46, 47]:

$$H_{SO}^{2D} = \alpha \left(\sigma_x k_y - \sigma_y k_x\right) + \beta \left(\sigma_y k_y - \sigma_x k_x\right). \tag{6}$$

Here, α and β represent material parameters, which indicate the strength of the Rashba and the linear Dresselhaus term, respectively. $\boldsymbol{\sigma}$ is the vector of Pauli spin matrices and the crystallographic axes were chosen as $x \parallel [100]$ and $y \parallel [010]$. The Rashba term in Eq. (6) depends on the asymmetry of the structure, but also on the strength of the admixture of the conduction and valence band. The reason is that the electron's wave function is composed of

	GaAs	InAs	InSb
α_0[eÅ^2]	5.2	117.1	523.0
β_0[eVÅ^3]	27.6	27.2	760.1

Table 1: Values of the Rashba and Dresselhaus coefficients for certain materials after [31].

a Bloch part, which has the periodicity of the lattice, and a envelope function. The first one is affected by the atomic fields and the second one by macroscopic fields [31]. A macroscopic field can be introduced by an asymmetric doping of the structure or an external applied electric field F along the growth direction z. The consequence of this field is expressed via the energy shift due to the Rashba term [48, 49]:

$$\Delta E_{SO}^{R} = 2\alpha_0 eFk_{||}, \quad \text{with} \quad \alpha_0 = \frac{\hbar^2}{2m_0^*}\frac{\Delta_0(2E_0+\Delta_0)}{E_0(E_0+\Delta_0)(3E_0+2\Delta_0)}. \tag{7}$$

α_0 is called the Rashba coefficient and enters in Eq. (6) by $\alpha = eF\alpha_0$. From Eq. (7), it follows that not only the strength of an in-built or applied electric field F defines the Rashba SO splitting, but also the coefficient α_0. Due to the dependence of α_0 on E_0 and Δ_0, the effect is expected to be much stronger in narrow gap materials compared to wider gap materials.

Table 1 shows the Rashba and Dresselhaus coefficients, α_0 and β_0, for different materials. Compared to semiconductors like GaAs, InSb features Rashba and Dresselhaus effects orders of magnitude larger. The Dresselhaus coefficient β_0 is connected to Eq. (6) by $\beta = \beta_0\langle k_z^2\rangle$, where $\langle k_z^2\rangle$ is the expectation value of the squared wave vector component in the direction of the confinement potential [29]. The spin splitting induced by inversion asymmetry and presented in Eq. (6) can also be expressed in another way. For a moving electron and its spin, it can be useful to introduce an effective magnetic field $\boldsymbol{B}_{eff}(\boldsymbol{k}_{||})$, about which the spin precesses with an effective Larmor frequency $\boldsymbol{\Omega}(\boldsymbol{k}_{||}) = g^*\mu_B\boldsymbol{B}_{eff}(\boldsymbol{k}_{||})/\hbar$. Hence, Eq. (6) can be written as $H_{SO}^{2D} = \hbar\boldsymbol{\sigma}\cdot\boldsymbol{\Omega}(\boldsymbol{k}_{||})$ with:

$$\boldsymbol{\Omega}(\boldsymbol{k}_{||}) = \frac{1}{\hbar}\left[(\alpha k_y - \beta k_x)\right), (\beta k_y - \alpha k_x), 0\right]. \tag{8}$$

From this equation it follows that the precession of an electron's spin depends on the strength of the SO coupling, as well as the direction and magnitude of the electron's momentum.

2.1.5 The effects of external magnetic fields

So far we considered the absence of any external magnetic field. However, since the effects under investigation are induced or strongly influenced by an applied magnetic field, the change of the electron's energy due to the field is of importance. Two different orientations of the magnetic field were used in the experiments: the alignment in the plane and perpendicular to the two-dimensional electron gas. In the following, the influence of these two configurations on the conduction band in a QW structure is described.

2.1.5.1 In-plane magnetic field

The application of an in-plane magnetic field only affects the electron's spin via the Zeeman splitting, but not the carrier's orbital motion [33]. The effective Landé g^*-factor determines thereby the strength of the Zeeman spin-splitting. The splitting stems from the fact that the electron's spin magnetic momentum couples to an applied magnetic field $\boldsymbol{B}$. Hence, the spin up and spin down subbands are shifted in energy against each other owing to the difference in the number of electrons, whose spin is aligned parallel or anti-parallel to the direction of $\boldsymbol{B}$. Without taking into account any many-body effects due to the interaction between the electrons, the Zeeman term in the Hamiltonian and the resulting energy splitting is given by the linear expressions [43]:

$$E_Z = g^* \mu_B \boldsymbol{\sigma} \cdot \boldsymbol{B} \quad \Longrightarrow \quad \Delta E_Z = g^* \mu_B B \tag{9}$$

2.1.5.2 Out-of-plane magnetic field

Whereas the Zeeman term contributes to the Hamiltonian independently of the orientation of the magnetic field with respect to the 2DEG, the formation of Landau levels is restricted to a field component $B_\perp$ perpendicular to the 2DEG. In a classical approach, an electron of a 2DEG is, due to $B_\perp$, forced to a cyclotron motion with frequency $\omega_c^* = \frac{eB_\perp}{m^*}$ [50]. An incident light with

frequency ω and electric field $\boldsymbol{E}(\omega)$ perpendicular to $B_\perp$ (Farady configuration) leads to absorption for the cyclotron resonance condition: $\omega = \omega_c^*$. A further condition for absorption is that the time for one cycle of the electron is shorter than its collision time τ_c, which can be expressed by: $\omega_c^* > 1/\tau_c$. The absorption of light can be written as [43, 50]:

$$P_\pm(\omega) = \frac{1}{2} |\boldsymbol{E}|^2 \frac{\sigma \tau_c^{-2}}{\tau_c^{-2} + (\omega \pm \omega_c)^2}, \tag{10}$$

where $\pm$ stands for right- and left-handed circular polarization. The absorption curve exhibits a Lorentzian shape and its width is proportional to $1/\tau_c$.

In the quantum mechanical effective mass approximation (EMA), the perpendicular magnetic field results in a quantization of the energy spectrum along the growth direction and forms Landau levels [31]. Assuming a parabolic dispersion, the energy spectrum is given by a sum of the Landau and the Zeeman term:

$$E_N^{EMA} + E_Z = \hbar\omega_c^* \left(N + \frac{1}{2} \right) \pm \frac{1}{2} g^* \mu_B B, \tag{11}$$

where N is an integer, called the Landau quantum number. Excitation by light, typically in the far-infrared range, induces optical transitions between the Landau levels E_N^{EMA} and E_{N+1}^{EMA}. Within the effective mass approximation, the selection rules for such transitions are given by: $\Delta N = \pm 1$ and $\Delta\sigma = 0$. In the case of a nonparabolic conduction band and consequently an energy dependence of $m^*(E)$ and $g^*(E)$, the first term of Eq. (11) is not linear in B anymore. This energy-dependence may lead to a splitting of the resonance absorption lines of Eq. (10) [31]. Furthermore, taking into account the Rashba and Dresselhaus term from Eq. (6), also spin-flip transitions with $\Delta\sigma = \pm 1$ may be induced. These are caused by the coupling of the spin-subbands of adjacent Landau levels with opposite spin σ.

2.2 Phenomenological theory of photogalvanic effects and photon drag effect

While the previous section mainly dealt with the band structure of InSb and the effect of an external magnetic field, this section describes the influence of an external radiation field in the terahertz range. The small photon energy relative to the energy gap of this material predominantly allows a redistribution of free carriers with respect to their momentum and energy in the same subband, and may in the case of low symmetry structures, like e.g. in InSb QWs, lead to dc electric currents, known as the photogalvanic effects (PGE) and the photon drag effect (PDE) [51]. The PGE can be further classified depending on the polarization of the exciting radiation into the linear photogalvanic effect (LPGE) and the circular photogalvanic effect (CPGE). In this section, we will not go into details of the microscopic models, but will only consider the phenomenological theory of the LPGE and CPGE as well as the PDE.

2.2.0.3 The linear photogalvanic effect

The linear photogalvanic effect is based on the generation of a direct motion of carriers by the oscillating electric field due to nonsymmetric random relaxation and scattering in the potential of a noncentrosymmetric medium [46, 51–53]. Unlike all other photogalvanic effects presented here, the LPGE does not require gyrotropy but is only present in media without an inversion center. Phenomenologically, the photocurrent of the LPGE can be written as:

$$j_\lambda = \sum_{\lambda\mu\nu} \chi_{\lambda\mu\nu} I \frac{(E_\gamma E_\delta^* + E_\delta E_\gamma^*)}{2}, \tag{12}$$

where $\chi_{\lambda\mu\nu}$ is a third-rank tensor, E_γ the components of the electric field $\boldsymbol{E} = E_0\hat{\boldsymbol{e}}$, $\hat{\boldsymbol{e}}$ the unit vector pointing in the direction of the light propagation, E_0 the magnitude of the electric field and $I = E_0^2$ is the light's intensity. As the LPGE is caused by periodically alternating electric fields in the absence of any net force (averaged over one period in time) in systems with sufficiently low symmetry, it can also be understood as a classical microscopic ratchet. This effect may occur for the excitation with linear polarization and even for unpolarized light.

2.2.0.4 The circular photogalvanic effect

The circular photogalvanic effect is caused by the transfer of the photon angular momentum into a direct motion of carriers and is excited by circular polarization [51, 54–56]. The CPGE is defined by the point symmetry of the underlying structure and the media must fulfill the conditions of gyrotropy, which will be introduced in more detail in the next section (see Eq. (15)). Similar to the LPGE, also the CPGE can be derived on a phenomenological level as follows:

$$j_\lambda = \sum_\rho \gamma_{\lambda\rho} I i \left(\boldsymbol{e} \times \boldsymbol{e}^*\right)_\rho = \sum_\rho \gamma_{\lambda\rho} I \hat{e}_\rho P_{\mathrm{circ}}. \tag{13}$$

$\gamma_{\lambda\rho}$ stands here for a real second-rank pseudo tensor and P_{circ} for the helicity of the radiation. The characteristic feature of the CPGE is, due to the transfer of the photon angular momentum, the reversion of the sign of the photocurrent by switching the helicity of the light from left-handed to right-handed circular polarization and vice versa.

2.2.0.5 Photon drag effect

Beside the group of photogalvanic effects in the presence or absence of an external magnetic field, there is an additional effect caused by homogeneous illumination of semiconductors with intense THz radiation. The photon drag effect is based on the transfer of the linear momentum of the absorbed photons on free carriers. In the classical frequency limit, this effect can microscopically be explained by the action of the crossed electric and magnetic field of the electromagnetic wave, similar to the ordinary Hall effect. As this effect is usually rather weak, the availability of high-power lasers, e.g. like the CO_2 laser, enabled due to the high radiation fluxes the detection of this effect [51]. Phenomenologically, the photon drag effect can be expressed by:

$$j_\lambda = \sum_{\delta\mu\nu} T_{\lambda\delta\mu\nu} q_\delta E_\mu E_\nu^*. \tag{14}$$

Due to the fourth rank tensor $\boldsymbol{T}$, there are no symmetry restrictions for this effect. Therefore, this effect causes in bulk materials a current flow along the light's propagation direction. Beside this longitudinal photon drag effect,

also a transverse component may occur in crystals of cubic symmetry. This transverse effect is however usually much weaker [56]. In QW structures, the proportionality of the drag current to the light's wave-vector $\boldsymbol{q}$ in Eq. (14) imposes the requirement of an oblique incidence of the light on the plane of the 2DEG in order to obtain a non-zero in-plane component of $\boldsymbol{q}$. There are different microscopic mechanisms of the photon drag effect, which are based on several types of optical transitions like: free carrier absorption, direct transitions between valance subbands, Landau levels, etc.

2.3 Magnetogyrotropic photogalvanic effects

As distinguished from the PGE and PDE in the previous section, the magnetogyrotropic photogalvanic effects (MPGE), which occur for illumination of any polarization, are only present for an external magnetic field. A proper choice of the geometrical configuration, i.e. the state of polarization, as well as the orientation of the magnetic field with respect to the crystallographic axis, allows to distinguish between the two different MPGEs: the linear MPGE, induced by linearly or unpolarized radiation, and the circular MPGE, sensitive to the helicity of circularly polarized light. In the beginning of this section, the phenomenological theory of both effects are presented followed by their microscopic mechanisms. In this chapter, the microscopic models will be restricted to the spin-based contributions to the LMPGE and CMPGE, while the mechanisms of an additional possible orbital contribution are developed during the discussion of the experimental results.

2.3.1 Phenomenological theory

The dependences of the photocurrents of the LMPGE and the CMPGE on the direction of the radiation's polarization and orientation of the applied magnetic field can be derived without consideration of any microscopic mechanism. This is a result of the fact that these two effects are present for the illumination of a gyrotropic nanostructure. For a medium illuminated by radiation with an

electric field $\boldsymbol{E}(\omega, \boldsymbol{q})$, the displacement field $\boldsymbol{D}(\omega, \boldsymbol{q})$ can be connected to the dielectric tensor $\epsilon_{\lambda\mu}(\omega, \boldsymbol{q})$ by the relation [57]:

$$D_\lambda(\omega, \boldsymbol{q}) = \epsilon_{0,\lambda\mu} E_\mu(\omega, \boldsymbol{q}) - i \left[\boldsymbol{G} \times \boldsymbol{E}(\omega, \boldsymbol{q})\right]_\lambda . \tag{15}$$

If the vector $\boldsymbol{G}$ is non-zero, the medium is called optically active or gyrotropic. Consequently, in gyrotropic media, there are components of a polar vector (equivalent to G_λ) and a pseudovector or axial vector (equivalent to $(\boldsymbol{G} \times \boldsymbol{E})_\lambda$) which transform under symmetry operations according to the equivalent representations of the underlying symmetry point group. In such a medium, the MPGE connects a current $\boldsymbol{j}$ (a polar vector) and a magnetic field $\boldsymbol{B}$ (a pseudovector) by $\boldsymbol{j} \sim I\boldsymbol{B}$ and can therefore be derived by symmetry considerations. In linear approximation in $\boldsymbol{B}$, the photocurrent of the MPGE can be written as [23]:

$$j_\alpha = \sum_{\beta\gamma\delta} \phi_{\alpha\beta\gamma\delta} B_\beta \frac{(E_\gamma E_\delta^* + E_\delta E_\gamma^*)}{2} + \sum_{\beta\gamma} \mu_{\alpha\beta\gamma} B_\beta \hat{e}_\gamma E_0^2 P_{\mathrm{circ}}. \tag{16}$$

$\boldsymbol{\phi}$ is here a fourth-rank pseudo tensor and $\boldsymbol{\mu}$ a regular third-rank tensor. The first term on the right-hand side represents the LMPGE, induced by linearly or unpolarized radiation, while the second term stands for the CMPGE and requires circular polarization. For a zincblende QW asymmetrically grown along the (001)-direction, Eq. (16) reduces to [23, 51]:

$$j_x = S_1 B_y I - S_2 B_y \left(|e_x|^2 - |e_y|^2\right) I + S_3 B_x \left(e_x e_y^* + e_y e_x^*\right) I + S_4 B_x I P_{\mathrm{circ}}, \tag{17}$$

$$j_y = S_1' B_x I - S_2' B_x \left(|e_x|^2 - |e_y|^2\right) I + S_3' B_y \left(e_x e_y^* + e_y e_x^*\right) I + S_4' B_y I P_{\mathrm{circ}}. \tag{18}$$

Here the coordinate system was chosen as $x \parallel [1\bar{1}0]$ and $y \parallel [110]$. The parameters S_1 to S_4 and S_1' to S_4' represent the non-zero components of the tensors $\boldsymbol{\phi}$ and $\boldsymbol{\mu}$. The first term is sensitive to even unpolarized radiation, the second and third one to linear polarization and the last term requires circularly polarized radiation. The expression of these four contributions allows to describe them by means of the Stokes parameters, which will be introduced in the following chapter, and connects this phenomenological equations with the experimentally variation of the polarization states by $\lambda/2$- and $\lambda/4$-plates. A proper choice of the orientation of the magnetic field enables an individual investigation of the single terms in Eq. (17) and (18).

2.3.2 Spin-based microscopic mechanisms

Although the photocurrents for the LMPGE and the CMPGE can be derived only on the basis of symmetry considerations, this approach reveals no information about the microscopic processes of both effects. As mentioned above, there are two contribution to the LMPGE and CMPGE, a spin-related and an orbital mechanism. Here only the spin-based microscopic mechanisms are presented.

2.3.2.1 Linear MPGE

In general, electrons, which are spin-polarized and isotropic distributed in the momentum space, are scattered asymmetrically on impurities or phonons in noncentrosymmetric media. Consequently, a spin-polarized electron is scattered predominantly in one direction [58]. This mechanism also affects the perturbation of a free electron gas due to the absorption of THz radiation. Absorption in this range usually is associated with a heating of the electron gas, followed by the subsequent relaxation of the carriers back to equilibrium. During this process, the energy and momentum conservation law has to be fulfilled and hence, the intrasubband excitation of free carriers due to this Drude-like absorption is accompanied by scattering of the electrons with acoustic or optical phonons and static defects. Such optical transitions involve virtual intermediate states and are treated in perturbation theory as second-order processes. The matrix element of a transition from the initial state $|s\boldsymbol{k}\rangle$ to the final state $|s'\boldsymbol{k}'\rangle$ can be written as [59]:

$$\hat{M}_{s'\boldsymbol{k}',s\boldsymbol{k}} = \sum_j \left(\frac{V_{e1s'\boldsymbol{k}',j\boldsymbol{k}} R_{j\boldsymbol{k},e1s\boldsymbol{k}}}{E_{e1\boldsymbol{k}} - E_{j\boldsymbol{k}} + \hbar\omega} + \frac{R_{e1s'\boldsymbol{k}',j\boldsymbol{k}'} V_{j\boldsymbol{k}',e1s\boldsymbol{k}}}{E_{e1\boldsymbol{k}} - E_{j\boldsymbol{k}'} \mp \hbar\Omega_{\boldsymbol{k}-\boldsymbol{k}'}} \right). \tag{19}$$

Here s and s' are the spin indices, j the subband of the intermediate state, $E_{e1\boldsymbol{k}}$, $E_{e1\boldsymbol{k}'}$ and $E_{j\boldsymbol{k}}$ the electron energies of the initial, final and intermediate state; $V_{e1s'\boldsymbol{k}'}$ and $R_{j\boldsymbol{k},e1s\boldsymbol{k}}$ are the matrix elements for the electron scattering and the electron interaction with the electromagnetic field with frequency ω; $\hbar\Omega_{\boldsymbol{k}-\boldsymbol{k}'}$ is the phonon energy (for elastic scattering by an impurity or defect $\hbar\Omega_{\boldsymbol{k}-\boldsymbol{k}'} = 0$). The most dominant contribution to this optical transition matrix comes from processes with intermediate states in the same subband $e1$. Considering

only one subband of a (001)-grown QW and linearly polarized radiation, two contributions arise: $\hat{M}_{\boldsymbol{k}'\boldsymbol{k}} = \hat{M}^{(0)}_{\boldsymbol{k}'\boldsymbol{k}} + \hat{M}^{(1)}_{\boldsymbol{k}'\boldsymbol{k}}$. The first element, $\hat{M}^{(0)}_{\boldsymbol{k}'\boldsymbol{k}}$, defines the absorption coefficient of the QW, while the second is given by [60]:

$$\hat{M}^{(1)}_{\boldsymbol{k}'\boldsymbol{k}} = \frac{eA}{c\omega m^*}\boldsymbol{e}\cdot(\boldsymbol{k}-\boldsymbol{k}')\sum_{\alpha\beta} V_{\alpha\beta}\sigma_\alpha(k_\beta + k'_\beta), \tag{20}$$

where $\boldsymbol{A} = A\boldsymbol{e}$ is the vector potential of the field and $\boldsymbol{e}$ the unit polarization vector. From Eq. (20) it is obvious that the scattering of electrons on phonons and defects within one spin-subband is spin-dependent. This spin-dependent asymmetry is not a consequence of the band structure modified by the spin-orbit coupling, but stems from the influence of the SOC on the scattering. Similar to the band structure, this effect arises due to the structure and bulk inversion asymmetry of the QW and is a consequence of the admixture of the conduction and valence band. The spin-dependent scattering leads to an im-

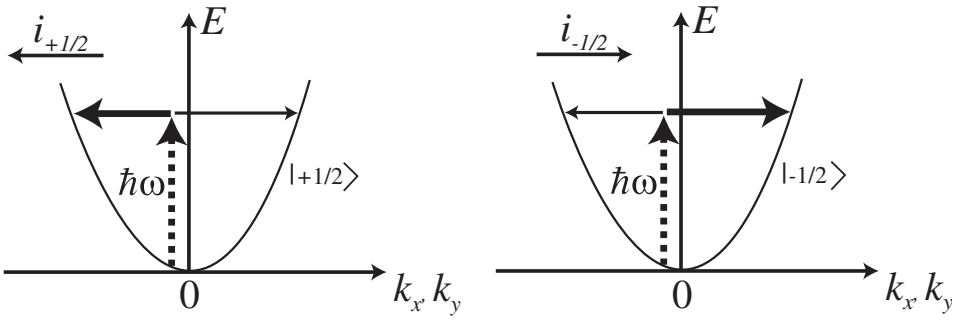

Figure 5: Asymmetric photoexcitation within one spin-subband. The rates of optical excitation with radiation energy $\hbar\omega$ from an arbitrary initial state via intermediate states is different for opposite wave vectors k_x, k_y (indicated by different thickness of horizontal arrows). The resulting flow of electrons $i_{\pm 1/2}$ is opposite for the spin-up (left side) and spin-down (right side) subband.

balance in the distribution of the photoexcited carriers in the momentum space and therefore, generates a pure spin current. Fig. 5 illustrates indirect optical transitions by absorption of linearly polarized THz radiation within the spin-up and spin-down subband, respectively. The left picture shows a transition from an arbitrary initial state k via scattering to a positive or negative final

state k' in the spin-up subband. The spin-dependent asymmetry from Eq. (20) yields a difference in the scattering probabilities (indicated by different thicknesses of arrows) for positive $0 < k'$ and negative $0 > k'$ and generates a flow of spin-up electrons $\boldsymbol{i}_{+1/2}$. For the spin-down subband, the sign of Eq. (20) inverts and a spin-down electron flow $\boldsymbol{i}_{-1/2}$ arises in opposite direction. As a result, a pure spin current, defined as a spin flow without an electric current, is formed while the average spin of the system remains zero. With respect to

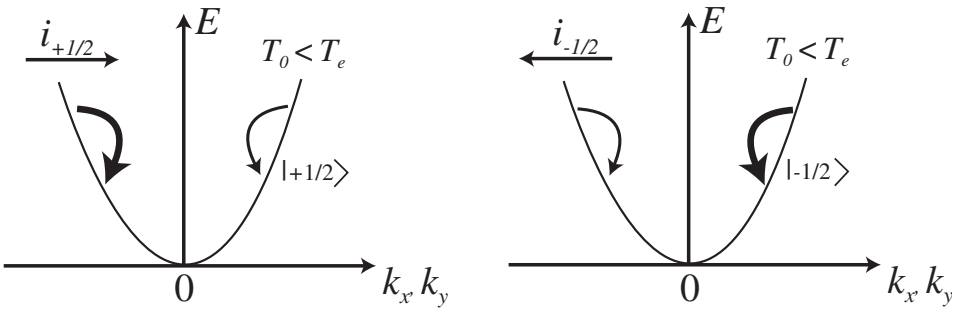

Figure 6: Asymmetric relaxation of an heated electron gas. Difference in the relaxation rates result in a flow of electrons $\boldsymbol{i}_{\pm 1/2}$ for each spin-subband (spin-up left side, spin-down right side).

the spin Hall effect, this type of scattering of electrons with opposite spin in opposite directions is called zero-bias spin separation due to the absence of an applied bias.

An additional contribution to the pure spin current is given by asymmetric relaxation processes of the excited carriers. The radiation absorption heats the electron gas and redistributes the carriers with respect to their momentum and energy. This process can be expressed by the electron temperature T_e, which in the case of electron gas heating differs from the crystal lattice temperature $T_0 < T_e$. Subsequently, relaxation processes restore equilibrium between the electrons and the lattice by, e.g., emitting acoustic phonons and the carriers lose therefore a part of their kinetic energy. Again Eq. (20) leads to a spin-dependent asymmetry for this relaxation mechanism, which gives an additional contribution to the pure spin current [61]. Like for the excitation process, the asymmetry in the relaxation is contrary for the spin-up and -down subband. The asymmetric relaxation of the heated electron gas is displayed in Fig. 6.

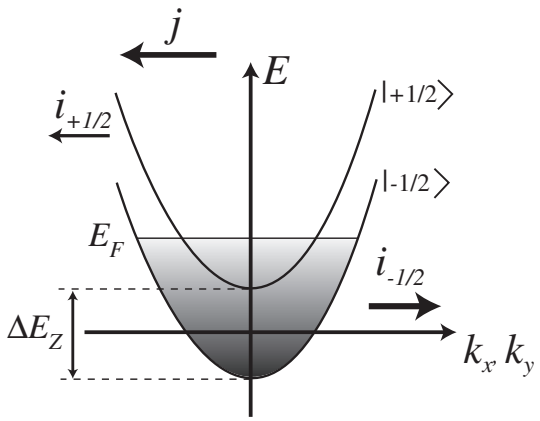

Figure 7: Zeeman splitting of subbands due to an external magnetic field. The spin-subbands are shifted by ΔE_Z. The imbalance in the population of the subbands causes an imbalance of the electron flows $i_{\pm 1/2}$ and results in an electric current j.

The total spin current, emerging from asymmetric excitation and relaxation, can be expressed by the single electron flows $\boldsymbol{i}_{\pm 1/2}$:

$$\boldsymbol{J}_{spin} = \frac{1}{2}\left(\boldsymbol{i}_{+1/2} - \boldsymbol{i}_{-1/2}\right). \tag{21}$$

The electron flows are proportional to the spin-up and -down carrier densities $n_{\pm 1/2}$ of the subband. In the case of a zero average spin S, the electron flows $\boldsymbol{i}_{+1/2} = -\boldsymbol{i}_{-1/2}$ have equal magnitude but opposite signs. Consequently, no net electric current $\boldsymbol{j} = 0$ is present. For any kind of spin polarization, e.g. the application of external magnetic fields, the pure spin current is disequilibrated ($\boldsymbol{i}_{+1/2} \neq -\boldsymbol{i}_{-1/2}$) and a net electric current arises:

$$\boldsymbol{j} = e\left(\boldsymbol{i}_{+1/2} + \boldsymbol{i}_{-1/2}\right) = 4eS\boldsymbol{J}_{spin} \quad \text{with} \quad S = \frac{1}{2}\frac{n_{+1/2} - n_{-1/2}}{n_{+1/2} + n_{-1/2}}. \tag{22}$$

Figure 7 depicts the polarization of the spins by an external magnetic field. The spin-up and -down subband are shifted against each other by the Zeeman energy ΔE_Z representing the unequal population of the subbands. After Eq. (22), the imbalance of $\boldsymbol{i}_{\pm 1/2}$ leads to an electric current $\boldsymbol{j}$, which is proportional to the average spin S and hence, to the Zeeman splitting. Due to

the excitation with linearly polarized radiation, this effect is called the linear magneto-gyrotropic photogalvanic effect (LMPGE) [22, 23, 62].

2.3.2.2 Circular MPGE

While in the previous section an applied magnetic field converts a pure spin current into an electric current, even the spin polarization of an electron gas itself can drive a current [63]. This effect, also known as the spin galvanic effect, is called the circular magneto-gyrotropic photogalvanic effect. The formation of this current is based on asymmetric spin-flip relaxation processes. In contrast to the LMPGE, for the CMPGE the $\boldsymbol{k}$-linear terms in the Hamiltonian are essential. The connection of an electric current $\boldsymbol{j}$ with the spin $\boldsymbol{S}$ of the system can be phenomenologically expressed by [56]:

$$j_\alpha = \sum_\gamma Q_{\alpha\gamma} S_\gamma. \tag{23}$$

Here $Q_{\alpha\gamma}$ is a second-rank pseudo-tensor and α, γ indicate the coordinates. For the symmetry of a (001)-grown zinc blende QW, Eq. (23) reduces to $j_x = Q_{xy} S_y$ and $j_y = Q_{yx} S_x$. Hence, in this case a spin polarization in the plane of the 2DEG is required for the observation of a photocurrent. An in-plane spin component can be achieved by initially optical spin orientation along the normal of the 2DEG, and subsequent Larmor precession about an applied in-plane magnetic field. The initial spin orientation S_{0z} by circularly polarized THz radiation can be derived from Eq. (19) and is caused by a transfer of the angular momentum of the photons to the electrons in a 2DEG. The intraband (Drude-like) absorption of circularly polarized light results in a redistribution of the electrons between the single spin subbands, which is called

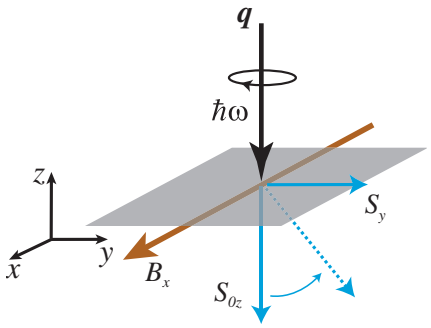

Figure 8: Precession of an initial optical spin-orientation S_{0z} about an in-plane magnetic field B_x.

monopolar optical orientation of electron spins [59]. These intraband transitions always involve virtual intermediate states in the complex valence band and are accompanied by scattering with phonons or defects. The steady-state spin polarization S_{0z} can be rotated into the plane by, e.g., a magnetic field B_x, which results in a spin component along the y-direction [64]:

$$S_y = -\frac{\omega_L \tau_{s\perp}}{1+(\omega_L \tau_s)^2} S_{0z} \quad \text{with} \quad \omega_L = g^* \mu_B B_x/\hbar, \tag{24}$$

where $\tau_s = \sqrt{\tau_{s\parallel}\tau_{s\perp}}$ is the total spin relaxation time with contributions from any relaxation mechanism, $\tau_{s\parallel}, \tau_{s\perp}$ are the longitudinal and transversal spin relaxation times and ω_L is the Larmor frequency. This mechanism is illustrated in Fig. 8.

The process, which yields an electric current as a consequence of the in-plane spin S_y, is illustrated in Fig. 9 (a) and (b). On the left-hand side, the energy spectrum $E(k_x)$ is depicted including the $\boldsymbol{k}$-linear terms from Eq. (6), which shifts the minimum of the single subbands to $k_{x_\pm}$. The spin orientation is expressed by the imbalance of the spin-up and -down band. The system restores to equilibrium between the spin subbands by $\boldsymbol{k}$-dependent spin-flip relaxation processes [65]. Electrons with spins pointing in y-direction are scattered along k_x. These relaxation processes are illustrated by bent arrows. The matrix element $\hat{M}_{\boldsymbol{k'k}}$ for such a transition within one subband but a change of the spin can be written as [56, 65]:

$$\begin{aligned} \hat{M}_{\boldsymbol{k'k}} &= A_{k'k}\hat{I} + \boldsymbol{\sigma}\cdot\boldsymbol{B}_{k'k} \\ \text{with} \quad \boldsymbol{\sigma}\cdot\boldsymbol{B}_{k'k} &= v(\boldsymbol{k}-\boldsymbol{k'})\left[\sigma_x(k'_y+k_y) - \sigma_y(k'_x+k_x)\right] \end{aligned} \tag{25}$$

Here $\hat{I}$ is the unit matrix. The scattering amplitude $v(\boldsymbol{k}-\boldsymbol{k'})$ in the second term depends on the difference of the initial and final wave vector $\boldsymbol{k}-\boldsymbol{k'}$. As a consequence, the possible relaxation processes by elastic scattering from the initial state $|+1/2, k_x\rangle_y$ to the final state $|-1/2, k'_x\rangle_y$ have different probabilities, shown in Fig. 9 by different thickness of the bent arrows. While transitions shown as dashed arrows are of equal strength, the transitions shown by continuous arrows occur with different probability. This difference leads to an asymmetric distribution of the carriers around the single spin subband

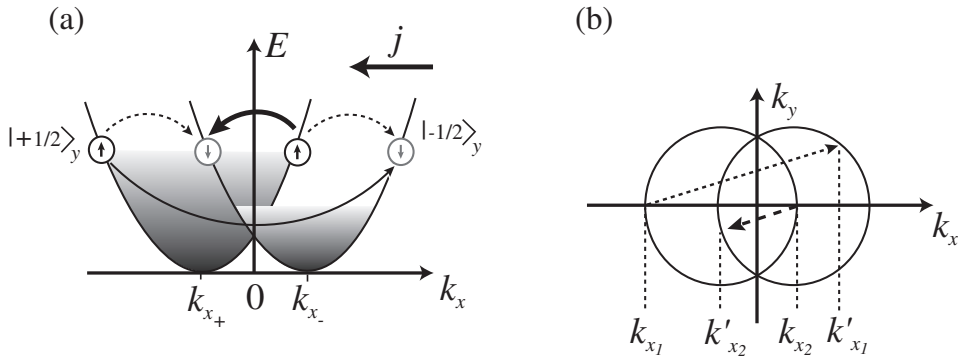

Figure 9: Origin of the spin-galvanic effect in the presence of $\boldsymbol{k}$-linear terms in the Hamiltonian. (a) In the one-dimensional model the optical spin-orientation yields a difference in the population of the spin-up $|+1/2, k_x\rangle_y$ and spin-down subband $|-1/2, k_x\rangle_y$. The rate of spin-flip scattering depends on the difference of the initial and final wave vector k_x (different thickness of arrows) and causes an asymmetric population of the single spin-subbands and hence an electric durrent j. (b) Transitions due to spin-flip scattering in two dimensions.

minimum k_{x_+} and k_{x_-}. Hence, a current j is generated. This model for one dimension shows the main principle of the current formation, but does rather not allow a current for the case of elastic scattering due to $|k_x| = |k'_x|$. In order to observe a current, inelastic scattering has to be taken into account, or like shown in Fig. 9 (b), the model has to be extended to the two dimensional case, where $k_y \neq 0$. Microscopically, Eq. (23) can be expressed in the following way:

$$j_x = Q_{xy} S_y \sim e n_e \frac{\beta^{(1)}_{yx}}{\hbar} \frac{\tau_p}{\tau'_s} S_y \quad \text{and} \quad j_y = Q_{yx} S_x \sim e n_e \frac{\beta^{(1)}_{xy}}{\hbar} \frac{\tau_p}{\tau'_s} S_x. \tag{26}$$

Here τ'_s is the spin relaxation time due to the Elliot-Yafet mechanism, from which the spin-dependent terms in Eq. (25) stems [65], and which determines the current of the CMPGE. The most characteristic feature of the CMPGE can be readily seen from Eq. (24) and (26): a change of the radiation's helicity from left-handed circular polarization to right-handed changes the sign of S_{0z} and subsequently of S_y (or S_x) and therefore reverses the sign of j_x (or j_y). In contrast to the LMPGE, this photocurrent is not spin polarized because

the same number of carriers with spin-up and spin-down move with the same velocity in the same direction, respectively [63].

3 Samples and experimental methods

In this chapter, all structures investigated in this work are briefly discussed. Thereby, the detailed growth structure of the different samples and their energy band profiles are presented. After that, the THz laser systems used to generate the photocurrents are introduced, followed by the laser beam guiding system for the detection, control and manipulation of the radiation during the measurements. The experimental methods also involve the different orientations of the sample relative to the applied magnetic field and the radiation beam. Finally, the electronic setups used to detect the photocurrent signals are explained.

3.1 Description of studied samples

The indium antimonide QWs investigated in this work were grown by molecular beam epitaxy on (001)-oriented, non-miscut GaAs substrates. In order to realize InSb low-dimensional structures, this material is confined on both sides by an $In_{1-x}Al_xSb$ barrier of different compositions [17]. In general, the growth of high-quality InSb is still a difficult task. The disadvantages compared to the growth of GaAs- or Si-based low-dimensional structures is that there are no lattice-matched III-V insulators available as a substrate material. However, despite the large lattice mismatch between GaAs and InSb of 14.6%, GaAs substrates represent a reasonable choice due to their availability in high quality at rather low costs. Nevertheless, the mismatch complicates the structure growth resulting in the appearance of misfit dislocations at the QW interfaces [66] and in structural deficiencies, which can lead to a change in the electric properties along the growth direction of the InSb QW samples [67].

In order to avoid this deficiencies, first a 200 nm AlSb nucleation layer was grown on the cleaned and buffered GaAs substrate followed by a 3 μm thick $In_{1-x}Al_xSb$ accommodation layer. The detailed growth structures of the investigated samples are shown in Fig. 10. AlSb with a mismatch of only 6% and $In_{1-x}Al_xSb$ with a mismatch <1% compared to InSb allows a successive adjustment of the lattice parameters. Hence, this kind of matching the single layers between the substrate and the InSb QW is a good method to avoid defects

and ensures atomically abrupt interfaces [16]. By this, one tries to achieve the desired good crystallographic properties like e.g. for GaAs heterostructures.

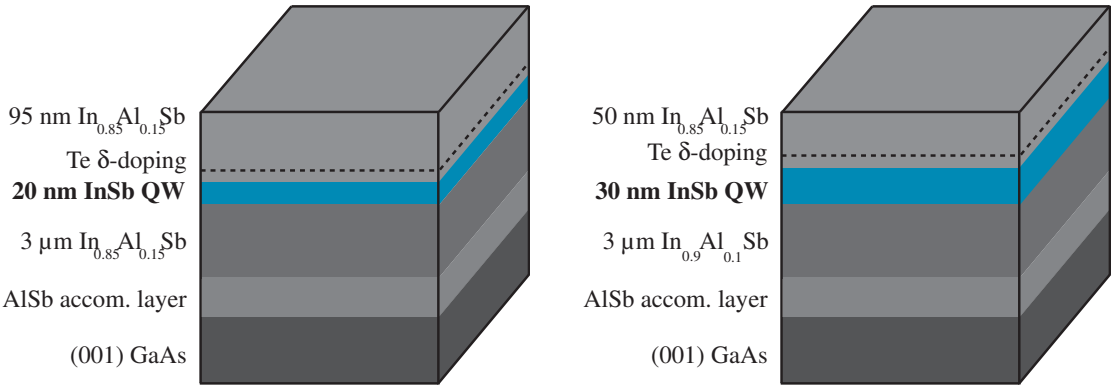

(a) 20 nm wide InSb QW (type A) (b) 30 nm wide InSb QW (type B)

Figure 10: Detailed growth structure of InSb/InAlSb quantum well structures grown on (001)-oriented GaAs substrate used in the experiments.

In this work, two different sets of InSb-based QWs, which mainly vary in the quantum well thickness, were used. The samples of type A have a 20 nm thick QW confined between two $In_{0.85}Al_{0.15}Sb$ barriers. The samples of type B have a 30 nm thick QW, where the lower barrier layer is made up of $In_{0.90}Al_{0.10}Sb$ and the upper barrier has the same composition as in type A. Furthermore, the upper barrier of both sets contains a Te-modulation-doped layer, which is placed 20 nm above the well and leads to an asymmetry along the growth direction. The doping provides free carriers, which are confined to the well. Hence, the QW with 20 nm width contains a two-dimensional electron gas with a carrier density of $N_s \approx 3 \times 10^{11}$ cm^{-2} and a mobility of $\mu_e \approx 5 \times 10^4$ cm^2/V s below 77 K. The 30 nm wide well is characterized by $N_s \approx 5 \times 10^{11}$ cm^{-2} and $\mu_e \approx 15 \times 10^4$ cm^2/V s.

The single-side doping of the structures leads to an asymmetric energy band profile, which is given for both samples in Fig. 11. The conduction band E_c and the wave functions of the first subband were calculated by a self-consistent Schrödinger-Poisson model [17, 69]. Here, the energy scale is defined with respect to the Fermi energy being equal to $E = 0$ meV. The figure shows

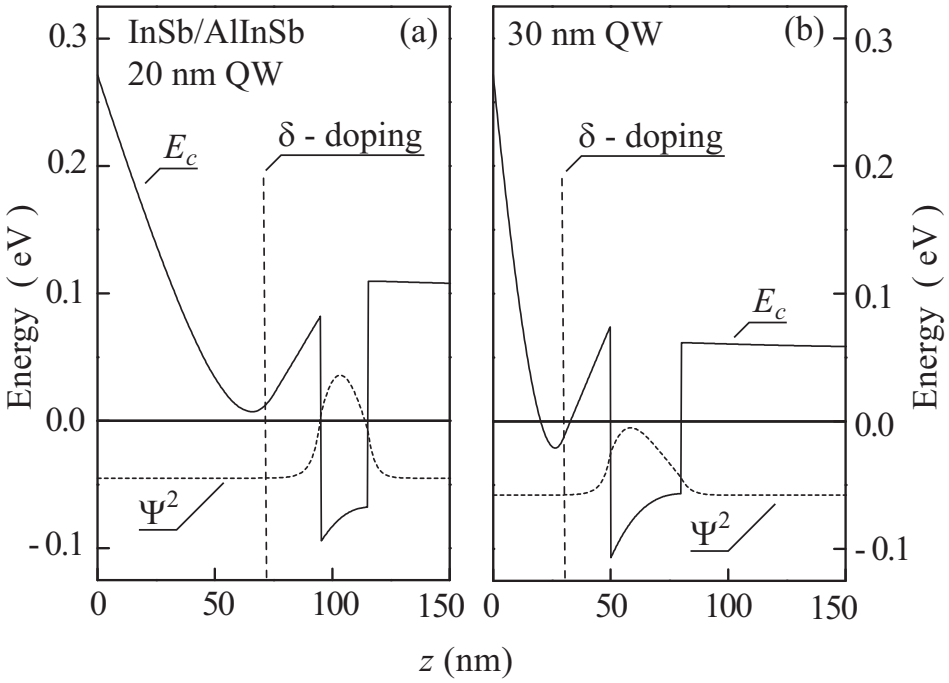

Figure 11: Conduction-band profile and electron wave function of the 20 nm wide (a) and the 30 nm wide (b) InSb QW structure within a self-consistent Schrödinger-Poisson model [68].

the position of the δ-doping layer and the resulting bending of the conduction band. Furthermore, the calculations illustrate the asymmetry of the QW due to the single-side doping and the difference in the barrier composition. As a consequence, it can be clearly seen that in both type of samples the wave functions of the electrons are shifted off the center of the quantum well towards the upper barrier cap containing the doping layer.

3.2 THz laser systems

In order to generate photocurrents in the structures described above, molecular lasers optically pumped by CO_2 lasers were applied. The CO_2 laser exploits vibrational-rotational transitions between the energy levels of the CO_2 molecule, leading to emission of radiation in the mid-infrared range. Thereby, this kind of laser represents the most important pump source for THz lasers, as strong rotational-vibrational absorption lines of many molecules lie in its

tunable range between 9.2 and 11.2 μm [51]. In the experiments, two different operation modes are used: continuous wave (*cw*) and pulsed [70, 71].

The fundamental idea is to excite vibrational-rotational transitions in molecules with a permanent electric dipole moment, e.g. NH_3 or CH_3OH, by the mid-infrared radiation (MIR) of the CO_2 laser. The transitions between the rotational states of the molecules lead to an emission of radiation in the THz range [72]. This principle is similar for the pulsed and the *cw* operation mode. Three strong lines of the pulsed system are used for the excitation of the photocurrents: 90.5, 148 and 280 μm. These lines correspond to photon energies of 13.7, 8.4 and 4.4 meV, respectively, and their radiation power lies in the kW range. By contrast, the *cw* system provides THz radiation in the mW range with a wavelength of 118.8 μm (10.4 meV). The emitted THz radiation exhibit a well defined degree of linear polarization, whose orientation is determined by the angular momentum selection rules of the pump and THz transitions. For the *cw* system, this orientation is horizontal, while for the pulsed, it is vertical for all wavelengths used in the experiments.

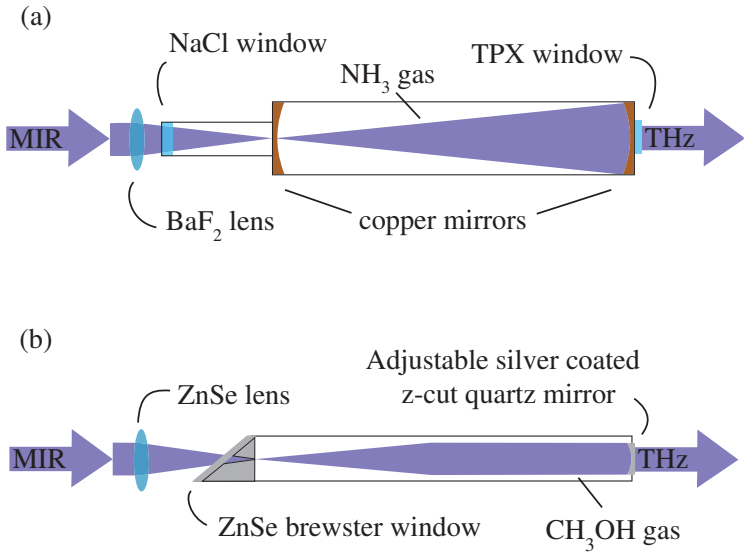

Figure 12: Resonators of (a) the pulsed and (b) *cw* laser system pumped by the MIR beam from the CO_2 laser including all optical components.

Figure 12 (a) and (b) illustrate the setup of the pulsed and *cw* molecular laser system, respectively. In the pulsed system, the MIR beam is focused by a BaF_2 lens into a glass tube, which contains the laser gas NH_3. A NaCl window allows to couple the beam into the resonator. The cavity of the molecular laser is formed by two spherical gold coated copper mirrors for multiple reflections and maximal absorption of the pump beam, and contains holes for in- and out-coupling of the beam. A polymer window (TPX) closes the cavity and ensures that only THz radiation is coupled out and MIR radiation gets absorbed. The pulsed laser system provides short pulses with a duration of 100 ns leading to high pulse powers up to 40 kW. Figure 13 (a) shows the temporal shape of such a short laser pulse. These pulses are repeated with a frequency of 1 Hz, which results in a small duty cycle of about 10^{-7}. By this, the heating of the sample is avoided. The beam of the radiation forms an almost Gaussian shape. Its spatial distribution is measured by a pyroelectric camera and displayed in Fig. 13 (b).

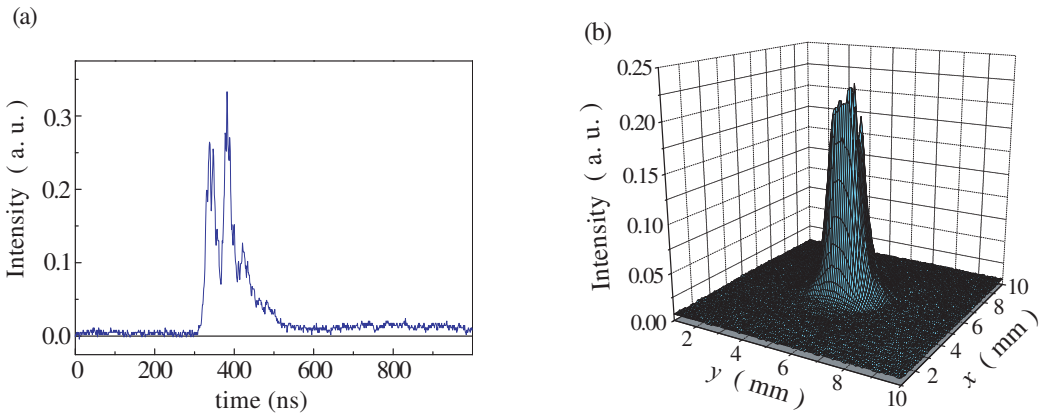

Figure 13: (a) Temporal shape of a THz laser pulse, (b) spatial intensity distribution of a typical THz beam with almost Gaussian shape.

In contrast to the pulsed laser system, the *cw* system operates at much less radiation power [73]. The setup of this laser is depicted in Fig. 12 (b). The emitted MIR radiation is, similar to the pulsed system, coupled into a second cavity by a ZnSe lens. The ZnSe Brewster window in front of the focus forms the gas tube and ensures a huge degree of linear polarization of the emitted THz beam. In the experiments, the laser gas CH_3OH was used to obtain

Laser	**Wavelength**	$\boldsymbol{E_{ph}}$	**Power**
pulsed	90.5 μm	13.7 meV	10.9 kW
pulsed	148 μm	8.4 meV	20.9 kW
pulsed	280 μm	4.4 meV	2.4 kW
cw	118.8 μm	10.4 meV	2.0 mW

Table 2: Wavelengths, photon energies E_{ph} and powers of all laser lines used in the experiments.

a radiation wavelength of 118.8 μm. The cavity is closed by an adjustable, silver coated z-cut quartz mirror in order to let the linear polarization pass unaffected. By a proper choice of the position of this mirror, it is possible to set the radiation's wavelength, as well as its mode structure. The power of the *cw* system is about 2 mW, and in particular multiple orders of magnitude smaller than in the pulsed system. Table 2 lists all wavelengths of the pulsed and the *cw* laser system used in the experiments and gives the corresponding photon energies E_{ph}, as well as the average radiation powers.

3.3 Experimental setups and sample alignments

The previous section discussed the generation of the THz radiation. Now, all experimental components involved in the manipulation of the radiation and the detection of the photocurrents are described. Additionally, a detailed overview of the different alignments of the sample with respect to the illuminating THz beam and the applied magnetic field will be presented.

Figure 14 shows schematically the optical path of the THz beam through different optical components. The radiation beam ends in an optical cryostat at the sample surface. This experimental setup is almost identical for both, the pulsed and the *cw* laser system. The beam is first splitted by an mylar film in order to extract a small part of the radiation. This part is detected by a reference detector. In order to measure the power of the THz beam, in the *cw* system a pyroelectric detector and in the pulsed laser setup a photon drag detector is used. The system is calibrated by determining the ratio of

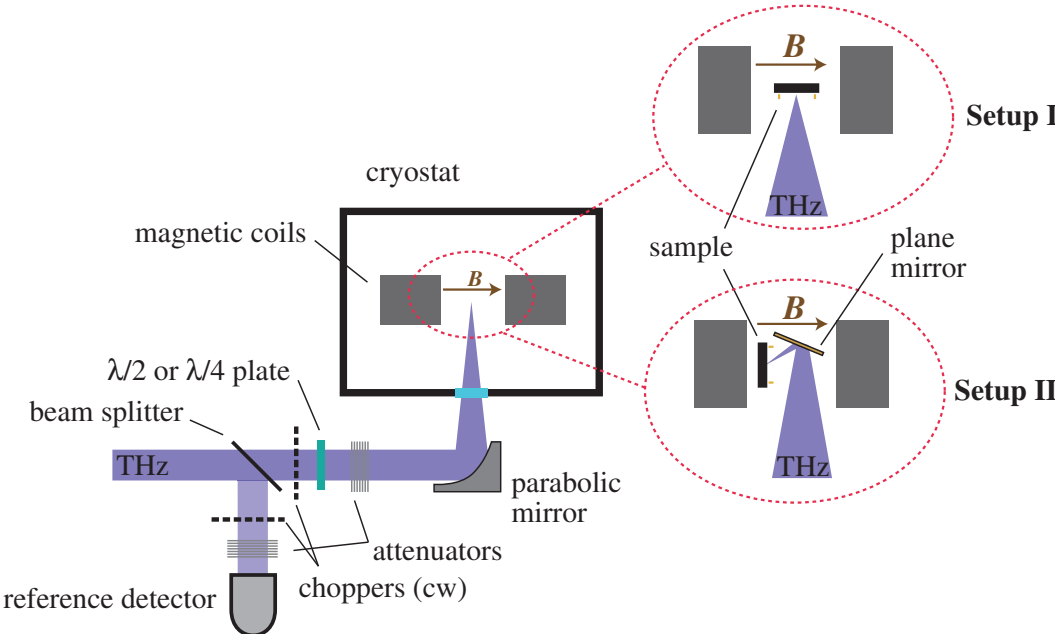

Figure 14: Optical path of the THz beam with all components of the experimental setup. Two different geometries were used: Setup I for in-plane magnetic field and normal incidence of radiation; Setup II for normal magnetic field and oblique incidence of radiation.

the radiation power at the sample position and at the reference detector. This ratio allows to evaluate the radiation power, which reaches the sample during the measurements. By normalizing the photocurrent signal on the radiation power at the sample position, all power fluctuations of the laser system are eliminated and therefore any effects of these fluctuations on the photocurrent dependencies can be excluded.

In the *cw* system, the modulation of the THz beam by a chopper allows the use of standard lock-in technique for the detection of the photocurrents. In order to study the current's dependence on the radiation power, the THz beam can be attenuated by a number of plates, consisting of materials like teflon or polyethylene. These materials are semitransparent for the THz lines used in this work and their transmission can be varied by the thickness of the plates. A gold-coated parabolic mirror focuses the beam on the the sample in the center of an optical cryostat with a typical spot size of about 2 mm. In order

to generate magnetic fields up to ±7 T, optical Janis and Oxford cryostats are used. Both cryostats contain superconducting split-coils, which produce a homogeneous field at the sample position. Furthermore, the temperature of the sample can be adjusted to a wide range between 1.7 and 300 K. Beside the detection of the photocurrent, also the transmission of THz radiation through the sample is investigated in the presence of a magnetic field. For this purpose, a Golay cell is placed behind the sample, which allows to detect the power of the transmitted radiation.

In the experimental setup, a variation of the polarization state was accomplished by $\lambda/2$- and $\lambda/4$-plates. These plates consist of x-cut quartz. The material is transparent in the THz range and exhibits an anisotropy of the refraction index $n(\omega)$. By a proper choice of the thickness of the plate, the linear polarization can be rotated by an angle α. Furthermore, the plate's thickness can be chosen to convert linear polarized radiation into elliptically and circularly polarized light. The rotation of the $\lambda/4$-plate is described by the angle φ between the initial linear polarization and its optical axis. The two angles α and φ allow to connect the Stokes parameters with the rotation of the λ-plates [74]:

$$\frac{s_1}{s_0} = \frac{|E_x|^2 - |E_y|^2}{|E|^2} = -\cos(2\alpha) = -\frac{1+\cos(4\varphi)}{2}\,, \tag{27}$$

$$\frac{s_2}{s_0} = \frac{E_x E_y^* + E_y E_x^*}{|E|^2} = \sin(2\alpha) = \frac{\sin(4\varphi)}{2}\,, \tag{28}$$

$$\frac{s_3}{s_0} = \frac{\mathrm{i}(E_x E_y^* - E_y E_x^*)}{|E|^2} = -P_{\mathrm{circ}} = -\sin(2\varphi)\,. \tag{29}$$

For these equations, it was assumed that electric field $\boldsymbol{E}$ of the radiation lies in a xy-plane and the beam propagates along -z. The parameters s_1 and s_2 in Eq. (27) and (28) describe the linear polarization. This state of polarization occurs for both $\lambda/2$- and $\lambda/4$-plates, and is therefore connected to α and φ. The third parameter s_3 describes fully circularly polarized light and is proportional to its helicity, $P_{\mathrm{circ}} = \sin(2\varphi)$, which is equal to +1 and -1 for right- and left-handed circular polarization, respectively. The parameter $s_0 = |E|^2 = I$

describes the radiation intensity and does not contain any information about the polarization state of light.

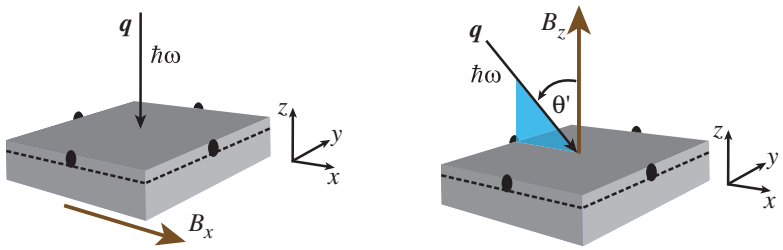

(a) Setup I (b) Setup II

Figure 15: Sample geometries and orientation of the incidence of light and magnetic field direction.

In Fig. 15, the different orientations of the THz beam and the applied magnetic field used in the experiments are depicted. The edges of the samples are oriented along the crystallographic axes $x \parallel [1\bar{1}0]$ and $y \parallel [110]$. The axis $z \parallel [001]$ is parallel to the growth direction. Two setups are used, which mainly differ by the orientation of the magnetic field. In setup I, the radiation beam is aligned parallel to z and normal to the 2DEG. An external magnetic field $\boldsymbol{B}$ is applied along the x-axis lying in the plane of the 2DEG. In setup II, the incident beam, defined by the wavevector $\boldsymbol{q}$, is tilted by an angle θ' with respect to the z-axis and lies in the x-z-plane, which is depicted by the blue triangle in Fig. 15 (b). In this setup, the field is aligned along z and hence is oriented normal to the 2DEG. The two configurations are performed using setup I and II shown in Fig. 14. In setup II, a plane, metallic mirror directly in front of the sample is used in order to realize simultaneous normal magnetic field and oblique incidence of the THz beam. Ohmic Indium contacts are alloyed to the center of the sample edges and detect the photocurrents parallel and perpendicular to the in-plane magnetic field or the plane of oblique incidence, respectively.

In Fig. 16 (a) and (b), the circuits used in the pulsed and the *cw* system are depicted. The photocurrents induced by pulsed THz radiation are detected in a closed circuit via the voltage drop over a 50 Ω resistance without applied bias. An amplifier with differential input and a gain coefficient of 20 dB was used to

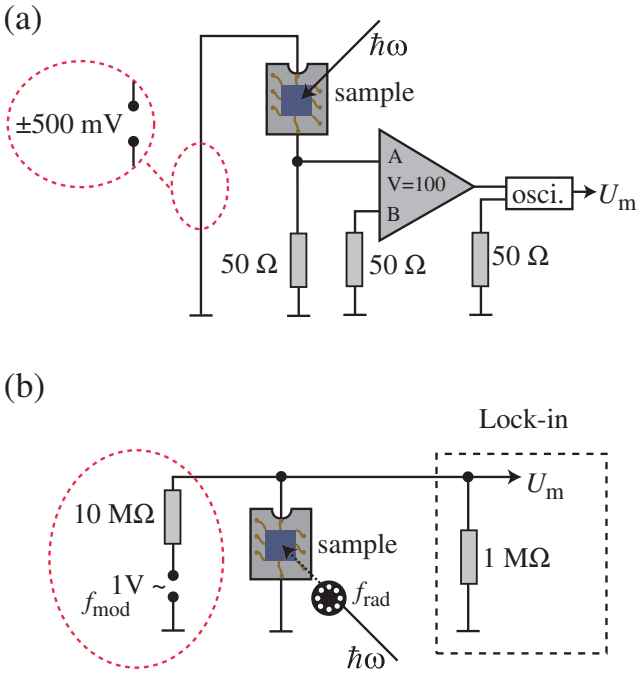

Figure 16: Electric circuits used for the detection of the photocurrents induced by the pulsed (a) and the *cw* (b) laser system. Red circles indicate the modifications for the setups used in the photconductivity experiments.

increase the detected pulsed signal. By digital high-bandwidth oscilloscopes, the signal U_m was recorded with an high temporal resolution. In order to investigate the change of the conductivity by illumination of the sample, a bias of ±500 mV was applied to the sample, shown in the red dashed circle in Fig. 16 (a). In the *cw* system, the signal U_m was detected by the voltage drop over the sample (see Fig. 16 (b)). For the photoconductivity experiments, currents of 100 nA, modulated by a frequency f_{mod}, and two series-connected Lock-ins were used to detect the change of the voltage drop due to the THz illumination.

4 Magnetic field independent photocurrents

Additionally to the magnetic-field-induced photocurrents presented in the following chapters, this chapter is dedicated to magnetic-field-independent signals. The study of these currents allows to obtain information about the symmetry properties of the investigated InSb QW structures, and is therefore important for the understanding of the magnetically sensitive signals. The phenomenological theory of the linear and the circular photogalvanic effect, which was introduced in section 2.2, allows to derive the LPGE's and CPGE's dependence of the photocurrents on the light polarization and the angle of incidence. These phenomenological equations are solely based on symmetry considerations. Consequently, the comparison of the experimentally observed photocurrents with the phenomenological equations allows to draw conclusions about the corresponding symmetry point group of the investigated structure.

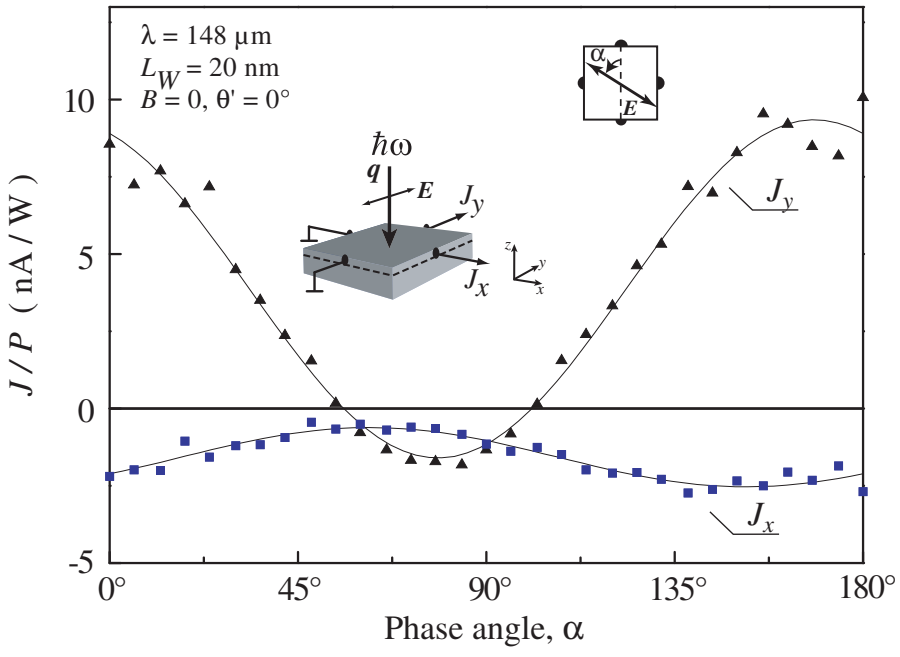

Figure 17: Dependence of the photocurrent J_x and J_y on the orientation of the light's electric field $\boldsymbol{E}$ for the 20 nm wide InSb QW structure. The inset shows the experimental geometry.

First, the experimental observations of the 20 nm wide InSb QW structures (type A) are presented. Illumination with THz radiation at normal incidence of light without magnetic field yields a photocurrent along the $x \parallel [1\bar{1}0]$, as well as the $y \parallel [110]$ direction. Figure 17 shows both signals depending on the orientation of the linear polarization. The currents exhibit a well-defined dependence on the direction of the light's electric field vector $\boldsymbol{E}$. In addition, also the excitation with circularly polarized THz radiation yields a photocurrent for normal incidence of the beam. Figure 18 illustrates the photocurrents for various angles φ, which represents the rotation of a $\lambda/4$ plate. The resulting different polarization states are displayed on the top of Fig. 18 and are given by the Stokes parameters from Eq. (27) to (28). It can be seen that also for

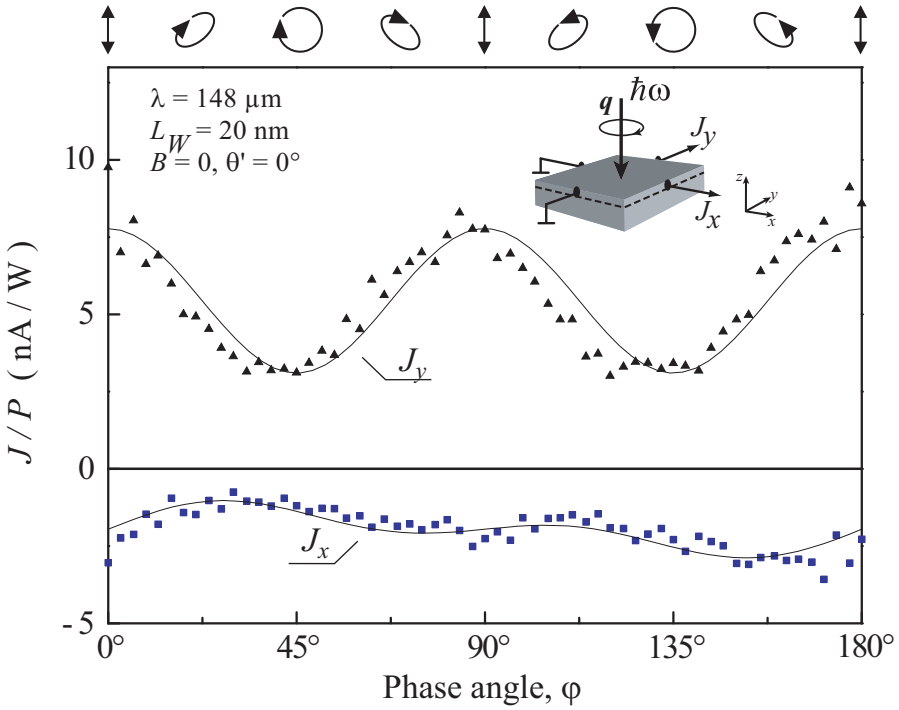

Figure 18: Helicity dependence of the photocurrent J_x and J_y.

circularly ($\varphi = 45°$ and 135°) and elliptically polarized light, a photocurrent appears for both crystallographic directions x and y. Similar dependences of the photocurrents in the 20 nm structures are observed for various wavelengths and in a wide temperature range from room temperature down to 4.2 K. In contrast to the occurrence of a photocurrent in the 20 nm wide QW structure,

in the 30 nm wide well (type B) no currents are detected at normal incidence of light neither for linearly nor for circularly polarized radiation.

The observation of the photocurrents in the sample of type A indicates a reduction of its symmetry. This follows from the phenomenological theory of the photogalvanic effects. In general, asymmetric zinc-blende structure based QWs grown on (001) exact oriented substrates belong to the C_{2v} symmetry point group. For this symmetry group, the phenomenological equation (12) for the LPGE reduces to [51]:

$$j_x^{LPGE} = \chi_{xxz} \left(E_x E_z^* + E_z E_x^* \right), \tag{30}$$

$$j_y^{LPGE} = \chi_{yyz} \left(E_y E_z^* + E_z E_y^* \right). \tag{31}$$

From this equation, it becomes apparent that a current resulting from the LPGE can in a structure of C_{2v}-symmetry only be induced by an oblique incidence of light, as this effect requires a component of the light's electric field vector $\boldsymbol{E}$ along the z-direction. The same argument holds for the CPGE. The phenomenological equations for this effect (see (Eq. 13)) can be written for C_{2v}-symmetry as [51]:

$$j_x^{CPGE} = \gamma^{(1)} \hat{e}_y I P_{circ}, \tag{32}$$

$$j_y^{CPGE} = \gamma^{(2)} \hat{e}_x I P_{circ}. \tag{33}$$

Similar to the LPGE, the CPGE requires oblique incidence of the THz beam for this symmetry group. This is expressed by the components of the unit vector of the light propagation $\hat{e}_{x,y}$ in Eq. (32) and (33), which vanish for normal incidence.

While the absence of any photocurrent for normal incidence of light in the 30 nm QW structure is in full agreement with Eqs. (30) to (33), the observation of a photocurrent for the 20 nm wide samples indicates that this structure does not belong to the C_{2v} symmetry group, but its symmetry is reduced to those of C_s or even to C_1. The origin of the symmetry reduction can be, e.g., a miscut of the surface or a in-built strain. This would lead to the disappearance of certain elements of the symmetry point group and hence, allow the occurrence of photocurrents even for normal incidence of light. The

absence of any currents for the 30 nm QW structures, however, proves that this type of sample definitely belongs to the C_{2v} group.

5 Photocurrents in the presence of an in-plane magnetic field

In this chapter, the experimental observation and detailed study of the magnetogyrotropic photogalvanic effects in InSb quantum wells are presented. It will be demonstrated that illumination of this narrow gap material with THz radiation in the presence of an in-plane magnetic field results in a dc electric current. By applying radiation of different polarization, both the linear and circular MPGE are analyzed. The first one can be induced by linearly polarized or even unpolarized radiation, while the CMPGE results in a light helicity-dependent photocurrent and reverses its sign by switching the sign of the circular polarization. Thereby, the behavior of the photocurrents is studied upon variation of the magnetic field strength, polarization, temperature, as well as the radiation's wavelength. The results are analyzed in terms of the microscopic models based on the asymmetric relaxation of carriers in the momentum space. It is shown that the observed strong nonlinearity for the LMPGE and a pure linear magnetic field dependence of the CMPGE stem from an interplay between spin-related and spin-independent roots of both MPGEs [21].

5.1 Linear MPGE

In this section, the experimental observation of the photocurrents arising from excitation with linearly polarized radiation is presented. Polarization dependences of the LMPGE signals show that the current formation stems from asymmetric relaxation processes after the electron gas was heated. Accordingly, the electron gas heating is proved by photoconductivity measurements. The experimental results are finally discussed in the framework of the two competing mechanisms of the LMPGE.

5.1.1 Experimental results

The irradiation of the InSb QW structures with linearly polarized radiation may result in signals due to the LMPGE and exclude the CMPGE. For this

purpose, the photocurrent signals are measured perpendicular as well as parallel to the in-plane magnetic field and the THz beam is adjusted to normal incidence. The geometrical configuration for measurements with linear polarization is illustrated in the inset of Fig. 19. In the presence of a magnetic field B_x, a current is detected along the y-direction in the 20 nm, as well as in the 30 nm structure. The observed signal varies with the magnetic field strength and its sign depends on the magnetic field direction. In addition to the field dependent current, also the magnetically independent current presented in chapter 4 is present, which is however not in the focus of this chapter. Hence, we extract the field-dependent part as follows:

$$J_y(|B|) = \left[J(B_x > 0) - J(B_x < 0)\right]/2. \tag{34}$$

In Fig. 19, the normalized current J_y/P is illustrated as a dependence of the magnetic field B_x for the low power *cw* radiation at $T = 35$ K. The current increases almost linearly with the field B_x up to about 2 T. For higher fields, a nonlinear dependence emerges. In contrast to the low field range, the sign of the current's slope dJ_y/dB_x becomes negative, the current decreases and even vanishes at about 7 T. A qualitatively similar magnetic field behavior is found in a wide temperature range up to 120 K in all samples.

The inset on the right-hand side in Fig. 19 shows the current J_y/P dependent on the orientation of the linear polarization, which is varied by a $\lambda/2$ plate. The rotation of the electric field vector $\boldsymbol{E}$ of the radiation is given by the azimuth angle α, defined as the angle between the y-axis and the $\boldsymbol{E}$-field vector, as shown in the inset. The polarization dependence is measured at a fixed magnetic field $B_x = +5$ T for different temperatures in both samples of type A and B (left and right scale). At liquid helium temperature, a photocurrent J_y is detected, which is almost independent of the polarization orientation. A comparison of the 20 nm and the 30 nm sample reveals that in the wider well structure the current is larger by one order of magnitude. At higher temperatures, the signals become polarization dependent. This dependence can be well fitted by $J_y = J_1 + J_2 \cdot \cos(2\alpha)$. For the longitudinal current J_x (not shown), a similar behavior is observed. For this direction, only a polarization dependent current $J_x = J_3 \cdot \sin(2\alpha)$ is measured. The experiment reveals

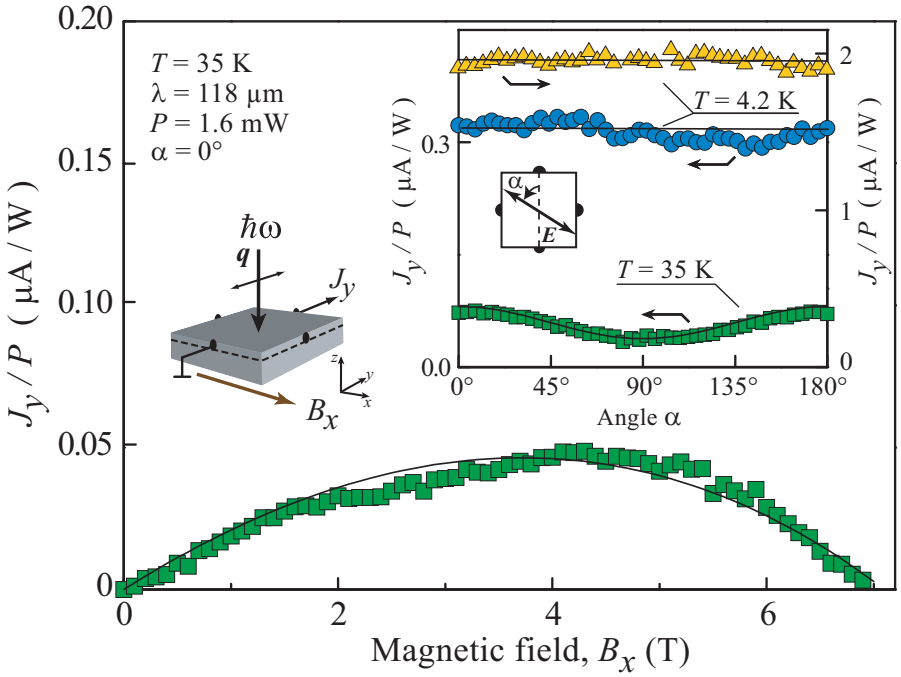

Figure 19: Transvers photocurrent J_y normalized by the radiation power P as a function of the in-plane magnetic field B_x for linearly polarized radiation of $\lambda = 118$ μm from the *cw* laser system and $T =$ 35 K. The line is fitted after Eq. (50). The left inset shows the experimental geometry. The right inset shows the photocurrent's dependence on the azimuth angle α measured for $T = 4.2$ and 35 K at fixed B_x $= +5$ T. The triangle symbols correspond to the 30 nm, and the circle and squared symbols to the 20 nm QW structures.

that particular at low temperatures, the polarization-dependent photocurrent contributions $J_2 \cdot \cos(2\alpha)$ and $J_3 \cdot \sin(2\alpha)$ are substantially smaller than the polarization-insensitive term J_1. Thus, we focus in the following only on the transverse, polarization-independent photocurrent J_y.

Figure 20 shows the current J_y/P induced by the high power pulsed laser radiation of 148 μm as a function of the $\boldsymbol{B}$-field for different temperatures. The experimental geometry is identical to the setup of the *cw* system measurements and the signals behave similarly. In the low field range, J_y is proportional to B_x up to a maximum value of about 3 T. For high magnetic fields, the current

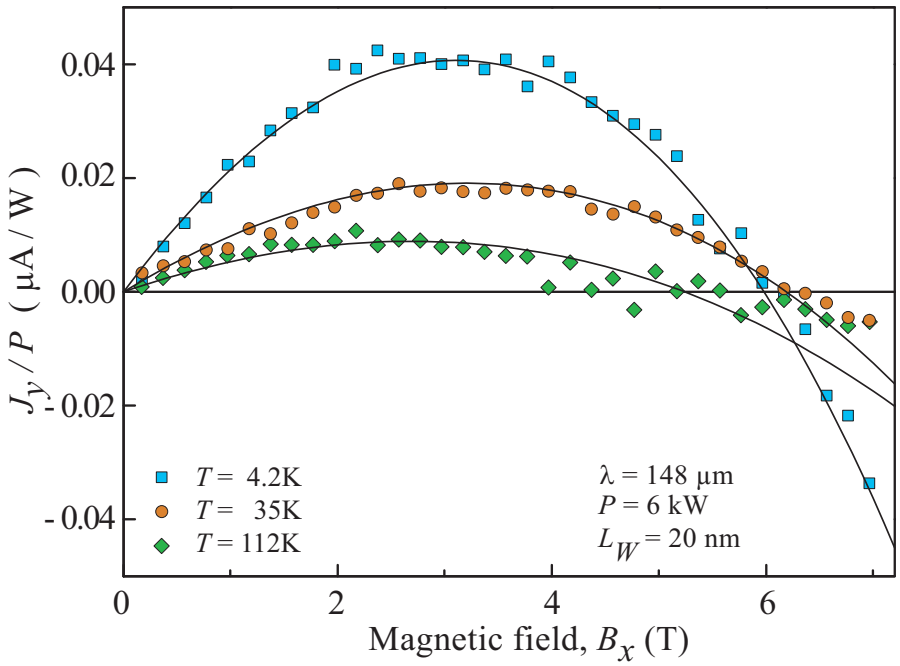

Figure 20: Transverse photocurrent J_y normalized by the radiation power P as a function of the in-plane magnetic field B_x for linearly polarized radiation of $\lambda = 148$ μm from the pulsed laser system and different temperatures T. The lines are fitted after Eq. (50).

vanishes again and even changes its sign. If the temperature is heated up to 112 K, the zero crossing of the photocurrent remains unchanged at a position of about 6.2 T. The maximum magnitude of the signal, however, decreases for higher temperatures. A more detailed analysis of this behavior was done by keeping the magnetic field fixed at the maximum photocurrent position $B_x = +3$ T and varying the temperature. For the low as well as for the high power excitation, the amplitude of the current remains constant for $T < 8$ K, but rapidly decays for higher T following a dependence close to $J \propto 1/T$.

In addition to the dependence on the temperature, also the behavior of the current for different wavelengths was investigated at a constant temperature of 4.2 K. Fig. 21 depicts the magnetic field dependence of J_y/P for 148 and 280 μm. The data show that the amplitude of the signal increases for longer wavelengths. Furthermore, the maximum current and, in particular, the zero crossing shifts to higher fields.

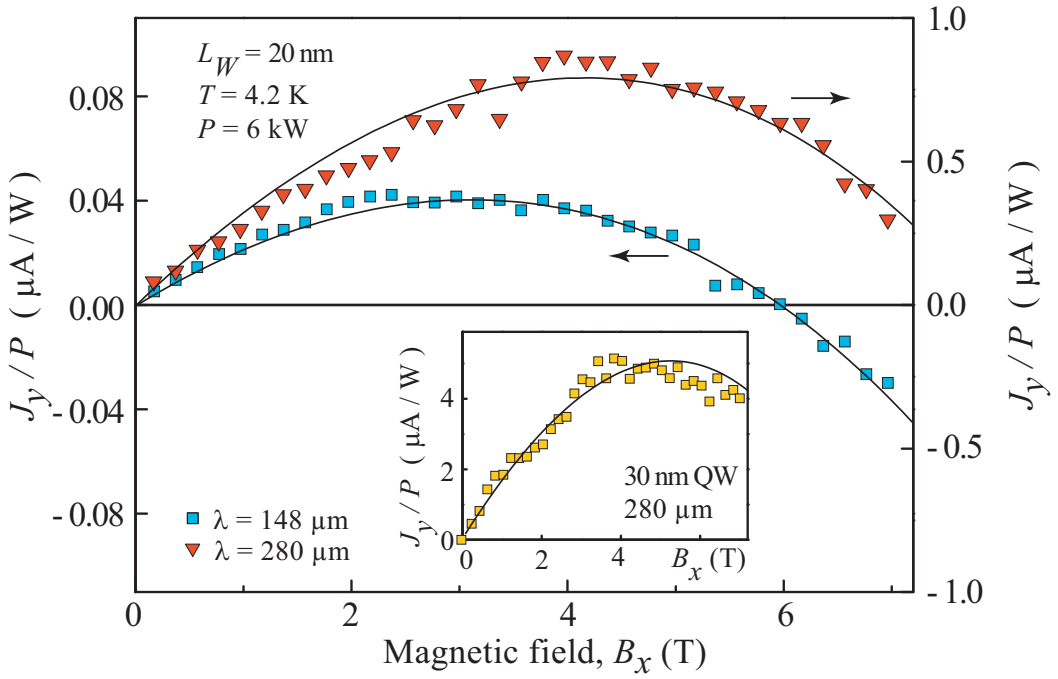

Figure 21: Transverse photocurrent J_y normalized by the radiation power P as a function of the in-plane magnetic field B_x for linearly polarized radiation from the pulsed laser system for fixed temperatures $T = 4.2$ K and different wavelengths $\lambda = 148$ and 280 μm. The inset shows the magnetic field dependence for the 30 nm wide QW structures. The lines are fitted after Eq. (50).

The inset of Fig. 21 shows the photocurrent's magnetic field dependence for the 30 nm wide QW structure. This structure exhibits a similar behavior for an increasing magnetic field. Here, the maximum occurs at larger magnetic fields and the magnitude of the signal is by a factor of 10 larger than the current of the 20 nm sample. Finally, one should note that a sweep of the magnetic field from -7 to +7 T and back results in no hysteresis effects.

5.1.2 Photoconductivity and electron gas heating

The experimental investigation of the photocurrents induced by linearly polarized radiation demonstrates that the signal is almost insensitive to the orientation of the radiation's electric field $\boldsymbol{E}$. Consequently, the dominant contribution to the current stems from a polarization-independent mechanism. Previous studies of the LMPGE in other materials demonstrated that such polarization-independent photocurrents are caused by the radiation-induced electron gas heating and a subsequent asymmetric scattering of carriers in $\boldsymbol{k}$-space during the relaxation process [22–24]. In order to characterize the electron gas heating due to the Drude-type absorption of the THz radiation, we use photoconductive measurements.

In general, photoconductivity (PC) describes the change of the electrical conductivity resulting from the irradiation of the structure. The more specific μ-photoconductivity, which only affects the change of the carrier mobility by illumination, may give an access to the phenomena of electron gas heating [75]. Fig. 22 (a) and (b) show the relative change of the conductivity $\Delta\sigma/\sigma_0$ for the 20 nm wide QW (type A) due to illumination with the *cw* and the high-power pulsed laser as a dependence of the radiation power incident on the sample. The structure is illuminated with different wavelengths from 118 to 280 μm at zero magnetic field and a temperature of $T = 4.2$ K. In contrast to the zero-bias measurements of section 5.1.1, here a voltage U_{bias} was applied to the sample. The change of the sample-resistance allows to determine the relative change of the conductivity $\Delta\sigma/\sigma_0 = (\sigma_i - \sigma_0)/\sigma_0$. Here σ_0 and σ_i are the conductivity of the dark sample and during the illumination, respectively.

In Fig. 22 (a), it can be seen that without radiation, no PC signal is observed. Increasing the power of the *cw* laser, a negative signal is detected, which raises for higher radiation power. The irradiation with a power of 1.25 mW yields a relative change of about -6×10^{-4}. Similar behavior is observed for the pulsed operation for two different wavelengths (see Fig. 22 (b)). Like for the *cw* system, a negative photoconductive signal is found for all wavelengths and radiation powers. Here, an increase of the radiation power up to several kilowatts results in a conductivity change up to about -5×10^{-2}, being two orders

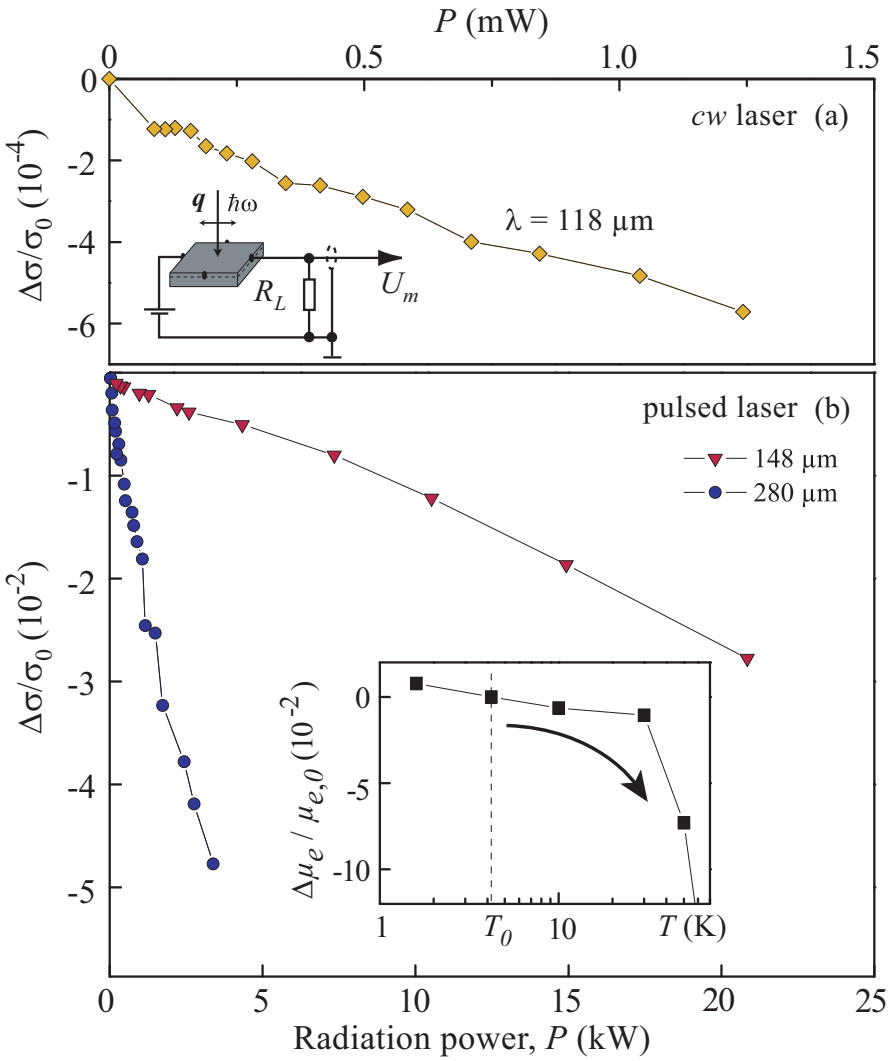

Figure 22: Relative change of the conductivity $\Delta\sigma/\sigma_0 = (\sigma_i - \sigma_0)/\sigma_0$ in the QW structures of 20 nm width measured versus the radiation power P at $T = 4.2$ K and $B = 0$. The ratio of the conductivity under illumination σ_i and the dark conductivity σ_0 is determined from the photoconductive signals measured in the circuit sketched in the inset of the upper plate. (a) Photoconductive signal measured applying *cw* radiation with wavelengths $\lambda = 118$ μm. (b) $\Delta\sigma/\sigma_0$ measured applying pulsed laser radiation with $\lambda = 148$ and 280 μm. The inset shows the temperature dependence of the relative change of the mobility $\Delta\mu_e/\mu_{e,0}$, where $\mu_{e,0}$ is the mobility at $T_0 = 4.2$ K.

in magnitude larger than for the *cw* laser. Keeping the radiation power P fixed, illumination with longer wavelengths leads to larger negative signals.

In order to understand the photoconductivity data presented above, one has to consider that all samples used in the experiments are n-doped, and therefore provide only one type of carriers ($p_0 \ll n_0$) at low temperatures. As the photon energies are much smaller than the energy gap (and consequently: $n_0 = const., \Delta n_0 = \Delta p_0 = 0$), the change of the conductivity $\Delta\sigma$ with respect to the conductivity without illumination $\sigma_0 = e(n_0\mu_e + p_0\mu_h)$ [50] can be written as:

$$\Delta\sigma = e(n_0\, \Delta\mu_e). \tag{35}$$

Here n_0, p_0, μ_e and μ_h are the carrier densities and mobilities for electrons and holes at dark conditions, respectively. It can be seen from Eq. (35) that for a constant carrier density the PC varies with the mobility [76]. In this case, the PC is restricted to the heating or cooling of the equilibrium electrons. Hence, it is useful to introduce the concept of the electron temperature T_e. The relative change of the conductivity due to the variation of the mobility can be expressed by the change of T_e [77]:

$$\frac{\Delta\sigma}{\sigma_0} = \frac{1}{\mu_e}\left.\frac{\partial\mu_e}{\partial T_e}\right|_{T_e=T_0} \Delta T_e, \tag{36}$$

where T_0 is the lattice Temperature and $\Delta T_e = T_e - T_0$. It is clearly seen that the sign of the relative photoconductive signal is determined by the derivative $\partial\mu_e/\partial T_e$ and the temperature difference ΔT_e. In order to obtain information about T_e, the temperature dependence of the electron mobility μ_e and the carrier density n_0 were determined from 1.7 K up to room temperature (see Fig. 23). These data were obtained applying low-field Hall measurements. While the carrier density is constant in a wide temperature range up to about 120 K, the mobility exhibits a sharp decrease at about 30 K, reflecting the predominant scattering by an increasing number of acoustic phonons for higher temperatures [50, 77]. From these data, we can calculate the relative change of the mobility $\Delta\mu_e/\mu_{e,0}$ with respect to the mobility $\mu_{e,0}$ at constant lattice temperature $T_0 = 4.2$ K. This is depicted in the inset in Fig. 22 (b).

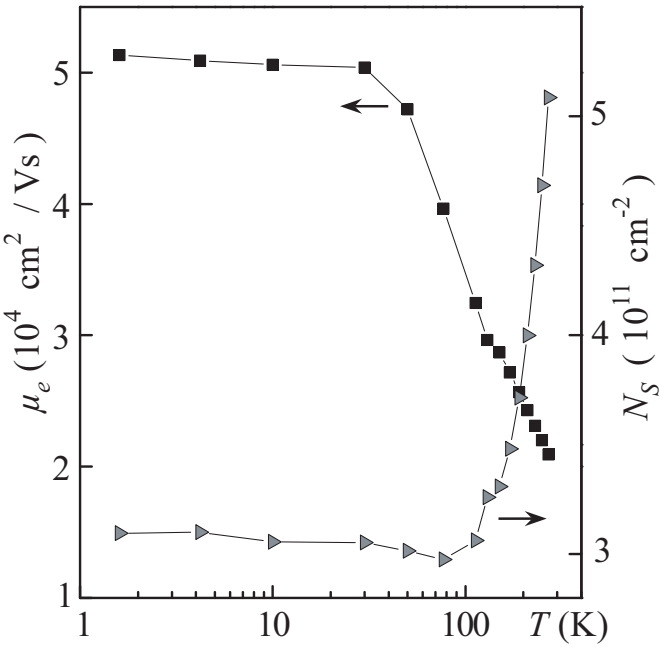

Figure 23: Temperature dependence of the electron mobility μ_e and carrier density N_s obtained by low-field Hall measurements in the 20 nm wide QW samples.

The comparison of the relative photoconductivity $\Delta\sigma/\sigma_0$ with the relative change of the mobility $\Delta\mu_e/\mu_{e,0}$ enables a rough estimation of the change in the electron temperature. An important observation is that the negative sign of $\Delta\sigma/\sigma_0$ reflects the decrease in μ_e, which again results from an increase of T_e. Furthermore, this method reveals that the *cw* low power laser radiation causes a negligible small heating of the electron system. In $\Delta\mu_e/\mu_{e,0}$, the relative change of about -6×10^{-4} results in only a tiny increase of the temperature. In contrast to the low power excitation, the illumination with radiation in the kW range yields a remarkable enhancement of the electron temperature (relative decrease of several 10^{-2}) from 4.2 up to several tens of Kelvin. In addition, the comparison of the PC data for different wavelengths demonstrates an essential stronger electron gas heating for longer wavelengths. This behavior reflects the typical frequency dependence of the Drude-type absorption, which increases with λ [51].

To summarize, the data presented above demonstrate that the absorption of high-power THz radiation drives the electron gas out of equilibrium and heats the electron subsystem [51, 78]. Due to the absorption, the internal energy of the system is raised and redistributed between the electron subsystem and the lattice. The excitation of the electron gas together with electron-electron scattering leads to a temperature of the electron system which differs from the temperature of the lattice. Regarding the radiation powers, the comparison of the *cw* and pulsed data reveals that an increase of the radiation power by about six orders of magnitude results in a change of the relative photoconductivity $|\Delta\sigma/\sigma_0|$ by about two orders of magnitude. This nonlinear power dependence can be explained by nonlinear energy losses in InSb QWs at low temperatures [51]. Consequently, this dependence causes a nonlinear dependence of the electron temperature T_e on the absorbed energy.

One should notice that the heating of the lattice in such measurements is negligible small and does not contribute to the signal. However, an accurate quantitative determination of the electron temperature is not possible, because for the mobility μ_e the increased lattice temperature results in a rising number of phonons. Nevertheless, qualitatively the PC signal varies in a similar way as the temperature of the sample was varied [76] and hence, the negative μ-photoconductivity proves the heating of the electron gas by the excitation with the low as well as the high power THz radiation. The asymmetric relaxation of the heated electron system in the presence of the external magnetic field leads to the photocurrents of the LMPGE presented above. These currents will be discussed in more detail in the following section.

5.1.3 Discussion

All our observations in the low magnetic field range exhibit the recognized behavior of the LMPGE. In particular, the linear coupling of the photocurrent $\boldsymbol{j}$ and the magnetic field $\boldsymbol{B}$ is a main feature of this effect and is substantially based on the gyrotropic symmetry of the InSb quantum well structures [23]. The sign reversion of the photocurrents by switching the magnetic field's direction, the anisotropy of the signal (j_x, j_y) in the plane of the 2DEG with respect to the applied field, as well as the dependence of the current on the orientation of the polarization was observed in all samples. These findings are in accordance with the observations in other zinc blende nanostructures of identical symmetry like, e.g. GaAs or InAs QWs. Compared to the photocurrents in these other materials, the currents in the InSb QWs are much stronger and at least two orders of magnitude larger. In particular, the magnetic field behavior of the LMPGE in all other materials featured solely a linear dependence on $\boldsymbol{B}$ [22,23]. Thus, the most striking feature of the LMPGE in InSb is the strong nonlinearity, which results even in a change of sign for sufficient large magnetic fields. In order to explain the strong nonlinear behavior of the photocurrent, the experimental results have to be analyzed taking into account the strong magnetic properties of InSb.

First, the polarization dependence of the current will be put in the phenomenological context. For the experimental geometry used here, the phenomenological equations (17) and (18) from chapter 2 reduce for low magnetic fields along the x-axis and purely linear polarization to:

$$j_x = S_3 B_x \left(e_x e_y^* + e_y e_x^*\right) I, \tag{37}$$

$$j_y = S_1' B_x I - S_2' B_x \left(|e_x|^2 - |e_y|^2\right) I. \tag{38}$$

The Stokes parameters, which were introduced in chapter 3.3, allow to rewrite Eq. (37) and the second term of Eq. (38) and express them by $\left(e_x e_y^* + e_y e_x^*\right) = \sin(2\alpha)$ and $(|e_x|^2 - |e_y|^2) = \cos(2\alpha)$. This polarization dependence is in full agreement with the experimental observations and reflects the phenomenology of the LMPGE based on the symmetry of the InSb quantum well, which belongs to the $C_{2\mathrm{v}}$ symmetry point group.

The prefactors S_1',S_2' and S_3 in Eq. (37) and (38) represent the strength of the single contributions. As the first term S_1' is in all experiments much larger than the polarization dependent terms, the experimental detected photocurrent stems from a mechanism independent of the initial orientation of the light's polarization.

Accordingly, the current formation can be explained by the heating of carriers and a subsequent asymmetric relaxation. The increase of the electron temperature is proved by μ-photoconductivity measurements. The negative photoconductive signal compared to the temperature dependence of the electron mobility reveals the heating of the electron gas up to several tens of Kelvin for the highest radiation powers. As shown in chapter 2, the subsequent relaxation of the heated electrons is, as a consequence of the spin-orbit coupling in gyrotropic media, spin-dependent and results in a pure spin current $\boldsymbol{J}_s = 1/2(\boldsymbol{i}_{+1/2} - \boldsymbol{i}_{-1/2})$. Without an applied magnetic field, the spin flows are of equal strength, and no current is detected. For the spin-polarization by an external magnetic field, the imbalance in the spin current leads to an electrical current:

$$\boldsymbol{j}_{\text{spin}} = -4es\boldsymbol{J}_s \qquad \text{with} \qquad s = \frac{1}{2}\frac{N_{+1/2} - N_{-1/2}}{N_{+1/2} + N_{-1/2}}. \tag{39}$$

Here $N_{\pm 1/2}$ are the carrier densities of the single spin-subbands. One should mention that for this theoretical consideration, it is convenient to use the current density $\boldsymbol{j}$ instead of the electric current $\boldsymbol{J}$. However, the electric current, which is detected in the experiments, is proportional to the current density used in the theory.

In the low magnetic field range, the Fermi energies E_F of our structures are much larger than the energy of the Zeeman spin-splitting Δ. In this case, the average spin $\boldsymbol{s}$ of the free electron gas can be expressed by:

$$\boldsymbol{s} = -\frac{\Delta}{4\bar{E}}\frac{\boldsymbol{B}}{B}, \tag{40}$$

where $\Delta = g^*\mu_B B$ is the energy of the Zeeman spin-splitting and $\bar{E}$ the characteristic electron energy, which is equal to the Fermi energy E_F for a degenerate, or equal to the thermal energy $k_B T$ for a non-degenerate electron gas. Herein,

k_B is the Boltzmann constant. The signals observed in the experiments follow in the low field range Eq. (40) ($J_y \propto s$), and therefore are linear in the magnetic field B_x. Furthermore, Eq. (40) is also in agreement with the temperature dependence of the photoresponse. The constant currents for temperatures $T < 8$ K reflect the constant Fermi energy E_F in a degenerate electron gas. For higher T, J_y decreases due to $s \propto 1/(k_B T)$. Contrary to the low field range, a nonlinear behavior of the current's magnetic field dependence for high fields is only possible for the case $|\Delta| > 2E_F$, where one spin-subband is completely depopulated. This would imply that the electron gas is fully spin-polarized ($s = \pm 1/2$) and hence, J_y saturates.

In order to explain the nonlinear behavior of the spin-dependent LMPGE in the whole field range, one should take into account that in thermal equilibrium the carrier densities $N_{\pm 1/2}$ are given by:

$$N_{\pm 1/2} \propto \sum_{\boldsymbol{k}} \left[\exp\left(\frac{\varepsilon_{\boldsymbol{k}} \pm \Delta/2 - \mu}{k_B T_e} \right) + 1 \right]^{-1}, \tag{41}$$

where $\epsilon_{\boldsymbol{k}} = \hbar^2 k^2/(2m^*)$ is the kinetic energy, m^* the effective mass, μ the chemical potential. Here, the effects of nonparabolicity of the conduction band were ignored due to the fact that the Boltzmann redistribution from the Zeeman spin splitting is much larger compared to these effects. A straightforward summation over the wave vector $\boldsymbol{k}$ results in:

$$s = \frac{1}{2} \frac{\ln\left\{ \left[1 + \exp\left(\frac{\mu - \Delta/2}{k_B T_e} \right) \right] / \left[1 + \exp\left(\frac{\mu + \Delta/2}{k_B T_e} \right) \right] \right\}}{\ln\left\{ \left[1 + \exp\left(\frac{\mu - \Delta/2}{k_B T_e} \right) \right] \times \left[1 + \exp\left(\frac{\mu + \Delta/2}{k_B T_e} \right) \right] \right\}}, \tag{42}$$

which describes an expression for the average spin of a two-dimensional electron gas in an external magnetic field for a fixed chemical potential μ. Since the total carrier density $N_S = N_{+1/2} + N_{-1/2}$ of the system is fixed during the experiment, we can introduce the chemical potential as follows:

$$\mu = k_B T_e \ln\left[\sqrt{\exp\left(\frac{2\pi N_s \hbar^2}{m^* k_B T_e} \right) + \cosh^2\left(\frac{\Delta}{2 k_B T_e} \right) - 1} - \cosh\left(\frac{\Delta}{2 k_B T_e} \right) \right]. \tag{43}$$

The average spin s from Eq. (42) saturates for sufficient large magnetic fields. Reaching an average spin close to $|s| = 1/2$, $s(B)$ becomes nonlinear and deviates from the linear dependence on B from Eq. (40). However, considering the samples used in the experiments, the deviation from a linear dependence occurs in spite of the large effective g^*-factor in InSb at larger fields than that used in the experiments, and therefore the observed nonlinear behavior of the photocurrent can not be caused by saturation effects.

Therefore, we suggest that other effects resulting in a nonlinear magnetic field dependence of the electron spin are responsible for the observed reversal of the electric current with the field increase. As a possible origin of this effect, we consider the *exchange interaction* between spin-polarized electrons, which causes a strong nonlinearity of the Zeeman spin splitting. This effect has been observed especially in InSb-based heterostructures by different experimental methods, like the coincidence method at tilted magnetic fields, polarization transition and the temperature-dependent resistivity [79, 80]. It has also been in the focus of several experimental and theoretical studies of structures based on other materials like GaAs or InAs [81–86]. At finite external magnetic field, the partial polarization of the electron gas yields, due to the interaction between the carriers, an enhancement of the spin susceptibility. Several other groups have shown that the enhancement is proportional to the average spin of the system and can be introduced in the effective g^*-factor by an additional term, which is linear in s [79, 80]:

$$g^* = g_0 + 2|s|g^{**}\,, \quad \Delta = (g_0 + 2|s|g^{**})\mu_B B, \tag{44}$$

Here g_0 is the effective Landé factor at zero magnetic field and g^{**} represents the strength of the exchange interaction. The modified Eq. (44) for the Zeeman spin splitting has to be introduced in Eq. (42) and (43). Afterwards both equations are solved by self-consistent calculations and the average spin s is plotted in Fig. 24 (a) for different interaction parameters g^{**} and in (b) for different electron temperatures T_e. For the calculations, we used an effective mass of $m^* = 0.02 \cdot m_0$. This value was obtained by the cyclotron resonance experiments presented in the following chapter and is in accordance with results from other groups [19, 42, 87]. The g^*-factor at zero field was used as -25,

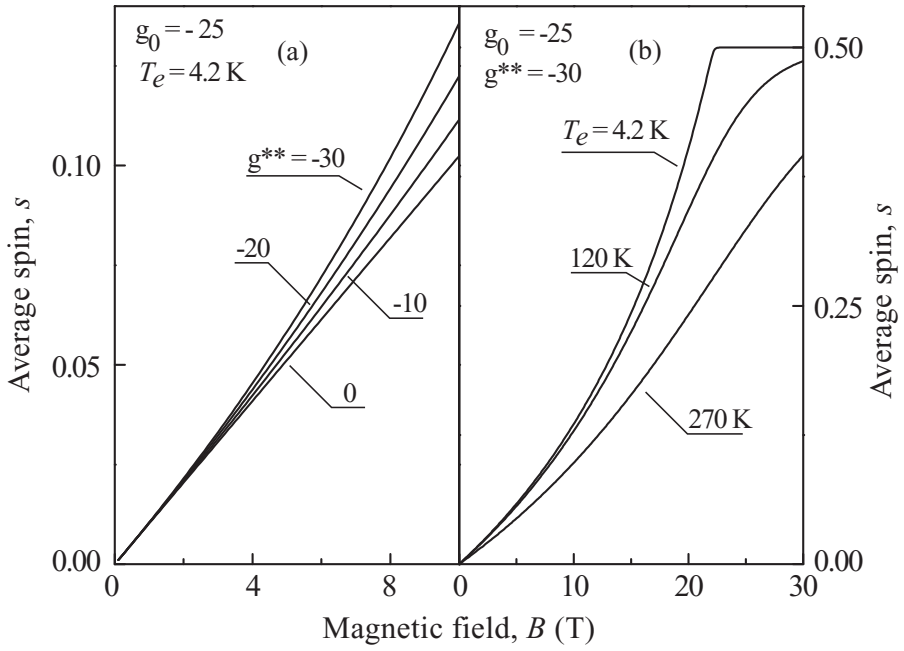

Figure 24: Average spin obtained by self-consistent calculations of Eq. (42) and (44) as a function of the magnetic field. For this calculations, a Landé factor g_0 = -25 at zero field and an effective mass of m^* = $0.02 \cdot m_0$ were used. Average spin calculated for (a) fixed temperature but for various values of the exchange interaction given by the parameter g^{**} indicated by numbers next to the curves; (b) fixed exchange interaction parameter g^{**} = -30 but various electron temperatures T_e.

which was measured by other groups for similar InSb QW structures [79]. In Fig. 24 (a) the effect of the interaction is clearly seen. A comparison of the magnetic field dependences with and without exchange interaction shows that $s(B)$ changes for an increasing parameter g^{**} from a linear function to a superlinear dependence on B. For a fixed magnetic field, the exchange interaction leads to a stronger spin-polarization of the system than without interaction. Figure 24 (b) illustrates the behavior for various electron temperatures. A change of T_e from 4.2 up to about 130 K results in almost no change in $s(B)$ in the field range up to 10 T. For higher magnetic fields, a saturation of the electron's average spin occurs at about 22 T. This calculations show that in our experimental setups, where fields up to 7 T and temperatures up to 120 K

were used, $s(B)$ remains nearly unaffected by the temperature. Only for temperatures above 120 K, the electron temperature T_e plays an important role for the field dependence of the average spin and, thereby, for the Zeeman splitting.

While spin-mediated relaxation can produce a nonlinear signal, it can not cause the observed sign reversal of the photocurrent. Hence, another spin-independent mechanism of the LMPGE has to be taken into account, which was theoretical predicted by Tarasenko and Fal'ko [25, 88, 89]. This mechanism has already been observed in GaAs quantum well structures [90] and may provide an additional contribution to the total photocurrent. Its generation is based on the asymmetric relaxation of the heated electrons due to the Lorentz force acting on the moving carriers, and is therefore called the orbital mechanism as opposed to the previous presented spin-dependent effect. The origin of this effect is again the structure and/or bulk inversion asymmetry of the sample. In contrast to the effect of the LMPGE based on the spin, the electron scattering rate with an asymmetric term from the orbital mechanism can be expressed in the following way:

$$\boldsymbol{W_{kk'}} = W_0 + w_{\mathrm{SIA}}[\boldsymbol{B} \times (\boldsymbol{k} + \boldsymbol{k'})]_z. \tag{45}$$

Here W_0 is the field-independent term and w_{SIA} is a measure of the structure inversion asymmetry. Eq. (45) can be written in a similar way for the case of bulk inversion asymmetry. The difference to Eq. (20) in chapter 2 is that the scattering rate is linear in $\boldsymbol{B}$ instead of the spin $\boldsymbol{\sigma}$. Due to the magnetic-field-dependent scattering, transitions to positive and negative k'_y states occur with different probabilities. Therefore, hot electrons with opposite k_y have different relaxation rates in the two spin subbands, and hence an electric current is generated.

The microscopic mechanism of this process is illustrated in Fig. 25. The picture shows a side view of the quantum well for three different points in time. The arrows on the top demonstrate the oscillating electric field $\boldsymbol{E}(\omega, t)$ of the terahertz radiation. On the left-hand side, the wave function of an electron is slightly shifted to the upper barrier (blue) due to the asymmetry of the QW, which stems from the asymmetric single-side δ-doping (indicated by the dashed line in the barrier). The magnetic field is applied along the x-axis. For the

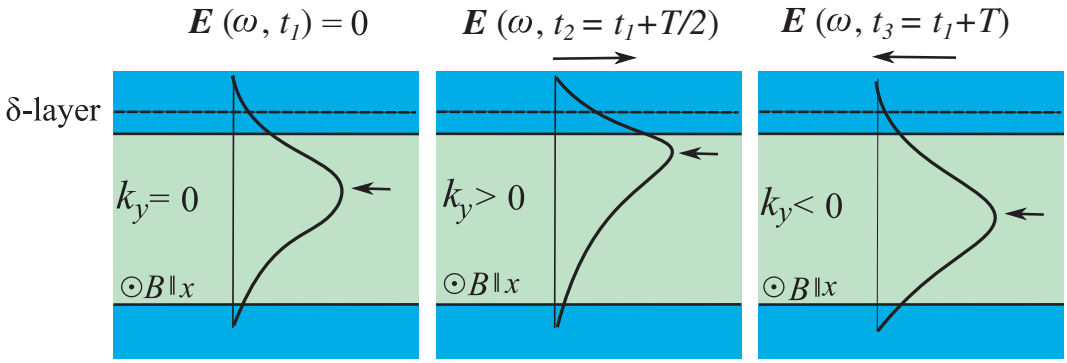

Figure 25: Side view of the QW with barriers (blue) and δ-doping layer (dashed line) for three different points in time (left, center, right). A magnetic field is applied long x and the electron wave function maximum is indicated by arrows. The electric field vector $\boldsymbol{E}(\omega,\, t)$ of the radiation is zero for t_1 and points in opposite y-directions for t_2 and t_3. k_y is the wave vector of the electron resulting from $\boldsymbol{E}$.

first point in time, the electric field is zero $\boldsymbol{E}(\omega, t_1) = 0$ and therefore $k_y = 0$. For a non-zero field $\boldsymbol{E}(\omega, t_2 = t_1 + T/2)$ half a period later in time, the electron exhibits a momentum $k_y > 0$ due to the electric force, and consequently the Lorentz force $\boldsymbol{F}_L = e(\boldsymbol{v} \times \boldsymbol{B})$ acts on the moving electron. The force leads to a shift of the wave function to the upper barrier of the QW. One period in time later, the electric field $\boldsymbol{E}(\omega, t_3 = t_1 + T)$ has an opposite sign and therefore the sign of the Lorentz force $\boldsymbol{F}_L$ also reverses. Now, the wave function is shifted closer to the lower barrier. If we now consider the relaxation of electrons by scattering on impurities or phonons, the difference in the overlap of the wave function with, e.g. the δ-layer, causes an asymmetry in the scattering rate for t_2 and t_3. This asymmetry is expressed in Eq. (45). As a result, the imbalance of the electrons with velocity in positive y- and negative y-direction results in an electric current.

The electric current originating from the orbital effect can be written as:

$$\boldsymbol{j}_{\mathrm{orb}} = -2e \sum_{\boldsymbol{k}} \boldsymbol{v}_{\boldsymbol{k}} f_{\boldsymbol{k}}, \tag{46}$$

where $\boldsymbol{v_k} = \hbar\boldsymbol{k}/m^*$ is the electron velocity and $f_{\boldsymbol{k}}$ the electron distribution function. This electron distribution function can be derived from the Boltzmann equation:

$$G_{\boldsymbol{k}} - \sum_{\boldsymbol{k'}} [\boldsymbol{W_{kk'}} f_{\boldsymbol{k'}}(1 - f_{\boldsymbol{k}}) - W_{\boldsymbol{k'k}} f_{\boldsymbol{k}}(1 - f_{\boldsymbol{k'}})] = 0, \tag{47}$$

where the generation term $G_{\boldsymbol{k}}$ describes the electron gas heating by the linear polarized terahertz radiation. From Eq. (45), it can be seen that the scattering rate contains an asymmetrical part proportional to $w_{\mathrm{SIA}}B$. Therefore, also the distribution function $f_{\boldsymbol{k}}$ contains an asymmetrical part and, hence, the orbital photocurrent $\boldsymbol{j}_{\mathrm{orb}}$ is linearly coupled with the external magnetic field and proportional to the degree of SIA (and/or BIA):

$$\boldsymbol{j}_{\mathrm{orb}} \propto w_{\mathrm{SIA}} \boldsymbol{B} \tag{48}$$

This linear behavior is restricted to the width of the quantum well. For large enough magnetic field strengths, Eq. (48) is not valid any more. However, a rough estimation for the quantum wells used in the experiments gives a maximum magnetic field strength until which the orbital photocurrent $\boldsymbol{j}_{\mathrm{orb}}$ remains linear in $\boldsymbol{B}$ [25, 88]:

$$B \approx \frac{\pi^2 \hbar c}{e L_W^2}. \tag{49}$$

For well widths of $L_w \approx 20$ nm and 30 nm, this is much larger than the fields used in our setup.

Both mechanisms, the spin-dependent and the orbital, contribute to the total photocurrents measured in the experiments. The measured currents are the sum of the spin and non-spin mechanism:

$$j_y = j_{\mathrm{spin}} + j_{\mathrm{orb}}. \tag{50}$$

The total photocurrent contains the magnetic field dependences from Eq. (39) together with Eq. (42) and (48), and can therefore be fitted to the experimental data by using the functions $j_{\mathrm{spin}} = a \cdot s(B)$ and $j_{\mathrm{orb}} = b \cdot B$, where

a and b are fitting parameters. Combining spin and non-spin mechanism and assuming they have opposite signs, it is possible to reproduce the experimental data, and in particular the reversal of the photocurrent direction. Thereby, we used a Landé factor of g_0 = -25 and a exchange interaction parameter of g^{**} = -30 (obtained in InSb QWs similar to our structures by magnetotransport measurements [79]), the estimated electron temperature T_e from the photoconductivity measurements and scaled the strengths of both mechanisms via a and b. By this, we can well describe the data for the low radiation power measurements in Fig. 19, as well as the high-power photocurrents in Fig. 20 and 21. The different dependence of both mechanisms on the magnetic field strength reveals that in the low field, linear range the orbital mechanism is dominant. The nonlinear increase of the average spin with B due to the exchange interaction (see Fig. 24) causes an enhancement of the spin-related LMPGE, which becomes the major origin in the high-field range.

Both contributions follow the identical phenomenological equations (17) and (18) in chapter 2 [25, 88, 90]. It is therefore not possible to separate them by means of the dependence on the radiation's polarization or the direction of the magnetic field relative to the crystallographic axis. The consideration above shows, however, that the different behavior of the photocurrent upon variation of the magnetic field strength allows to distinguish between these two mechanisms. The determination of the parameters a and b also shows that the spin and orbital effect yield photocurrents of comparable strength. The strong spin-orbit coupling of InSb and its huge magnetic properties, in particular the large g^*-factor, suggest the assumption that the spin-related mechanism should be dominant. However, the orbital mechanism is inverse proportional to the effective mass of the carriers [25, 88]. In InSb-based quantum well structures with an effective mass much smaller than in other III-V semiconductor materials, the orbital contribution is therefore also strongly enhanced.

5.2 Circular MPGE

While in the first part of this chapter, the observation of magnetic field induced photocurrents due to the excitation with linearly polarized radiation was presented, in this section it will be demonstrated that illumination of InSb QWs with circularly polarized light yields an helicity-dependent photocurrent. The behavior of this current upon a variation of the magnetic field strength will be studied for different wavelengths. Similar to the LMPGE, the signals due to the CMPGE are finally discussed in terms of a spin-related and an orbital mechanism of this effect.

5.2.1 Experimental results

For the investigation of the CMPGE, the linear polarization of the THz radiation was transformed into circular polarized light by a $\lambda/4$ plate and the magnetic field is aligned along the x-axis. Like in the previous section, the current is detected both parallel (J_x) and perpendicular (J_y) to B_x. For a non-zero magnetic field B_x, we observed a current in both directions, which varies with the rotation of the angle φ. This angle defines the polarization state of the THz radiation, which is illustrated on the top of Fig. 26 for various φ. Similar to the variation of the linear polarization of the LMPGE, the dependence of the photocurrent on the angle φ can be described via the Stokes parameters introduced in chapter 3. The transverse photocurrent J_y traces the function $J_y = J_1 + (J_2/2) \cdot \cos(4\varphi)$ (not shown). In particularly for right- and left-handed circular polarization at $\varphi = 45°$ and $135°$, respectively, this transverse current vanishes and is only non-zero for linearly or elliptically polarized light. Like for the LMPGE, the current induced in this experiments consists of a polarization-independent contribution J_1 and a contribution which is sensitive to the degree of linear polarization. These two contributions are identical to the transverse currents observed in the LMPGE experiments.

The polarization dependence of the photocurrent J_x parallel to the external field B_x and normalized by the radiation power P is depicted in Fig. 26 for different polarization states and a fixed magnetic field B_x = -6 T. This longitudinal current at non-zero magnetic field can be well described by the following

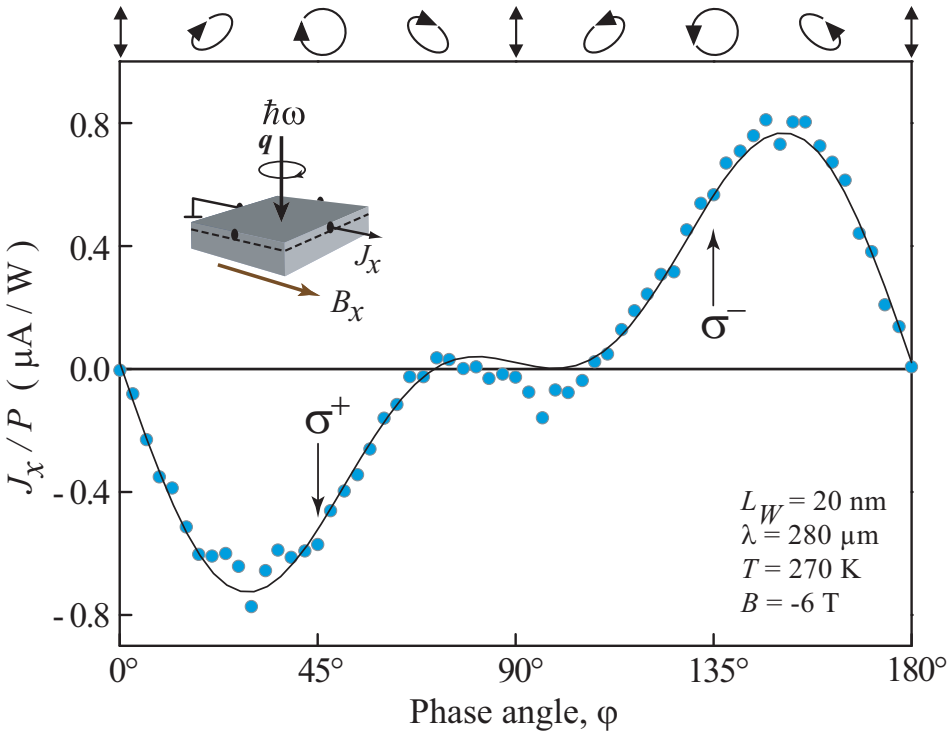

Figure 26: Helicity dependence of the photocurrent J_x normalized by the radiation power P for B_x = -6 T and λ = 280 μm with subtracted offset ξ. The inset shows the experimental setup. The ellipse on the top illustrate the polarization states for various φ.

equation: $J_x = (J_3/2) \cdot \sin(4\varphi) + J_C \cdot \sin(2\varphi) + \xi$. The total current consists of different contributions. The first term proportional to J_3 stems again from the current's dependence on the orientation of the linear polarization and is identical to the J_3-term of the LMPGE. Similar to the J_2-term of the transverse current, this J_3-term vanishes for circularly polarized radiation. However, in the parallel current J_x an additional term J_C occurs. This contribution is proportional to the light's helicity $P_{\text{circ}} = \sin(2\varphi)$. By changing the helicity of the radiation from left- to right-handed circular polarization, P_{circ} switches from -1 to +1 and the photocurrent changes its sign. In Fig. 26, this sign reversion for opposite helicity is indicated by arrows at 45° and 135°. The last term of the photocurrent's function, ξ, represents a polarization-independent offset. Since ξ is in all measurements much smaller than the other two contributions J_3 and J_C, we subtracted it from the data shown in Fig. 26.

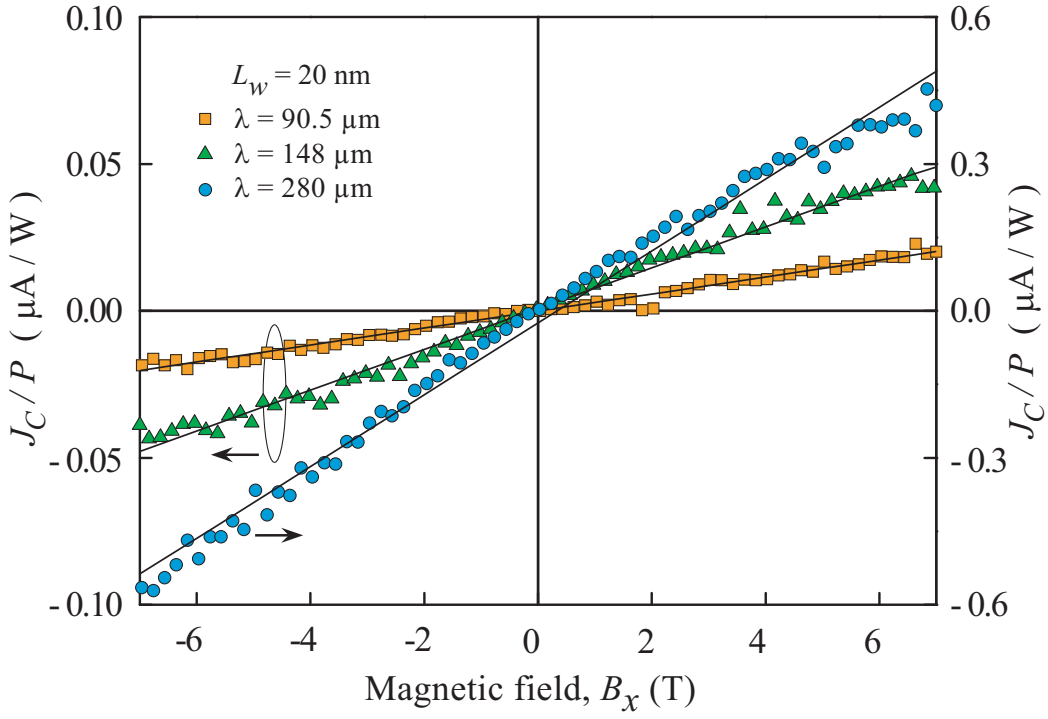

Figure 27: Circular photocurrent J_C/P as a function of the applied magnetic field B_x for wavelengths λ = 90.5, 148 and 280 μm at T = 270 K.

From the functions for the transverse and parallel photoresponses, it is obvious that only the term J_C of J_x is sensitive to the helicity of the light. Hence, we focus only on this contribution and eliminate all other terms by:

$$J_C = \left[J_x(\sigma^+) - J_x(\sigma^-)\right]/2. \tag{51}$$

The photocurrent term J_C normalized by the radiation power P is depicted in Fig. 27 as a function of the external magnetic field B_x for the 20 nm QW structures and different wavelengths. The helicity sensitive signal increases with rising magnetic field strength and changes its sign by reversing the direction of the external field. In particular, the current J_C is linear in B_x in the whole magnetic field range from -7 up to +7 T. Furthermore, for a fixed magnetic field, the magnitude of the current increases for longer wavelengths by more than one order of magnitude. The same purely linear magnetic field de-

pendence of an helicity-dependent photocurrent is also obtained for the 30 nm QW samples.

5.2.2 Discussion

In the analysis of the experimental data, two remarkable characteristics become evident. On the one hand, the current changes its sign for opposite magnetic field directions, and on the other hand, the photocurrent reverses by switching the light's helicity. These are typical fingerprints of the spin-galvanic effect [63] (in the following termed as the spin-dependent mechanism of the CMPGE). Considering the phenomenological equation (23) from chapter 2 and the C_{2v} point group symmetry of the zinc blende structure investigated here, this effect is only allowed for a component of the average spin in the plane of the 2DEG. This is achieved by initial spin-orientation along the z-axis and subsequent precession of the spin about an in-plane magnetic field. The resulting photocurrent is proportional to the in-plane spin-component and can therefore be written as [63]:

$$J_x^{\text{spin}} \propto -\frac{\omega_L \tau_{s\perp}}{1+(\omega_L \tau_s)^2} S_{0z}, \tag{52}$$

where $\tau_s = \sqrt{\tau_{s\parallel}\tau_{s\perp}}$ and $\tau_{s\parallel}$, $\tau_{s\perp}$ are the longitudinal and transverse electron spin relaxation times, $\omega_L = g^*\mu_B B_x/\hbar$ the Larmor frequency, and $S_{0z} = \tau_{s\parallel}\dot{S}_z$ is the steady-state electron spin-polarization in the absence of the magnetic field. The dependence of J_x^{spin} is a result of the rotating spin and represents the Hanle effect [91]. The in-plane component S_y and consequently the current rises with increasing magnetic field and reaches its maximum for $\omega_L\tau_s \approx 1$. By a further increase of the external magnetic field, and consequently larger $\omega_L\tau_s$, the current decreases and finally vanishes as it follows from the Hanle law. This dependence of the spin-dependent CMPGE has already been observed in wider gap materials like, e.g., GaAs low-dimensional structures and is determined by g^* and τ_s [63]. The spin-relaxation time of our InSb QWs has been obtained by other groups applying circularly polarized pump probe technique [68, 92]. These studies determined a value of $\tau_s \approx 0.1$ ps. Considering in addition a Landé factor of $g^* =$ -45, the maximum of the photocurrent is expected for

$B_x \approx 2.5$ T. However, Fig. 27 obviously shows a purely linear dependence on B_x, and in particular no maximum or any nonlinearity. Hence, the spin-dependent CMPGE does not contribute to the observed photocurrent behavior.

Similar to the orbital contribution to the LMPGE presented in section 5.1, a microscopic mechanism describing the orbital motion of the electrons also yields an helicity driven photocurrent [25, 88]. The irradiation of circularly polarized radiation causes the free electrons to perform cyclic motions. The in-plane magnetic field combined with SIA/BIA of the underlying structure forces the carriers to flow predominately along the direction of $\boldsymbol{B}$. This asymmetry in the scattering is again a result from the B-dependent corrections to the scattering probability given in Eq. (45). The underlying process is based on the Lorentz force acting on the moving electrons. One important aspect in the current formation of the orbital CMPGE is the retardation between the rotating electric field of the radiation and the electron velocity. Therefore, it reaches a maximum at $\omega\tau \approx 1$ (here, $\omega = 2\pi f$ is the radiation angular frequency and τ the scattering time), and vanishes for much lower or higher frequencies. Just as the spin-dependent mechanism, this orbital photocurrent is sensitive to the sign of the radiation's helicity as well as the direction of the magnetic field. In general, it can be described by the following equation:

$$J_\alpha^{\mathrm{orb}} = P_{\mathrm{circ}} |E_0|^2 \sum_\gamma R_{\alpha\gamma} B_\gamma. \tag{53}$$

Here, the second rank pseudotensor $\boldsymbol{R}$ has the same space symmetry properties as the pseudotensor $\boldsymbol{Q}$ from Eq. (23), which describes the spin-dependent CMPGE [90]. It follows again from Eq. (49) that for the QW widths of our structures, the orbital CMPGE is linear in $\boldsymbol{B}$ in the magnetic field range used in the experiments. Thus, the observed linear magnetic field behavior leads to the conclusion: the CMPGE in InSb-based QWs is dominated by the orbital mechanism. This follows from the fact that the magnetic field dependence of the CMPGE shows only a linear behavior in the field range up to ± 7 T, and in particular features no maximum current as it would be expected from a spin-dependent mechanism, which follows a Hanle curve. Similar to the orbital effect of the LMPGE, the orbital CMPGE is also inverse proportional to the electron's effective mass [88], and is therefore stronger in narrow gap materials.

As a result, the dominance of the orbital contribution can be attributed to the small band gap of InSb.

5.3 Summary

The linear and the circular MPGE in InSb-based QWs were demonstrated by illumination with THz radiation in the presence of an in-plane magnetic field. A comparison of the experimental results with data from other III-V materials reveals that the narrow energy gap, the strong magnetic properties and the strong spin-orbit coupling substantially enhance the MPGE. The magnetic field dependences of both effects feature a contradictory behavior: while the LMPGE is strongly nonlinear, the CMPGE is linear in the whole field range. Both dependences can be explained by the contribution of a spin and a orbital mechanism. The nonlinear behavior of the LMPGE is caused by the nonlinearity of the Zeeman spin splitting and supports recent conclusions on high polarization-dependent spin susceptibility of a two-dimensional electron gas in InSb-based QWs [79, 80]. For this effect, the spin and orbital mechanism have comparable strength. In contrast, the pure linear dependence of the CMPGE demonstrates that this effect is in InSb-based QW structures dominated by the orbital mechanism due to the small energy band gap and the associated small electron effective mass.

6 Photocurrents under cyclotron resonance conditions

In this chapter, THz induced photocurrents under cyclotron resonance conditions are presented. It is demonstrated that the illumination of InSb QW structures under oblique incidence of radiation onto the sample surface and the application of a magnetic field normal to the 2DEG leads to resonantly enhanced photovoltage signals. The voltage signals are studied parallel and perpendicular to the radiation beam. Furthermore, the radiation induced photovoltages are analyzed for various polarization states, wavelengths and temperatures. In addition, optical transmission experiments are performed and compared to the photovoltage signals. In the second part of this chapter, a theoretical model is developed based on the Boltzmann kinetic equation in the presence of a static normal magnetic field. The model takes into account the deflection of the photocurrent as a result of the Lorentz force and the enhanced radiation absorption at the cyclotron resonance position.

6.1 Experimental results

In order to investigate terahertz radiation induced currents under cyclotron resonance conditions, the magnetic field is applied along the growth direction and normal to the 2DEG. The photocurrents are detected via the voltage drop $U_{x,y}$ across the sample. Since the results of chapter 4 indicated a reduced symmetry of the 20 nm wide QWs (type A), we focus the investigations in this chapter to the 30 nm QW samples. The clear knowledge of the structure's symmetry simplifies the analysis of the resonant signals presented below.

As a first step, the 30 nm wide QW structure (type B) is irradiated under normal incidence of the laser beam. In this configuration, no signal is detected for any polarization in the whole magnetic field range from -7 up to +7 T (not shown). This observation is in accordance with the results presented in chapter 4 and 5.

As a further step, the THz beam is tilted by an angle θ' with respect to the sample normal and consequently hits the sample surface under oblique inci-

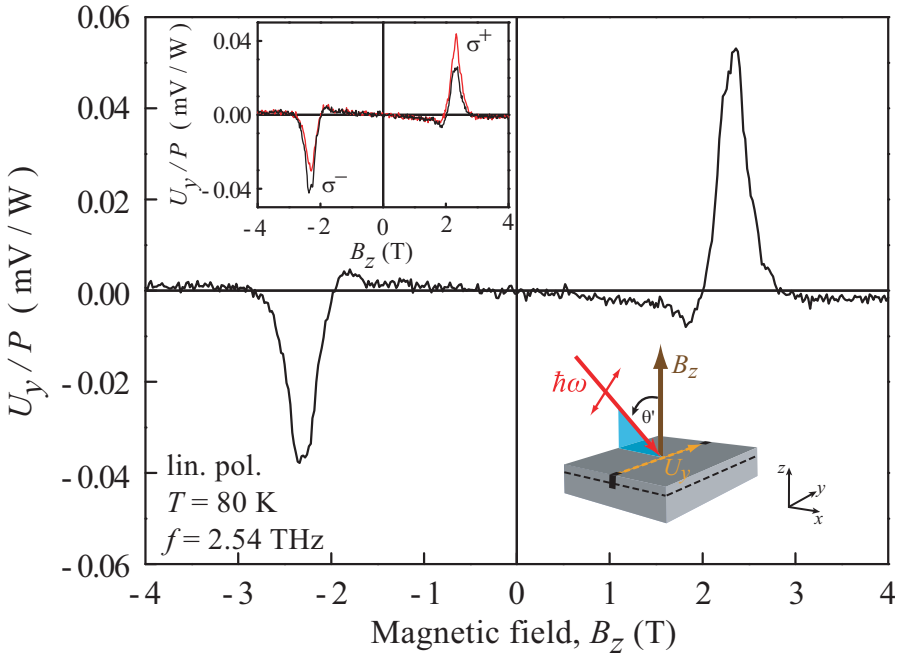

Figure 28: Transverse photovoltage signal U_y normalized on the radiation power P as a function of the magnetic field B_z normal to the 30 nm wide QW structure. The signal is induced by radiation with a frequency of 2.54 THz (118.8 μm) from the *cw* laser system at T = 80 K. The linear polarization is aligned in the plane of oblique incidence (p-polarization). The inset on the right side illustrates the geometrical setup. The left inset shows the dependence of U_y/P for left-handed (σ^-) and right-handed (σ^+) circular polarization.

dence. The radiation beam now lies in the xz-plane (see inset of Fig. 28 and 29). Also the linear polarization is oriented in this plane and the electric field vector $\boldsymbol{E}$ possesses a component in z-direction ($E_z \neq 0$). The configuration with the tilted radiation beam allows to define the measured signals U_x (parallel) and U_y (perpendicular) by their orientation relative to the plane of oblique incidence.

Figure 28 shows the normalized transverse signal U_y/P as a function of the magnetic field B_z. The sample was excited with a frequency of 2.54 THz (118.8 μm) from the *cw* laser system at T = 80 K. A sweep of the magnetic field up to +4 T yields a strong resonant photo signal at $B_c \approx +2.3$ T. The

resonance can be well fitted by a Lorentzian function. For higher fields up to +7 T, the signal almost vanishes again and no further resonances are detected. At the resonance position, the signal is strongly enhanced and the amplitudes at B_c and in the vicinity of zero magnetic field differ by more than two orders of magnitude. Characteristic for the transverse voltage signal is that a reversion of the B-field's direction yields a resonance in the photovoltage U_y at a corresponding negative field position but with opposite sign of U_y. Thus, the signal U_y can be described by an odd function of the magnetic field B_z.

A similar behavior is observed for circular polarization. Illumination with circularly polarized light, converted from linearly polarized light by $\lambda/4$-plates, demonstrates that the resonant signals are sensitive to the radiation's helicity. The magnetic field dependence for this polarization is illustrated in the left inset of Fig. 28. The photovoltage is again strongly enhanced at the resonance positions $\pm B_c$ for both helicities of light. However, for each polarization state, the signal U_y is increased or decreased for one specific field direction.

Figure 29 depicts the magnetic field dependence of the photo signal U_x parallel to the plane of oblique incidence. Similar to the transverse signal, also U_x is strongly enhanced and resonances in the signal occur. The resonances are again positioned at $B_c \approx \pm 2.3$ T, but now the sign of the resonant signal is negative for both polarities of B_z and therefore U_x describes an even function of the magnetic field. Finally, a comparison of the width of the parallel and the transverse Lorentzian-shaped signals reveals that both resonances are similarly wide broaden.

A remarkable observation concerns the orientation of the linear polarization. It turns out that both magnetic field dependences presented above are almost insensitive to the orientation of the radiation's electric field vector $\boldsymbol{E}$. Figure 28 and 29 show the signals for a non-zero component of $\boldsymbol{E}$ along z (p-polarization). A rotation of the polarization vector by a $\lambda/2$-plate in the xy-plane results in $E_z = 0$ (s-polarization), but only causes a small variation in the magnitude of the resonances. In particular, the resonant signals in U_y and U_x are present for any orientation of $\boldsymbol{E}$.

In order to analyze the influence of the absorption on the photovoltage signals, the transmission through the sample was investigated under variation

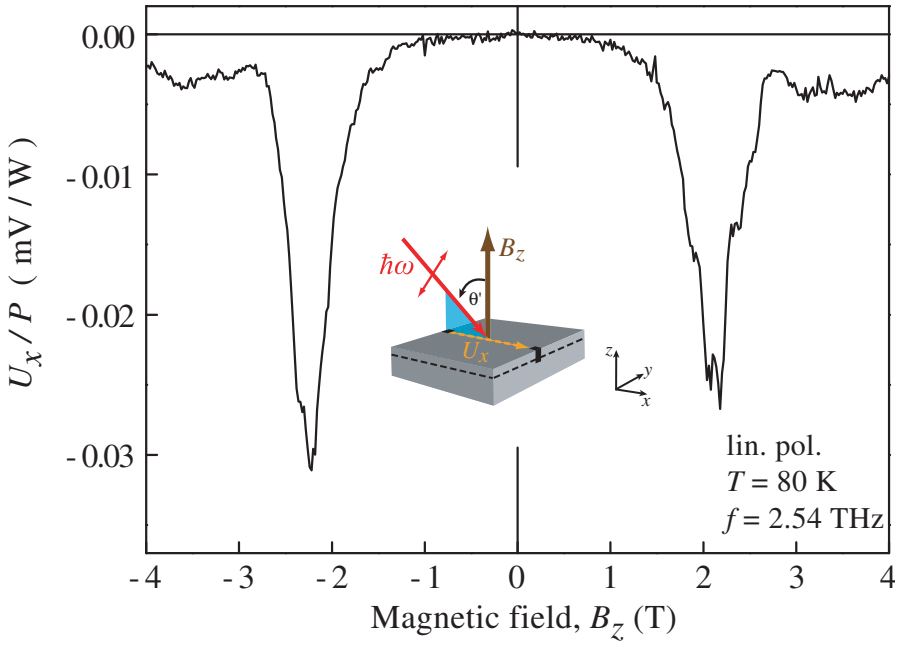

Figure 29: Parallel photovoltage signal U_x normalized on the radiation power P as a function of the magnetic field B_z for a frequency of 2.54 THZ (118.8 μm) at $T = 80$ K in the 30 nm QW structure (p-polarization). The inset in the center illustrates the geometrical setup.

of the applied magnetic field. The power of the THz radiation, which passes parallel to the growth direction through the structure, was measured by a Golay cell detector. The normalized transmission $T(B_z)/T(B_z{=}0)$ is depicted in Fig. 30 for various polarization states and 2.54 THz, the same frequency as in Fig. 28 and 29. All transmission measurements show clearly resolved resonances, whose position coincide with that of the photovoltage experiments. The transmission possess sharp dips down to 45 % of the initial signal at $B_c \approx \pm 2.3$ T, in particular the same position as for the photovoltage response. For circular polarization, the resonant signal is detected only for one polarity of B_z. This helicity dependence corresponds to that of the photovoltage. However, in contrast to the transmission, the photovoltage signal does not vanish completely for one specific helicity. Applying linearly polarized light, the decrease is half as large as for $\sigma^{\pm}$ and appears for both magnetic field directions $\pm B_c$. This behavior is due to the fact that linearly polarized light is the su-

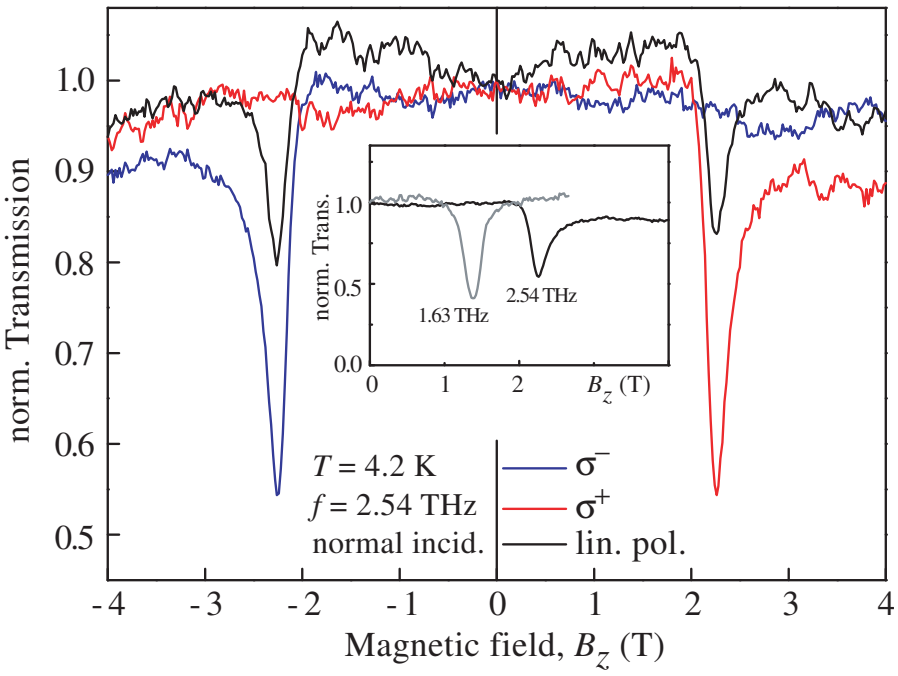

Figure 30: Transmission $T(B_z)$ normalized on the transmission at $B_z = 0$ in dependence on the applied magnetic field B_z. The transmission is detected for a frequency of 2.54 THz (118.8 μm) for different polarization states and at normal incidence of light in the 30 nm QW structure at $T = 4.2$ K. The inset compares the transmission for 1.63 and 2.54 THz.

perposition of σ^+ and σ^- photons [93]. The same observation is apparent in the photovoltage measurements, where the signals for $\pm B_c$ are almost equal in magnitude (see Fig. 28 and 29). The inset in Fig. 30 shows the transmission for different radiation frequencies. It can be seen that for 1.63 THz, the resonance shifts to a smaller magnetic field position $B_c \approx 1.4$ T. The transmission experiments were also carried out for oblique incidence of the beam under an angle of $\theta' \approx 20^\circ$ (not shown) similar to the setup of the photovoltage experiments. For this configuration, the resonances were detected at the same position B_c and show the same helicity-sensitive behavior as for normal incidence. Finally, one should note that in all transmission measurements, the resonances were only present at 4.2 K and rapidly vanished for higher temperatures. In partic-

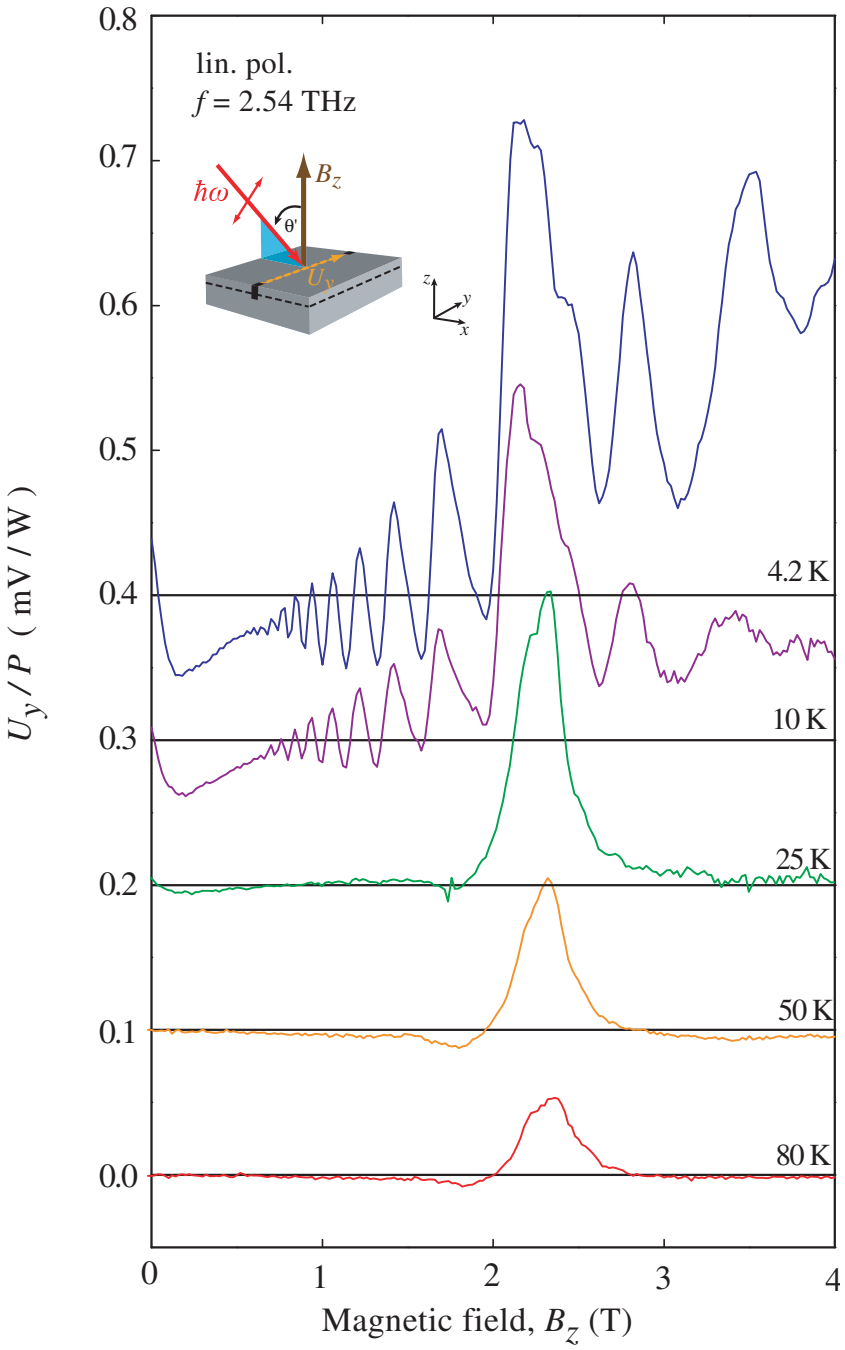

Figure 31: Magnetic field dependence of the transverse signal U_y/P for 2.54 THz and different temperatures. The data for each T is shifted by +0.1 mV/W.

ular, these signals are much more sensitive for elevated temperatures than the photovoltages.

Figure 28 and 29 showed the resonant photo response for a fixed temperature of $T = 80$ K. For higher temperatures, the amplitudes of the resonances decrease and vanish for $T > 100$ K. Figure 31 illustrates the behavior of the resonant signal for decreasing T down to liquid helium temperature. A resonant photovoltage was observed down to 25 K. Thereby, the maximum amplitude increases by about four times, while the resonant magnetic field position B_c remains unchanged. For even lower T, the signal U_y shows clearly pronounced oscillations, which start at about 0.7 T and are stronger for higher fields. The spacing between the maximum and minimum positions increases with B_z, meaning that the oscillation frequency decreases with B_z. Due to the predominating oscillating photovoltage, the resonant character of the signal is not clearly resolved anymore. The oscillations occur transversal as well as in the direction parallel to the plane of oblique incidence for linearly and circularly polarized light.

In order to analyze the oscillations in the photovoltage signal, the inverse magnetic field positions of the maximums $1/B_{max}$ were plotted as a function of an index N, where $N \in \mathbb{N}$ is an integer. For 4.2 K, Fig. 32 shows a clear linear dependence between $1/B_{max}$ and N, which indicates that the photo signal U_y oscillates with a constant frequency on a $1/B_z$-scale. Additionally, Shubnikov de Haas measurements were performed. The resistance of the sample was measured in dependence of the magnetic field B_z without illumination. At a temperature of 4.2 K, a constant current of 1 μA was used and the longitudinal resistance R_{xx} was measured via the voltage drop U_{xx}. The data are shown in the inset of Fig. 32. The longitudinal resistance shows a huge rising signal with increasing B_z and a small oscillating behavior in the high-field range above 2 T. The huge background signal is ascribed to a parallel conductance in our structure. Such a parallel transport has also been observed for similar InSb QW structures by other groups and stems from a channel parallel to the QW within the δ-doping plane of the AlInSb barrier [18,94]. Nevertheless, there are still oscillations apparent in the high-field range. The inverse magnetic field positions of the maximums in R_{xx} are also plotted in Fig. 32 and can be again

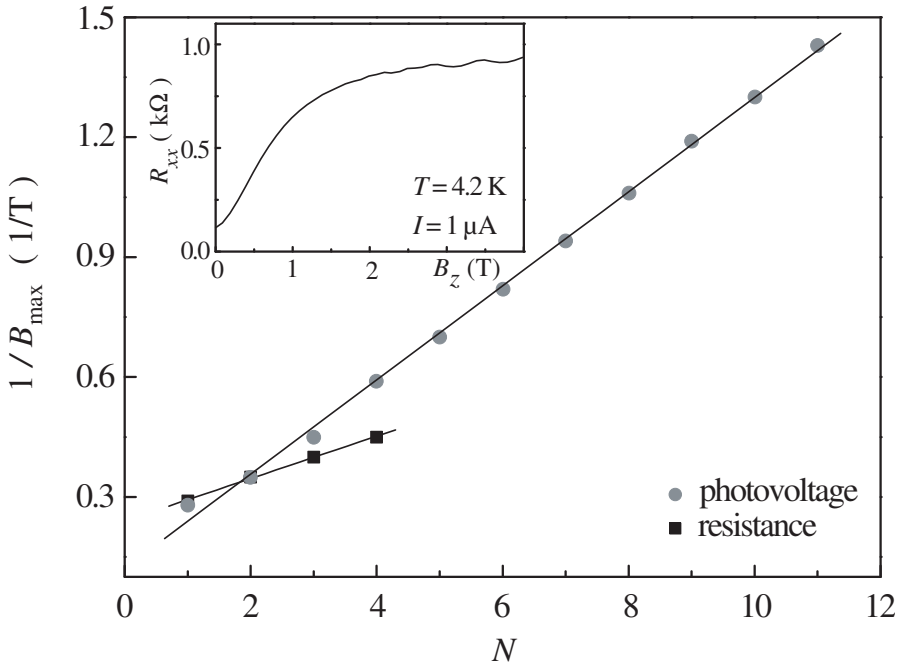

Figure 32: Maximums of the photovoltage signal (at 4.2 K in Fig. 31) and the longitudinal resistance R_{xx} on a $1/B_z$-scale as a function of an integer N. The inset shows the longitudinal resistance R_{xx} as a function of B_z measured with a constant current of 1 μA.

fitted by a linear function. A comparison of $1/B_{max}$ from the photo signal with that from the longitudinal resistance reveals that their slopes differ by a factor of about two.

The data presented above showed a resonant photo signal at a magnetic field position of $B_c \approx 2.3$ T for a fixed frequency of 2.54 THz induced by the *cw* laser system. The excitation with the pulsed laser system offers an expanded set of laser lines. An illumination with this laser system in the same geometrical setup resulted in qualitatively the same behavior as for the photovoltages shown in Fig. 28 and 29. The inset of Fig. 33 compares the resonances of the photo signals for different frequencies of 1.07, 2.03 and 3.31 THz from the pulsed laser and 2.54 THz from the *cw* laser system. The parallel signals U_x are normalized on the maximum detected signals $U_{x,max}$ and were induced by right-handed circularly polarized light. The comparison clearly demonstrates

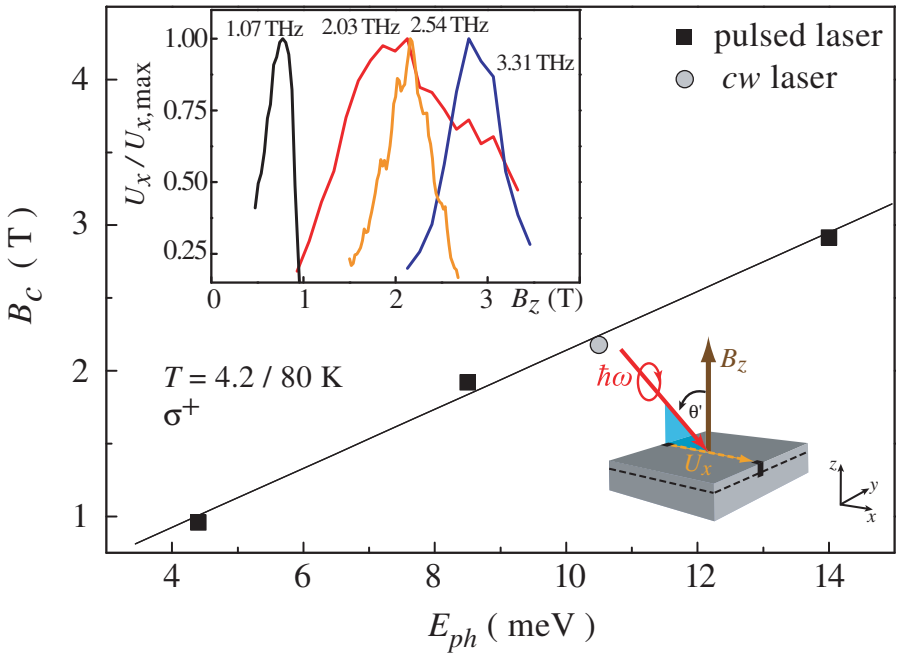

Figure 33: Resonant magnetic field positions B_c as a function of the photon energies E_{ph} of the different laser lines from the pulsed and the *cw* system. The field positions are obtained from the longitudinal photo signal shown in the left inset. The left inset illustrates the longitudinal signal U_x, normalized on the maximum signal $U_{x,max}$ for σ^+-polarization of different frequencies from the pulsed (1.07, 2.03 and 3.31 THz at 4.2 K) and the *cw* (2.54 THz at 80 K) laser system.

that similar to the transmission experiments, the maximum amplitude of the resonant signals shifts for higher frequencies to larger magnetic fields B_c. Figure 33 illustrates this behavior and shows the resonant magnetic field positions as a function of the single photon energies E_{ph}. The figure demonstrates that B_c increases linearly with increasing photon energy.

6.2 Discussion and comparison with theoretical model

The observation of the giant enhanced photo signals in the presence of a magnetic field applied normal to the 2DEG can be described in the framework of terahertz induced photocurrents under cyclotron resonance conditions. The coincidence of the transmission experiments with the photovoltage data supports this microscopic approach and demonstrates the influence of the enhanced absorption on the radiation induced currents. Furthermore, the shift of the resonances of the photo signals and the transmission with increasing photon energy to higher fields is characteristic for cyclotron resonance absorption.

For normal incidence of the laser radiation, no signal is detected. This observation is in accordance with the results for the 30 nm wide InSb QW shown in chapter 4. As this structure belongs to the C_{2v} symmetry group, photocurrents are forbidden for a normally incident beam and consequently, no resonances are present at B_c. The experimental results reveal that the resonant photovoltages are only detected for an oblique incidence of the beam. Photocurrents, which are only allowed for a tilted beam in structures of C_{2v} symmetry, may stem from the linear (LPGE) or circular (CPGE) photogalvanic effect [51, 95–97]. In contrast to the MPGEs presented in the previous chapter, these two effects do not require any external magnetic field. The CPGE has already been demonstrated in InSb QWs by using interband absorption of circularly polarized light [20]. For the LPGE excited with linearly polarized radiation, the point-group symmetry of the InSb QWs imposes some additional restrictions regarding the orientation of the radiation's electric field. These restrictions are expressed in the phenomenological equations. The LPGE's current for an asymmetrically doped InSb QW structure follows from Eq. (12) and can be written as [51]:

$$j_x^{LPGE} = \chi_{xxz} \left(E_x E_z^* + E_z E_x^* \right) \tag{54}$$

$$j_y^{LPGE} = \chi_{yyz} \left(E_y E_z^* + E_z E_y^* \right), \tag{55}$$

where χ_{xxz} and χ_{yyz} are the components of a third-rank tensor. From Eq. (54) and (55) it is obvious that both, the photocurrent in x- and in y-direction require a non-zero component ($E_z \neq 0$) of the radiation's electric field $\boldsymbol{E}$ in z-direction. This implies that the LPGE current is only present for a tilted beam

and, in addition, the incident radiation must be p-polarized. However, the experimental results demonstrate that the observed resonant signals are almost independent of the orientation of the linear polarization and, in particular, were present for s- as well as p-polarization in both x- and y-direction. This observation demonstrates that the LPGE is not the origin of the observed resonant signals.

Another effect, which may cause a photocurrent for an oblique incidence of light, is the photon drag effect. This effect is based on the momentum transfer of the photons to free carriers and is allowed for noncentrosymmetric as well as for centrosymmetric materials. The photon drag effect has been observed in many bulk materials like Ge, Si or GaP [98–101], in two-dimensional systems like GaAs and InAs QWs [97, 102, 103] and recently in graphene [104, 105]. Similar to the LPGE in InSb QWs, the photon drag effect vanishes for normal incidence of the radiation beam. The reason here is that this effect requires an in-plane component of the light's wave-vector $\boldsymbol{q}$. The drag current can be derived by solving the Boltzmann kinetic equation. This approach is analog to the microscopic model of the photon drag effect in a two-dimensional graphene sheet in [105], but now takes into account the additionally applied static magnetic field along the growth direction of the quantum well. In CGS-units, the Boltzmann kinetic equation can be written as:

$$\frac{\partial f}{\partial t} + \boldsymbol{v}\frac{\partial f}{\partial \boldsymbol{r}} + \frac{e}{\hbar}\left(\boldsymbol{E}_{\parallel}(t) + \frac{1}{c}\left[\boldsymbol{v}\times\boldsymbol{B}\right]\right)\frac{\partial f}{\partial \boldsymbol{k}} = \mathrm{St}\left[f\left(\boldsymbol{k},\boldsymbol{r},t\right)\right], \tag{56}$$

where $\boldsymbol{r}$ is the in-plane coordinate, $\boldsymbol{E}_{\parallel}(t) = \boldsymbol{E}_{\parallel,0}\, e^{i\boldsymbol{q}\boldsymbol{r}-i\omega t} + c.c.$ the in-plane component of the electric field, $\boldsymbol{B} = \boldsymbol{B}_0 + \boldsymbol{B}_1 e^{i\boldsymbol{q}\boldsymbol{r}-i\omega t} + c.c.$ the magnetic field perpendicular to the plane of the quantum well, f the electron distribution function and $\boldsymbol{v} = \frac{\boldsymbol{k}}{k}\frac{1}{\hbar}\frac{d\epsilon_k}{dk}$ the electron's velocity. The collision integral $\mathrm{St}\left[f\left(\boldsymbol{k},\boldsymbol{r},t\right)\right]$ can be described in terms of momentum relaxation times τ_m (m = 1, 2 ...) by a decomposition of the distribution function $f\left(\boldsymbol{k},\boldsymbol{r},t\right)$ into frequency, angular and spatial harmonics. The equations for the currents follow from: $\boldsymbol{j} = 2e\sum_{\boldsymbol{k}}\boldsymbol{v}_{\boldsymbol{k}}f(\boldsymbol{k})$, where the factor 2 accounts for the spin degeneracy. In the calculations of $\boldsymbol{j}$, the energy dispersion was assumed to be parabolic and τ_m and $m_c = m^*$ were kept constant.

At zero magnetic field $B_z = 0$, a non-zero current is found:

$$j_0 = -\frac{1}{2\pi}\frac{E_F}{\hbar^2}\frac{e^3E^2\tau_p^2}{m^*\omega}q_{\parallel}. \tag{57}$$

Here, ω is the radiation frequency, E_F the electron Fermi energy and $q_{\parallel} = q\cos\theta$ the in-plane component of the light wave-vector. Equation (57) represents the longitudinal photon drag effect, where the current is parallel to the in-plane component of the wave-vector $\boldsymbol{q}$ and confined in the plane of the QW. Additionally to the longitudinal photon drag effect, there is also a transverse effect. This effect is usually much weaker than the longitudinal one and is therefore neglected in our calculations [106]. For a non-zero magnetic field $B_z \neq 0$, the parallel current j_x^{gen} and the transverse component j_y^{gen} derived from the Boltzmann kinetic equation are:

$$j_x^{gen} = j_0\,\sin^2\theta\,\frac{1}{1+\omega_c^2\tau_p^2}\left(\frac{1}{1+(\omega-\omega_c)^2\,\tau_p^2}+\frac{1}{1+(\omega+\omega_c)^2\,\tau_p^2}\right), \tag{58}$$

$$j_y^{gen} = -j_0\,\sin^2\theta\,\frac{\omega_c\tau_p}{1+\omega_c^2\tau_p^2}\left(\frac{1}{1+(\omega-\omega_c)^2\,\tau_p^2}+\frac{1}{1+(\omega+\omega_c)^2\,\tau_p^2}\right), \tag{59}$$

where $\omega_c = eB_z/(c\,m^*)$ is the cyclotron frequency and $\theta = 90^\circ$ - θ'. Equations (58) and (59) describe the current of the photon drag effect in the presence of a normal magnetic field for a p-polarized incident laser beam, where the electric field components of the radiation are $E_x = E\,\sin\theta$ and $E_y = 0$. For the linear polarization oriented in the plane of the QW ($E_x = 0$, $E_y = E$, s-polarization), the factor $\sin^2\theta$ is equal to 1.

The radiation induced current j_0 generated by the photon drag effect is deflected by the normal field and enhanced due to the cyclotron resonance absorption. As a result, a current $\boldsymbol{j}^{\mathrm{gen}}$ with components in x- and y-direction arises. Due to the open-circuit configuration in the *cw* laser setup, the photocurrent $\boldsymbol{j}^{\mathrm{gen}}$ induces in the sample a static electric field $\boldsymbol{\epsilon}$, while the net electric current in the circuit is vanishingly small. The electric field $\boldsymbol{\epsilon}$ in turn induces a drift current $\boldsymbol{j}^{\mathrm{dr}}$, which compensates the photocurrent $\boldsymbol{j}^{\mathrm{gen}}$, so that the full

current at the edges and perpendicular to the border is zero. The components of the drift current are given by:

$$j_\alpha^{dr} = \sum_\beta \sigma_{\alpha\beta}\epsilon_\beta, \tag{60}$$

where $\sigma_{\alpha\beta}$ are the conductivity tensor components in the presence of a static magnetic field, which can be written as:

$$\sigma_{xx} = \sigma_{yy} = \frac{\sigma}{1+(\omega_c\tau_p)^2}, \tag{61}$$

$$\sigma_{xy} = -\sigma_{yx} = \frac{\sigma\omega_c\tau_p}{1+(\omega_c\tau_p)^2}, \tag{62}$$

$$\text{with} \quad \sigma = \frac{n_e e^2\tau_p}{m^*}. \tag{63}$$

Here, σ stands for the conductivity at zero magnetic field. The resulting current-induced electric field $\epsilon_{x,y}$, which is proportional to the detected photovoltage $U_{x,y}$, can be obtain via the Maxwell and the continuity equations. Thereby, it is assumed that the laser beam irradiates only the center of the sample and the contacts have a finite size. The parallel signal U_x and the transverse signal U_y resulting from Eqs. (57)-(63) are shown in Fig. 34 and 35 as a function of the applied magnetic field B_z for s- and p-polarized radiation.

The microscopic model based on the photon drag effect in the presence of a static magnetic field describes the essential observations of the experiments. Similar to the measured data, the calculations feature clearly resolved Lorentzian-shaped resonances with opposite parity for the parallel and transverse signal. At $B_z = 0$, a non-zero signal is only present parallel to the oblique incidence, which results from the longitudinal photon drag current j_0. The application of a magnetic field B_z causes, due to the Lorentz force, a deflection of the initially along x directed current j_0, and a non-zero component U_y rises with increasing B_z. By a further increase of the magnetic field, both signals, U_x and U_y, are strongly enhanced at $B_z = B_c$. The enhancement at this field strength stems from the increased radiation absorption at the cyclotron resonance position and is described by the last factor in Eq. (58) and (59).

The transverse and parallel signals feature different symmetries with respect to B_z. This is in agreement with the experiments: the signal U_y perpendicular

to the plane of oblique incidence represents an odd function of the magnetic field, while the parallel signal U_x is even in B_z. These two opposed parities are also present in the data shown in Fig. 28 and 29. Via the momentum relaxation time τ_p and the electron's effective mass m^*, both theoretical curves can be fitted to the measured data. These two parameters mainly influence the resonances: τ_p is inversely proportional to the width and m^* defines the position of the resonant signals.

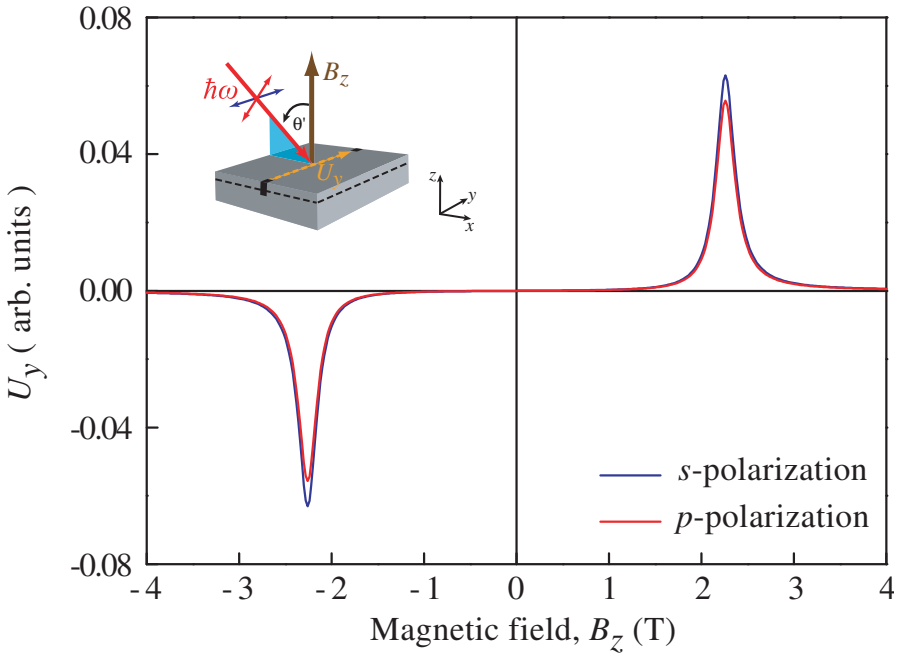

Figure 34: Calculated transverse photovoltage U_y in dependence of B_z for different orientations of the linear polarization. The left inset shows the geometrical configuration with s- (blue) and p-polarized (red) radiation.

The experimental method to identify the longitudinal photon drag effect and the distinction from other effects, in particular from the LPGE, is not so obvious. As the drag current in Eq. (57) is proportional to the in-plane component $q_\parallel$ of the light's wave-vector, the drag current changes its sign by reversing the angle of incidence $+\theta' \rightarrow -\theta'$. However, this sign-inversion is also present for the LPGE and follows from Eq. (54) and (55). An additional way to distinguish between both effects is the comparison of the polarization dependence of the

photon drag effect and the LPGE. The calculations presented above additionally reveal the dependence of the signals on the orientation of the radiation's electric field $\boldsymbol{E}$. A comparison of the photovoltages for s- and p-polarization shows that there is only a small difference in the amplitude of the resonances. In particular, the enhanced photon drag signals are present in both directions independently of the orientation of the linear polarization in or out of the QW-plane. This behavior describes very well the observations in the experiment and is contrary to the behavior of the photogalvanic effect, where the signal should completely vanish for s-polarized light. Consequently, the calculations demonstrate that the origin of the observed signals is the longitudinal photon drag effect.

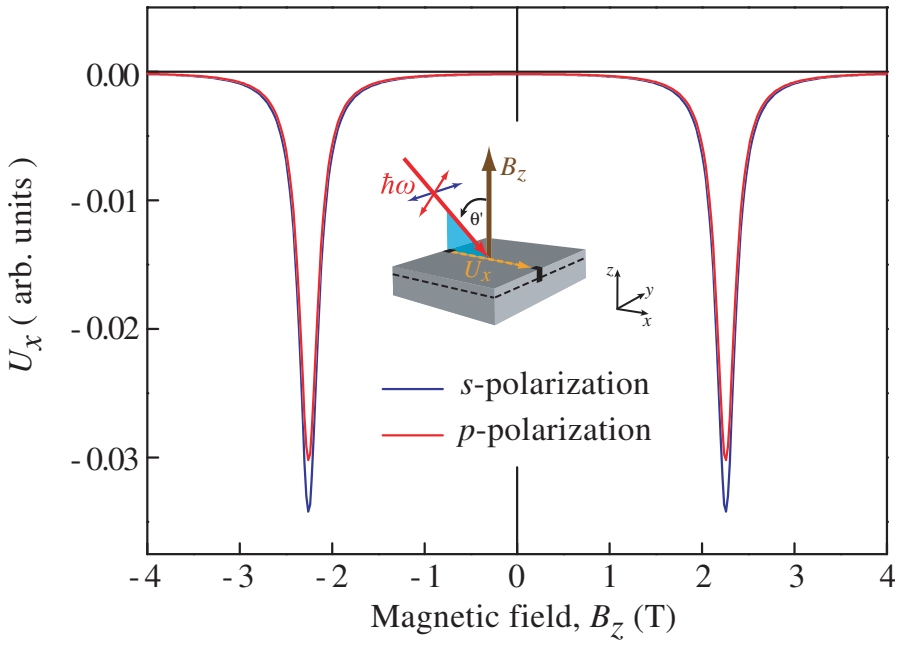

Figure 35: Calculated parallel photovoltage U_x in dependence of B_z for s- (blue) and p-polarized (red) radiation.

By fitting the calculated photovoltage dependences to the experimental data, it is possible to obtain the electron's effective mass m^* from the cyclotron resonance position B_c. Figure 33 illustrates the experimental obtained positions B_c for the different photon energies E_{ph} of the laser lines. The linear

dependence between E_{ph} and B_c is described by the condition for cyclotron resonance absorption, where $\omega_c = \omega$, and hence:

$$E_{ph} = \frac{\hbar e}{m^* c} B_c. \tag{64}$$

Following this relation, an effective mass of $m^* \approx 0.023\ m_e$ is determined. This value coincides well with values reported by other groups for similar InSb QWs (typically in the range of 0.018 - 0.026 m_e) [19,42,79,87]. The reason for the differences in m^* is its energy dependence, which results from the strong nonparabolicity in InSb. For larger energies, it follows from Eq. (5) that the effective mass increases compared to its value at the bulk InSb band edge 0.014 m_e [12]. Thus, m^* depends on parameters like the well width, carrier density and thereby on the Fermi level E_F.

The resonantly enhanced photocurrents for temperatures $T > 25$ K can be well described by the photon drag effect, deflected by the Lorentz force and strongly increased at the cyclotron resonance position. However, for lower temperatures this approach fails, because the resonances get more and more overlapped by oscillations. The comparison of the oscillations in the photo signal with that in a conventional Shubnikov de Haas experiment revealed that the oscillating behavior of the radiation induced signal is more clear resolved than in the longitudinal resistance of the transport measurements. Furthermore, the oscillations appear for the photo signal at much smaller magnetic field strengths than in R_{xx}, where oscillations are overlapped by a huge background signal. In general, the distances of the maximums in R_{xx} on a $1/B$-scale allow to determine the electron density n_e of the structure [43]. Theses distances are given by the slope in Fig. 32. It turns out that the slope of the photo signal maximums is by a factor of 2 larger than the slope of the resistance maximums. The reason for this difference is not apparent from the model developed above and hence, further studies of the oscillating photo signal are required.

6.3 Summary

In this chapter, the observation of resonantly enhanced photovoltage signals in InSb QWs under cyclotron resonance conditions was presented. It was shown that an oblique incidence of THz radiation on the sample in combination with a normally applied magnetic field yields resonant photo signals. Additionally performed transmission experiments coincide with the photovoltage resonances. The experimental studies together with the theoretical considerations demonstrated that the origin of the signals is the longitudinal photon drag effect, which is deflected by the Lorentz force and strongly enhanced due to cyclotron resonance absorption. The drag current is a consequence of the momentum transfer of the photon on the free electrons in the 2DEG. A theoretical model based on the Boltzmann kinetic equation was developed and describes very well the experimental observations. Below 25 K, the signals oscillate with the magnetic field. The origin of these oscillations can't be explained in the framework of the developed model and is a task for future investigations.

7 Conclusion

In conclusion, in this work magnetic-field-induced photocurrents were studied in InSb quantum well structures under THz laser excitation. In particular the linear and circular magnetogyrotropic photogalvanic effect (MPGE) have been observed in this material. The detailed study of the photo-induced currents together with the theoretical considerations reveals that in InSb-based low-dimensional structures, not only the spin-related origin of the MPGE is of importance, but also mechanisms based on the orbital motion of the carriers give a substantial contribution to the photocurrent. The fact that spin-based mechanisms are enhanced seems reasonable, particularly when taking into account that InSb QWs are characterized by a strong spin-orbit coupling and huge magnetic properties. Orbital effects, however, are also enhanced, as these effects increase with a lower electron effective mass, which is also characteristic for narrow-gap semiconductors. It is shown that the detailed study of the MPGE in InSb-based low-dimensional structures is an additional effective approach to distinguish between these qualitatively different mechanisms.

In the first part of this work, the linear MPGE was investigated in InSb structures in the presence of an in-plane magnetic field. The experimental results show that the photocurrents are caused by asymmetric relaxation processes in the momentum space. Furthermore, it is demonstrated that the spin-related and the orbital mechanism contribute with comparable strength to the total photocurrent. The spin-based effect reveals by means of its nonlinear magnetic field dependence a strong nonlinearity of the Zeeman spin splitting, and thereby supports recent conclusions on the high polarization-dependent spin susceptibility of a two-dimensional electron gas in InSb-based quantum wells [79, 80]. The Zeeman spin splitting is enhanced by the exchange interaction between polarized electrons, which in turn leads to an enhancement of the spin-mechanism. In addition, the circular MPGE has been observed by excitation with circularly polarized THz light. This effect manifests itself in a helicity-dependent photocurrent, which changes its sign by switching from left-handed to right-handed circular polarization. The analysis of this helicity-sensitive effect reveals that here, solely the action of the Lorentz force on the orbital motion of the electrons plays an important role. Finally, the investiga-

tion of the linear and the circular MPGE in InSb quantum wells demonstrates that in narrow gap materials, despite the strong spin-orbit coupling and consequent huge magnetic properties, also orbital roots of magnetic-field-induced photocurrents have to be taken into account.

The second part of this work was aimed to investigate THz radiation-induced photocurrents under cyclotron resonance conditions. A detailed study of the resonantly enhanced photo responses demonstrated that the observed signals are caused by the deflection of a photo-induced current and a strong enhancement due to the cyclotron resonance absorption. A microscopic model based on the photon drag effect was developed in this work, and describes all fundamental observations of the experiments. The experimental study of these resonant photo signals together with the theoretical considerations unveiled a novel opto-electronic approach to obtain information about the band structure of InSb and the dynamics of carriers. The microscopic theory, however, can not explain the oscillating behavior of the photo signal for low temperatures. A further exploration of this oscillating phenomenon may provide an additional access to the understanding and application of narrow-gap semiconductor nanostructures.

References

[1] S. A. Wolf, D. D. Awschalom, R. A. Buhrman, J. M. Daughton, S. von Molnar, M. L. Roukes, A. Y. Chtchelkanova, and D. M. Treger, *A Spin-Based Electronics Vision for the Future*, Science **294**, 1488 (2001).

[2] S. Datta and B. Das, *Electronic analog of the electro-optic modulator*, Appl. Phys. Lett. **56**, 665 (1990).

[3] Jörg Wunderlich, Byong-Guk Park, Andrew C. Irvine, Liviu P. Zârbo, Eva Rozkotová, Petr Nemec, Vít Novák, Jairo Sinova, and Tomás Jungwirth, *Spin Hall Effect Transistor*, Science **330**, 1801 (2010).

[4] I. Žutić, J. Fabian, and S. Das Sarma, *Spintronics: Fundamentals and applications*, Rev. Mod. Phys. **76**, 323 (2004).

[5] J. Fabian, A. Matos-Abiague, C. Ertler, P. Stano, and I. Žutić, *Semiconductor Spintronics*, Acta Phys. Slovaca **57**, 565 (2007).

[6] J. Nitta, T. Akazaki, and H. Takayanagi, *Gate control of spin-orbit interaction in an inverted* $In_{0.53}Ga_{0.47}As/In_{0.52}Al_{0.48}As$ *heterostructure*, Phys. Rev. Lett. **78**, 1335 (1997).

[7] A. M. Gilbertson, A. Kormnyos, P. D. Buckle, M. Fearn, T. Ashley, C. J. Lambert, S. A. Solin, and L. F. Cohen, *Room temperature ballistic transport in InSb quantum well nanodevices*, Appl. Phys. Lett. **99**, 242101 (2011).

[8] A. M. Gilbertson, M. Fearn, A. Kormnyos, D. E. Read, C. J. Lambert, M. T. Emeny, T. Ashley, and S. A. Solin, *Ballistic transport and boundary scattering in* $InSb/In_{1-x}Al_xSb$ *mesoscopic devices*, Phys. Rev. B **83**, 075304 (2011).

[9] N. Goel, J. Graham, J. C. Keay, K. Suzuki, S. Miyashita, M. B. Santos, and Y. Hirayama, *Ballistic transport in InSb mesoscopic structures*, Physica E **26**, 455 (2005).

[10] T. Ashley, L. Buckley, S. Datta, M. T. Emeny, D. G. Hayes, K. P. Hilton, R. Jefferies, T. J. Phillips, D. J. Wallis, P. J. Wilding, and R. Chau, *Hetergeneous InSb quantum well transistors on silicon for ultra-high speed, low power logic application*, Electron. Lett. **43**, 14 (2007).

[11] O. Madelung, U. Rössler, and M. Schulz, *Landolt and Bornstein - Group III Condensed matter: Group IV Elements, (IV-IV) and (III-V) Compounds. Part b - Electronic, Transport, Optical and Other Properties*. Springer, Berlin, 2006.

[12] I. Vurgaftman and J. R. Meyer, *Band parameters for III-V semiconductors and their alloys*, J. Appl. Phys. **89**, 5815 (2001).

[13] A. M. Gilbertson, W. R. Branford, M. Fearn, L. Buckle, P. D. Buckle, T. Ashley, and L. F. Cohen, *Zero-field spin splitting and spin-dependent broadening in high-mobility InSb/$In_{1-x}Al_xSb$ asymmetric quantum well heterostructures*, Phys. Rev. B **79**, 235333 (2009).

[14] A. M. Gilbertson, M. Fearn, J. H. Jefferson, B. N. Murdin, P. D. Buckle, and L. F. Cohen, *Zero-field spin splitting and spin lifetime in n-InSb/$In_{1-x}Al_xSb$ asymmetric quantum well heterostructures*, Phys. Rev. B **77**, 165335 (2008).

[15] G. A. Khodaparast, R. C. Meyer, X. H. Zhang, T. Kasturiarachchi, R. E. Doezema, S. J. Chung, N. Goel, M. B. Santos, and Y. J. Wang, *Spin effects in InSb quantum wells*, Physica E **20**, 386 (2004).

[16] T. D. Mishima, J. C. Keay, N. Goel, M. A. Ball, S. J. Chung, M. B. Johnson, and M. B. Santos, *Structural defects in InSb/$Al_xIn_{1-x}Sb$ quantum wells grown on GaAs (001) substrates*, Physica E **5121**, 770 (2004).

[17] J. M. Orr, A. M. Gilbertson, M. Fearn, O. W. Croad, C. J. Storey, L. Buckle, M. T. Emeny, P. D. Buckle, and T. Ashley, *Electronic transport in modulation-doped InSb quantum well heterostructures*, Phys. Rev. B **77**, 165334 (2008).

[18] O. J. Pooley, A. M. Gilbertson, P. D. Buckle, R. S. Hall, L. Buckle, M. T. Emeny, M. Fearn, L. F. Cohen, and T. Ashley, *Transport effects in remote-doped InSb/$Al_xIn_{1-x}Sb$ heterostructures*, New J. Phys. **12**, 053022 (2010).

[19] F. Gouider, Yu. B. Vasilyev, M. Bugr, J. Knemann, P. D. Buckle, and G. Nachtwei, *Terahertz photoresponse of AlInSb/InSb/AlInSb quantum well structures*, Phys. Rev. B **81**, 155304 (2010).

[20] M. Frazier, J. A. Waugh, J. J. Heremans, M. B. Santos, X. Liu, and G. A. Khodaparast, *Photoinduced spin-polarized current in InSb-based structures*, J. Appl. Phys. **106**, 103513 (2009).

[21] S. Stachel, P. Olbrich, C. Zoth, U. Hagner, T. Stangl, C. Karl, P. Lutz, V. V. Bel'kov, S. K. Clowes, T. Ashley, A. M. Gilbertson, and S. D. Ganichev, *Interplay of spin and orbital magnetogyrotropic photogalvanic effects in InSb/(Al,In)Sb quantum well structures*, Phys. Rev. B **85**, 045305 (2012).

[22] S. D. Ganichev, V. V. Bel'kov, S. A. Tarasenko, S. N. Danilov, S. Giglberger, Ch. Hoffmann, E. L. Ivchenko, D. Weiss, W. Wegscheider, Ch. Gerl, D. Schuh, J. Stahl, J. De Boeck, G. Borghs, and W. Prettl, *Zero-bias spin separation*, Nature Phys. **2**, 609 (2006).

[23] V. V. Bel'kov, S. D. Ganichev, E. L. Ivchenko, S. A. Tarasenko, W. Weber, S. Giglberger, M. Olteanu, H.-P. Tranitz, S. N. Danilov, Petra Schneider, W. Wegscheider, D. Weiss, and W. Prettl, *Magneto-gyrotropic photogalvanic effects in semiconductor quantum wells*, J. Phys.: Condens. Matter **17**, 3405 (2005).

[24] V. V. Bel'kov and S. D. Ganichev, *Magneto-gyrotropic effects in semiconductor quantum wells*, Semicond. Sci. Technol. **23**, 114003 (2008).

[25] S. A. Tarasenko, *Electron scattering in quantum wells subjected to an in-plane magnetic field*, Phys. Rev. B **77**, 085328 (2008).

[26] S. A. Tarasenko, *Direct current driven by ac electric field in quantum wells*, Phys. Rev. B **83**, 035313 (2011).

[27] E. D. Palik, G. S. Picus, S. Teitler, and R. F. Wallis, *Infrared Cyclotron Resonance in InSb*, Phys. Rev. **122**, 475 (1961).

[28] O. Matsuda and E. Otsuka, *Cyclotron resonance study of conduction electrons in n-type indium antimonide under a strong magnetic field*, J. Phys. Chem. Solids **40**, 809 (1979).

[29] T. Ihn, *Semiconductor Nanostructures*. Oxford University Press Inc., New York, 2010.

[30] E. O. Kane, *Band structure of indium antimonide*, J. Phys. Chem. Solids **1**, 249 (1957).

[31] R. Winkler, *Spin-Orbit Coupling Effects in Two-Dimensional Electron and Hole Systems*. Springer, Berlin, 2003.

[32] W. Zawadski, *Electron transport phenomena in small-gap semiconductors*, Adv. Phys. **91**, 435 (1973).

[33] M. I. Dyakonov, *Spin Physics in Semiconductors*. Springer, Berlin, 2009.

[34] H. J. Jiménez-González, R. L. Aggarwal, and G. Favrot, *Infrared Farady rotation of n-type InSb*, Phys. Rev. B **49**, 4571 (1994).

[35] K. L. Litvinenko, L. Nikzad, C. R. Pidgeon, J. Allam, L. F. Cohen, T. Ashley, M. Emeny, W. Zawadski, and B. N. Murdin, *Temperature dependence of the electron Landé g factor in InSb and GaAs*, Phys. Rev. B **77**, 033204 (2008).

[36] L. M. Roth, B. Lax, and S. Zwerdling, *Theory of Optical Magneto-Absorption Effects in Semiconductors*, Phys. Rev. **114**, 90 (1959).

[37] W. Zawadski, *The magnetic moment of conduction electrons in A_{III} B_V compounds*, Phys. Lett. **4**, 190 (1963).

[38] Michael P. Hasselbeck and Peter M. Enders, *Electron-electron interactions in the nonparabolic conduction band of narrow-gap semiconductors*, Phys. Rev. B **57**, 9674 (1998).

[39] D. F. Nelson, R. C. Miller, and D. A. Kleinman, *Band nonparabolicity effects in semiconductor quantum wells*, Phys. Rev. B **35**, 7770 (1987).

[40] M. J. Yang, R. J. Wagner, P. J. Lin-Chung, B. V. Shanabrook, and J. R. Waterman, *Spin-resolved cyclotron resonance in a 2D electron gas*, Surf. Sci. **305**, 271 (1994).

[41] P. Pfeffer and W. Zawadski, *Conduction electrons in GaAs: Five-level k . p theory and polaron effects*, Phys. Rev. B **41**, 1561 (1990).

[42] J. M. S. Orr, K.-C. Chuang, R. J. Nicholas, L. Buckle, M. T. Emeny, and P. D. Buckle, *Magnetoabsorption in InSb quantum-well heterostructures*, Phys. Rev. B **79**, 235302 (2009).

[43] M. Balkanski and R. F. Wallis, *Semiconductor Physics and Applications*. Oxford University Press Inc., New York, 2000.

[44] G. Dresselhaus, *Spin-orbit coupling effects in zinc blende structures*, Phys. Rev **100**, 580 (1955).

[45] Y. A. Bychkov and E. I. Rashba, *Properties of a 2D electron gas with lifted spectral degeneracy*, Pis'ma Zh. Eksp. Teor. Fiz. **39**, 66 (1984).

[46] E. L. Ivchenko, *Optical Spectroscopy of Semiconductor Nanostructures*. Alpha Science Int., Harrow, 2005.

[47] R. Eppenga and M. F. H. Schuurmans, *Effect of bulk inversion asymmetry on [001],[110] and [111] GaAs/AlAs quantum wells*, Phys. Rev. B **37**, 10923 (1988).

[48] F. G. Pikus and G. E. Pikus, *Conduction-band spin splitting and negative magnetoresistance in A_3B_5 heterostructures*, Phys. Rev. B **51**, 16928 (1995).

[49] E. A. de Andrada e Silva, G. C. La Rocca, and F. Bassani, *Spin-split subbands and magneto-oscillations in III-V asymmetric heterostructures*, Phys. Rev. B **50**, 8523 (1994).

[50] K. Seeger, *Semiconductor Physics*. Springer-Verlag, Wien, 1973.

[51] S. D. Ganichev and W. Prettl, *Intense Terahertz Excitation of Semiconductors*. Oxford Univ. Press, Oxford, 2006.

[52] B. I. Sturman and V. M. Fridkin, *The Photovoltaic and Photorefractive Effects in Non-Centrosymmetric Materials*. Gordon and Breach Science Publishers, New York, 1992.

[53] P. Olbrich, E. L. Ivchenko, R. Ravash, T. Feil, S. D. Danilov, J. Allerdings, D. Weiss, D. Schuh, W. Wegscheider, and S. D. Ganichev, *Ratchet Effects Induced by Terahertz Radiation in Heterostructures with a Lateral Periodic Potential*, Phys. Rev. Lett. **103**, 090603 (2009).

[54] E. L. Ivchenko and S. D. Ganichev, *Spin-Photogalvanics*. in *Spin Physics in Semiconductors*, p. 245, ed. M. I. Dyakonov (Springer, Berlin, 2008).

[55] S. D. Ganichev, V. V. Bel'kov, Petra Schneider, E. L. Ivchenko, S. A. Tarasenko, W. Wegscheider, D. Weiss, D. Schuh, E. V. Beregulin, and W. Prettl, *Resonant inversion of the circular photogalvanic effect in n-doped quantum wells*, Phys. Rev. B **68**, 035319 (2003).

[56] S. D. Ganichev and W. Prettl, *Spin photocurrents in quantum wells*, J. Phys.: Condens. Matter **15**, R935 (2003).

[57] E. L. Ivchenko and G. E. Pikus, *Photogalvanic effects in optically active crystals*, Ferroelectrics **43**, 131 (1981).

[58] V. I. Belinicher, *Asymmetry of the scattering of spin-polarized electrons and mechanisms of the photogalvanic effects*, Sov. Phys. Solid State **24**, 7 (1982).

[59] E. L. Ivchenko and S. A. Tarasenko, *Monopolar optical orientation of electron spins in bulk semiconductor and heterostructures*, JETP **99**, 379 (2004).

[60] S. A. Tarasenko, *Spin orientation of a two-dimensional electron gas by a high frequency electric field*, Phys. Rev. B **73**, 115317 (2006).

[61] E. L. Ivchenko and S. A. Tarasenko, *Pure spin photocurrents*, Semicond. Sci. Technol. **23**, 114007 (2008).

[62] S. A. Tarasenko and E. L. Ivchenko, *Pure spin photocurrents in low-dimensional structures*, Pis'ma Zh. Eksp. Teor. Fiz. **81**, 292 (2005). [JETP Lett. **81**, 231 (2005)].

[63] S. D. Ganichev, E. L. Ivchenko, V. V. Bel'kov, S. A. Tarasenko, M. Sollinger, D. Weiss, W. Wegscheider, and W. Prettl, *Spin-galvanic effect*, Nature (London) **417**, 153 (2002).

[64] S. D. Ganichev, *The infrared spin-galvanic effect in semiconductor quantum wells*, Physica E **20**, 419 (2004).

[65] N. S. Averkiev, L. E. Golub, and M. Willander, *Spin relaxation anisotropy in two-dimensional semiconductor systems*, J. Phys.: Condens. Matter **14**, R271 (2002).

[66] C. F. McConville, C. R. Whitehouse, G. M. Williams, A. G. Cullis, T. Ashley, M. S. Skolnick, G. T. Brown, and S. J. Courtney, *Interfacial studies and electrical characterisation of heteroepitaxial InSb on GaAs (001) grown by MBE*, J. Crystal Growth **95**, 228 (1989).

[67] Tetsuya D. Mishima and Michael B. Santos, *Regression analysis for transport electron scattering caused by structural defects in InSb quantum wells: Application of Matthiessen's Formula*, Jpn J. Appl. Phys. **51**, 06FE07–1 (2012).

[68] M. A. Leontiadou, K. L litvinenko, A. M. Gilbertson, C. R. Pidgeon, W. R. Branford, L. F. Cohen, M. Fearn, T. Ashley, M. T. Emeny, B. N. Murdin, and S. K. Clowes, *Experimental determination of the Rashba*

coefficient in InSb/InAlSb quantum wells at zero magnetic field and elevated temperatures, J. Phys.: Condens. Matter **23**, 035801 (2011).

[69] J. M. Orr, P. D. Buckle, M. Fearn, C. J. Storey, L. Buckle, and T. Ashley, *A surface-gated InSb quantum well single electron transistor*, New J. Phys. **9**, 261 (2007).

[70] F. K. Kneubühl and M. W. Sigrist, *Laser*. Teubner, Wiesbaden, 2005.

[71] O. Svelto, *Principles of lasers*. Plenum Press, New York, 1998.

[72] G. W. Chantry, *Long-wave optics Vol. 2: Applications*. Academic Press, London, 1984.

[73] P. K. Cheo, *Handbook of molecular lasers*. Marcel Dekker Inc, New York, 1987.

[74] M. Born and E. Wolf, *Principles of optics*. Pergamon Press, Oxford, 1964.

[75] Sh. M. Kogan, *A photoconductivity theory based on variations of carrier mobility*, Sov. Phys. Solid State **4**, 1386 (1963).

[76] E. H. Putley, *Far Infra-Red Photoconductivity*, Phys. Stat. Sol. **6**, 571 (1964).

[77] P. M. Valov and B. S. Ryvkin, *Intraband Photoconductivity in n-type Ge caused by optical heating of electrons*, Sov. Phys. Semicond. **5**, 797 (1971).

[78] G. V. Budkin and S. A. Tarasenko, *Heating and Cooling of a Two-Dimensional Electron Gas by Terahertz Radiation*, J. Exp. Theor. Phys. **112**, 656 (2011).

[79] B. Nedniyom, R. J. Nicholas, M. T. Emeny, L. Buckle, A. M. Gilbertson, P. D. Buckle, and T. Ashley, *Giant enhanced g-factors in InSb two-dimensional gas*, Phys. Rev. B **80**, 125328 (2009).

[80] K. F. Yang, H W Liu, T. D. Mishima, M. B. Santos, K. Nagase, and Y. Hirayama, *Nonlinear magnetic field dependence of spin polarization in high-density two-dimensional electron systems*, New J. Phys. **13**, 083010 (2011).

[81] Ying Zhang and S. Das Sarma, *Nonlinear 2D spin susceptibility in a finite magnetic field: spin-polarization dependence*, Phys. Rev. Lett. **96**, 196602 (2006).

[82] R. J. Nicholas, R. J. Haug, and K. v. Klitzing, *Exchange enhancement of the spin splitting in a GaAs-Ga_xAl_{1-x} heterojunction*, Phys. Rev. B **37**, 1294 (1988).

[83] E. Tutuc, S. Meinte, and M. Shayegan, *Spin polarization and g-factor of a dilute GaAs two-dimensional electron system*, Phys. Rev. Lett. **88**, 036805 (2002).

[84] J. Zhu, H. L. Stormer, L. N. Pfeiffer, K. W. Baldwin, and K. W. West, *Spin susceptibility of an ultra-low-density two-dimensional electron system*, Phys. Rev. Lett. **90**, 056805 (2003).

[85] V. Ya. Aleshkin, V. I. Gavrilenko, A. V. Ikonnikov, S. S. Krishtopenko, Yu. G. Sadofyev, and K. E. Spirin, *Exchange enhancement of the g-factor in InAs/AlSb heterostructures*, Semiconductors **42**, 828 (2008).

[86] Yu. G. Sadofyev, A. Ramamoorthy, B. Naser, J. P. Bird, S. R. Johnson, and Y.-H. Zhang, *Large g-factor enhancement in high-mobility InAs/AlSb quantum wells*, Appl. Phys. Lett. **81**, 1833 (2002).

[87] G. A. Khodaparast, D. C. Larrabee, and J. Kono, *Relaxation of quasi-two-dimensional electrons in a quantizing magnetic field probed by time-resolved cyclotron resonance*, Phys. Rev. B **67**, 035307 (2003).

[88] S. A. Tarasenko, *Direct current driven by ac electric field in quantum wells*, Phys. Rev. B **83**, 035313 (2011).

[89] V. I. Fal'ko, *Rectifying properties of 2D inversion layers in a parallel magnetic field*, Sov. Phys. Solid State **31**, 561 (1989).

[90] V. Lechner, L. E. Golub, F. Lomakina, V. V. Bel'kov, P. Olbrich, S. Stachel, I. Caspers, M. Griesbeck, M. Kugler, M. J. Hirmer, T. Korn, C. Schüller, D. Schuh, W. Wegscheider, and S. D. Ganichev, *Spin and orbital mechanisms of the magneto-gyrotropic photogalvanic effects in GaAs/AlGaAs quantum well structures*, Phys. Rev. B **83**, 155313 (2011).

[91] W. Hanle, *Über magnetische Beeinflussung der Polarisation der Resonanzfluoreszenz*, Zeitschrift für Physik **30**, 93 (1924).

[92] K. L litvinenko, B. N. Murdin, J. Allam, C. R. Pidgeon, M. Bird, K. Morris, W. Branford, S. K. Clowes, L. F. Cohen, T. Ashley, and L. Buckle, *Spin relaxation in n-InSb/AlInSb quantum wells*, New J. Phys. **8**, 49 (2006).

[93] Germain Chartier, *Introduction to Optics*. Springer, New York, 2005.

[94] A. M. Gilbertson, P. D. Buckle, M. T. Emeny, T. Ashley, and L. F. Cohen, *Supression of the buffer layer conductance in InSb/$Al_xIn_{1-x}Sb$ heterostructures using a wide-band-gap barrier layer*, Phys. Rev. B **84**, 075474 (2011).

[95] E. L. Ivchenko and G. E. Pikus, *Superlattices and Other Heterostructures. Symmetry and Optical Phenomena*. Springer, Berlin, 1997.

[96] S. D. Ganichev, E. L. Ivchenko, S. N. Danilov, J. Eroms, W. Wegscheider, D. Weiss, and W. Prettl, *Conversion of Spin into Directed Electric Current in Quantum Wells*, Phys. Rev. Lett. **86**, 4358 (2001).

[97] S. D. Ganichev, E. L. Ivchenko, and W. Prettl, *Photogalvanic effects in quantum wells*, Physica E **14**, 166 (2002).

[98] A. F. Gibson, M. F. Kimmit, and A. C. Walker, *Photon drag in germanium*, Appl. Phys. Lett. **17**, 75 (1970).

[99] E. V. Beregulin, P. M. Voronov, S. V. Ivanov, P. S. Kop'ev, and I. D. Yaroshetskii, *Experimental observation of drag of 2D electrons by far-IR light*, Sov. Phys. JETP Lett. **59**, 85 (1994).

[100] A. M. Danishevskii, A. A. Kastal'skii, S. M. Ryvkin, and I. D. Yaroshetskii, *Dragging of free carriers by photons in direct interband transitions in semiconductors*, Zh. Èksp. Teor. Fiz. **58**, 544 (1970). [Sov. Phys. JETP **31**, 292 (1970)].

[101] V. M. Tuchkevich and V. Ya. Frenkel, eds., *Semiconductor Physics - The Photon Drag of Electrons in Semiconductors*. Consultants Bureau, New York, 1986.

[102] V. A. Shalygin, H. Diehl, Ch. Hoffmann, S. N. Danilov, T. Herrle, S. A. Tarasenko, D. Schuh, Ch. Gerl, W. Wegscheider, W. Prettl, and S. D. Ganichev, *Spin photocurrents and circular photon drag effect in (110)-grown structures*, JETP Lett. **84**, 570 (2006).

[103] A. P. Dmitriev, S. A. Emelyanov, S. V. Ivanov, P. S. Kop'ev, Ya. V. Terent'ev, and I. D. Yaroshetsky, *Photon-drag current in 2DEG in the vicinity of cyclotron resonance and its first subharmonic*, Surf. Sci. **263**, 659 (1992).

[104] Chongyun Jiang, V. A. Shalygin, V. Yu. Panevin, S. N. Danilov, M. M. Glazov, R. Yakimova, S. Lara-Avila, S. Kubatkin, and S. D. Ganichev, *Helicity-dependent photocurrents in graphene layers excited by midinfrared radiation of a CO_2 laser*, Phys. Rev. B **84**, 125429 (2011).

[105] J. Karch, P. Olbrich, M. Schmalzbauer, C. Brinsteiner, U. Wurstbauer, M. M. Glazov, S. A. Tarasenko, E. L. Ivchenko, D. Weiss, J. Eroms, and S. D. Ganichev, *Photon helicity driven electric currents in graphene*, arXiv: 1002.1047v1 (2010).

[106] S. D. Ganichev and W. Prettl, *Spin photocurrents in quantum wells*, J. Phys.: Condens. Matter **15**, R935 (2003).

Danksagung

Ich möchte mich an dieser Stelle ganz herzlich bei allen bedanken, die mich während der Promotion begleitet und zu dieser Dissertation maßgeblich mit beigetragen haben.

Zuerst möchte ich mich bei Sergey Ganichev bedanken, der mir die Möglichkeit gegeben hat, diese Doktorarbeit in seiner Arbeitsgruppe anzufertigen. Bei der Arbeit an diesem interessanten und aufschlussreichen Thema stand er mir bei Fragen zu Experimenten und Theorie stets zur Seite.

Auch bei meinen Eltern möchte ich mich sehr bedanken, dass sie mir mein Studium in Physik ermöglichten. Vielen Dank auch an meine zwei Brüder, die mich während Studium und Promotion immer begleitet haben.

Des Weiteren möchte ich Sergey Danilov und Vasily Bel'kov danken, die mir bezüglich des experimentellen Aufbaus und der durchgeführten Experimente immer gute und nützliche Ratschläge erteilen konnten. Vielen Dank auch an Sergey Tarasenko und Grigory Budkin für die theoretische Unterstützung und die anregenden Diskussionen.

Zudem möchte ich der AG Ganichev und all ihren Ehemaligen meinen besonderen Dank für die gute Zusammenarbeit und das gute Arbeitsklima aussprechen. Vor allem meine Diplomanden und Masteranden Cynthia Karl, Thomas Stangl und Ursula Hagner haben viel zum Gelingen dieser Arbeit beigetragen. Für das Korrekturlesen bedanke ich mich bei Peter Olbrich, Christoph Drexler und Christina Zoth. Dazu auch vielen Dank an Vera Lechner, Johannes Karch, Markus Fehrenbacher, Josef Kamann, Thomas Schönberger, Bernhard Wittmann, Christina Reitmaier, Michael Schmalzbauer, Chonyung Jiang, Ines Caspers, Marion Hirmer, Peter Lutz, Christoph Schönhuber, Wolfgang Eder, Christoph Brinsteiner, Faina Lomakina, Helgi Diehl, Patricia Vierling, Helene Plank, Florian Müller, Florian Rückerl, Tobias Herrmann und Kathrin Dantscher. Für die technische und formale Unterstützung bedanke ich mich bei Anton Humbs und Hannelore Lanz.

Zuletzt möchte ich mich ganz besonders bei meiner Freundin Verena Winkler bedanken, die mich in all den Jahren stets unterstützt hat und immer für mich da war.